2020

Fabrication of advanced electrochemical capacitors with higher energy density

Xiaohui Tang
Iowa State University

Fabrication of advanced electrochemical capacitors with higher energy density

by

Xiaohui Tang

A dissertation submitted to the graduate faculty

in partial fulfillment of the requirements for the degree of

DOCTOR OF PHILOSOPHY

Major: Mechanical Engineering

Program of Study Committee:
Shan Hu, Major Professor
Jonathan Claussen
Xinwei Wang
Robbyn K. Anand
Yue Wu

The student author, whose presentation of the scholarship herein was approved by the program of study committee, is solely responsible for the content of this dissertation. The Graduate College will ensure this dissertation is globally accessible and will not permit alterations after a degree is conferred.

Iowa State University

Ames, Iowa

2020

DEDICATION

In dedication to my father, mother, mentors, colleagues and all other people that support me all the way.

TABLE OF CONTENTS

Page

ACKNOWLEDGMENTS

I would like to thank my committee chair, Dr. Shan Hu and my committee members, Dr. Jonathan Claussen, Dr. Xinwei Wang, Dr. Robbyn K. Anand, and Dr. Yue Wu, for their guidance and support throughout the course of this research.

In addition, I would also like to thank my friends, colleagues, the department faculty and staff for making my time at Iowa State University a wonderful experience. I want to also offer my appreciation to those who were willing to participate in my surveys and observations, without whom, this thesis would not have been possible.

ABSTRACT

Much effort has been put into improving the performance of the electrochemical capacitors (which can also be named as supercapacitors) due to their higher power density than that of batteries and higher energy density than that of conventional capacitors, respectively. Besides, it has been discovered that, in supercapacitors, there are about three types of electrode materials (including EDLC electrode, battery-type electrode and pseudocapacitive electrode) according to their different energy storage mechanisms and, with the combinations of different electrode materials, about three types of supercapacitors can be categorized, such as electric double layer capacitor (made of two EDLC electrode), asymmetric supercapacitor (fabricated by one pseudocapacitive electrode and one EDLC electrode or another different pseudocapacitive electrode) and hybrid supercapacitor (built by one battery-type electrode and one EDLC electrode or one pseudocapacitive electrode). In this dissertation, the energy storage mechanisms of these electrode materials are reviewed and the corresponding kinetic analysis based on cyclic voltammetry curves are discussed. Moreover, for the purpose of achieving better overall performance than that of batteries so that the supercapacitors cannot only be used in long term energy storage but also in rapid charge/discharge power supply, it is still necessary to develop supercapacitors possessing higher energy density without sacrificing their power density. Therefore, the four projects presented in this dissertation are the investigations of our group towards this ultimate goal.

CHAPTER 1. GENERAL INTRODUCTION

1. 1 Background

It is noted that the recent conflicts of our world are mainly coming from the struggle of energy resources, especially fossil fuels (such as oil, natural gas and coal) which are limited in supply, unevenly distributed on earth and cannot be regenerated within millions of years. In order to mitigate the possible occurrence of energy crisis when the depletion of fossil fuels happens, renewable energies (including water energy, solar energy, wind energy and geothermal energy etc.) have drawn great attentions of researchers from all over the world.[1, 2, 3] However, the energies produced from these renewable resources are usually intermittent which cannot continuously dispatch electricity to the power grid. Thus, it is of great importance to develop reliable energy storage devices that can firstly store electrical energy (produced from renewable resources) and, then, release it at the request of the power grid.

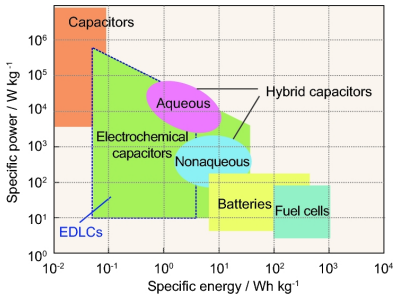

Figure 1.1. Ragone plot with energy density and power density for different energy storage devices. Reproduced with permission from Ref.[4]

Generally, there are mainly four types of energy storage devices (i.e. fuel cells, batteries, conventional capacitors and electrochemical capacitors which can also be named as supercapacitors) that have been widely recognized.[4] The performance of these devices can be described in Ragone plot whose X-axis and Y-axis represent energy density and power density,

respectively, as shown in figure 1.1. Briefly, energy density describes the amount of energy that can be stored in devices and power density indicates the charging/discharging rate of the devices.

1. 2 Brief introduction of fuel cells and batteries

1.2.1 Fuel cells

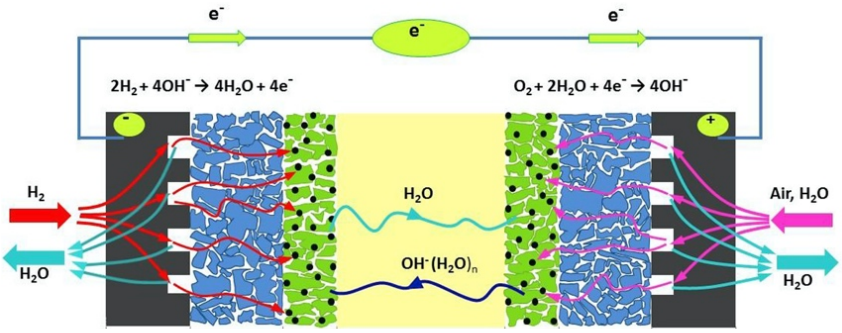

Figure 1.2. Schematic illustration of fuel cell. Reproduced with permission from Ref.[5]

According to the report, the first fuel cell was invented by Sir William Grove in 1839 and, then, put into practical usage by Francis Thomas Bacon in 1932 after many years of improvement.[6, 7] It needs to mention that the excess electrical energy that generated from power plant can be converted into chemical energy stored in hydrogen (H_2) through water decomposition ($2H_2O \rightarrow 2H_2 + O_2$). Reversely, fuel cells can convert chemical energy in H_2 with the mixing of oxygen (O_2) to electrical energy. As shown in figure 1.2, the anode reaction is $2H_2 + 4OH^- \rightarrow 4H_2O + 4e^-$ and the cathode reaction is $O_2 + 2H_2O + 4e^- \rightarrow 4OH^-$. The overall reaction in fuel cells is $2H_2 + O_2 \rightarrow 2H_2O + electrical\ energy + heat$.[5, 8] Contributed by this reaction, fuel cells can provide the highest energy density comparing with the other three energy storage devices suggesting their high energy storage capability, but the power density of fuel cells is very low indicating their slow energy converting rate. Moreover, there are still a lot of concerns regarding hydrogen storage systems, such as safety, cost and stability.[9, 10]

1.2.2 Batteries

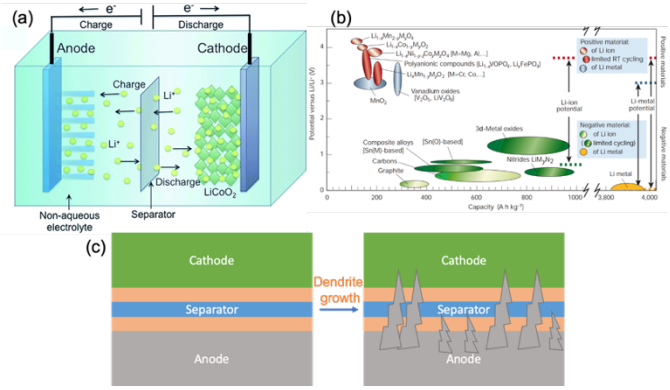

Figure 1.3. (a) Schematic illustration of Li-ion battery. (b) Some examples of the electrode materials of rechargeable Li-based cells. Reproduced with permission from Ref.[11, 12]

Besides fuel cells, batteries can also supply comparable high energy densities and its different mechanism from fuel cells can avoid the problems of hydrogen storage. Currently, batteries, especially Li-ion batteries , have been widely used not only to power the portable devices (e.g. electric vehicles, mobile phones and laptops, etc.) but also for large-scale grid energy storage due to their great energy-to-weight ratio, high open circuit voltage and low self-discharge rate.[13] Typically, a Li-ion battery is constructed by the organic based electrolyte, anode, cathode and a separator as shown in figure 1.3a. The electrical energy produced from power plant can be stored in batteries by the electrochemical reactions happening on both two electrodes (In Li-ion batteries, the reactions are the intercalation/deintercalation processes of Li ions on both cathode and anode materials.) and the electrolytes are the medium that can pass the species with charge (such as Li ions) in order to achieve charge balance of the system. Besides, the electrolytes used in Li-ion batteries are normally made of organic solvents containing Li ions, such as $LiPF_6$ in Ethylene carbonate (EC)-ethyl methyl carbonate (EMC) organic solvent.[14] However, the organic electrolytes are either toxic or flammable; aqueous electrolytes are limited by the narrow electrochemical stability window of water (which is about 1.23 V) which cannot

support most of the electrochemical couples used in Li-ion batteries; and the use of liquid electrolytes in Li-ion batteries has a risk of leakage which creates a hidden danger in our life.[15] In order to solve these problems, many works have been done, for example, Wang et al. proposed an aqueous/non-aqueous hybrid electrolyte with tailored electrode/electrolyte interphase producing an electrochemical stability window of 4.1 V.[16] Suo et al. for the first time developed a "water in salt" electrolyte which forms a dense protecting interphase on the anode surface and helps expand the electrochemical stability window of 3V.[17] Liu et al. reported a quasi-solid-state PVA-$LiNO_3$ hydrogel polymer electrolyte for Li-ion batteries.[18] For the electrodes, as shown in figure 1.3b, the output voltage of prepared Li-ion battery is decided by the potential difference of releasing and accepting processes of Li^+ ions between the cathode and anode.[12] Generally, during the charge process of Li-ion battery, the Li^+ ions released from the cathode material (e.g. $LiCoO_2$, $LiMn_2O_4$ and $LiNi_xCo_yMn_zO_2$, etc.) will transfer through the electrolyte and separator to the anode material; and the discharge process has an reversed process.[19] Theoretically, the most ideal anode material for rechargeable batteries is Li metal due to its superior capacity and lowest potential comparing with other materials (figure 1.3b). However, the growth of Li dendrite (figure 1.3c) during charge and discharge process can penetrate the separator and reach cathode resulting in the circuit short with a catastrophic cell failure.[20] The researchers also developed many other anode materials such as carbon-based material (e.g. graphite and graphene), TiO_2, alloy-based materials (Si, Sn, P) and transition metal oxides (e.g. Mn_3O_4) in order to mitigate Li dendrite growth, but the capacities of these materials are much lower than that of Li metal.[21] Thus, there are still a lot of research works that needs to be done in order to develop better anode materials for Li-ion batteries.

1. 3 Electrochemical capacitors (supercapacitors)

In terms of overall performance (figure 1), batteries exhibit very high energy densities but their power densities are so small that cannot meet the requirement of fast charging for modern devices. Besides, although the dielectric capacitors (which store charges dielectrically) have very high power densities, their energy densities are too low to store much energy. Therefore, it is necessary to investigate one type of devices which can provide relatively high energy density and high power density at the same time. To do so, electrochemical capacitors (or supercapacitors) have been investigated and their potentials in bridging the gap between batteries and dielectric capacitors have attracted a lot of research interests.

1.3.1 Electrodes of supercapacitors with different energy storage mechanisms

Based on the energy storage mechanisms, three types of electrodes can be categorized in electrochemical capacitors, including electric double layer capacitive (EDLC) electrodes, battery-type electrodes and pseudocapacitive electrodes.

I. EDLC electrode

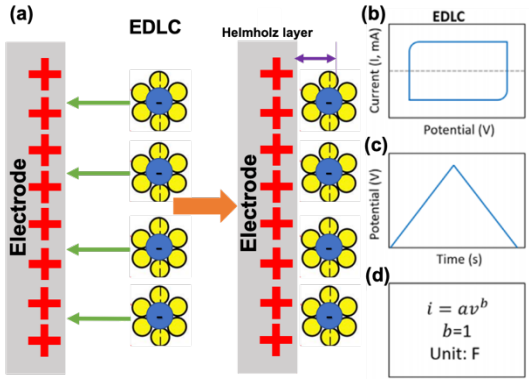

Figure 1.4. (a) Schematic of EDLC electrode. Typical (b) CV curves, (c) GCD profiles and (d) kinetic analysis of EDLC electrode. Reproduced with permission and modified from Ref.[22, 23]

In EDLC electrodes (typically made of conductive materials with high surface area such as activated carbon, carbon nanotubes and graphene, etc.), energy is stored/released through

adsorption/desorption of ions on the surface of electrode material (which forms a layer called Helmholtz layer as shown in figure 1.4a).[24, 25] The capacitance of the EDLC electrode (C_{dl}) can be estimated by equation 1: [26]

$$C_{dl} = \frac{Q}{V} = \frac{\varepsilon_r \varepsilon_0}{d} A \qquad (1)$$

Where Q is the total charge transferred at the potential of V, ε_r is the permittivity of the electrolyte, ε_0 is the permittivity of vacuum, d is the charge separation distance and A is the electrode surface area (which is accessible to the ions).[27] In the conventional capacitors, the charge separation distance is the distance between the two electrode plates, while, in EDLC electrode, the charge separation distance is close to the average thickness of Helmholtz layer; and the so called electric double layer capacitor made by two EDLC electrodes can be treated as the two EDLC electrodes linked in series. According to this equation, comparing with conventional capacitor, the EDLC electrode (which can be treated as a small capacitor) has the smaller d value and much higher A value. As a result, the EDLC electrode is able to provide higher capacitance value than that of the conventional capacitor. Besides, as shown in figure 1.4b, the cyclic voltammetry (CV) curves of EDLC electrodes give a rectangular shape which can be explained by equation 2. [28]

$$I = \frac{dQ}{dt} = C_{dl} \frac{dV}{dt} = C_{dl} \nu \quad (2)$$

Where I is the response current, t is time and ν is the scan rate in CV. Since the ideal C_{dl} is constant, the current only responds linearly with the scan rate which can be reflected by the rectangular shapes at different scan rates. Moreover, in the galvanostatic charge and discharge (GCD) tests (figure 1.4c), the potential changes linearly with respect to the time which is because that the whole process merely involves in the non-faradaic charge rearrangement.[26] Figure 1.4d,

which is about the kinetics analysis of the EDLC electrode based on the CV curves, will be discussed along with the kinetics analysis of the other two types of electrodes in the later section.

II. Battery-type electrodes

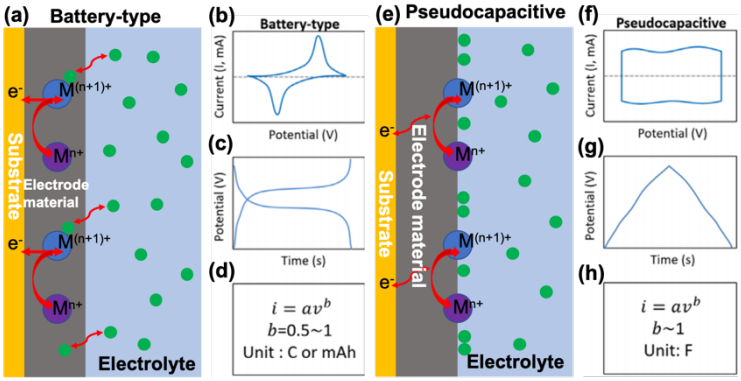

Figure 1.5. (a) Schematic of battery-type electrode. Typical (b) CV curves, (c) GCD profiles and (d) kinetic analysis of battery-type electrode. (e) Schematic of pseudocapacitive electrode. Typical (f) CV curves, (g) GCD profiles and (h) kinetic analysis of pseudocapacitive electrode. Reproduced with permission and modified from Ref.[23]

In traditional battery-type electrode, the energy is stored/released via diffusion-limited bulk faradaic redox reactions of the electrode materials (as shown in figure 1.5a) which are normally metal oxides/hydroxides or their related derivatives, such as $Ni(OH)_2$, Ni_3S_4 and graphene-$NiMoO_4$ composite,etc.[29, 30 ,31] Due to the sluggish faradaic redox reactions of the electrode material, a pair of well separated redox peaks can be clearly observed (figure 1.5b). The peak with the positive current is the oxidation peak while the other one is the reduction peak. In the GCD profiles, the potential will be pinned at a certain position during the charge process reflected by the plateau found in figure 1.5c which can also be observed during the discharge process. According to the reaction processes happening between the host battery-type electrode material and the guest ions (from the electrolyte), two different reaction mechanisms can be found:[32, 33]

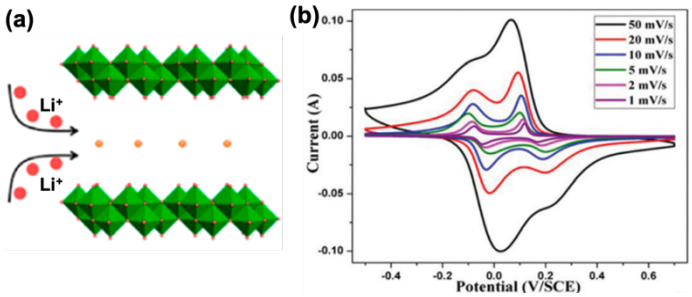

Figure 1.6. (a) Schematic illustration of the intercalation of Li^+ into V_2O_5 with layered structure. (b) CV curves of porous V_2O_5 hierarchical spheres in the $LiNO_3$ electrolyte. Reproduced with permission and modified from Ref.[34, 35]

(1) Intercalation: The intercalation/deintercalation process of the cations into/out of the tunnel or the layer structure of the host electrode material (which are normally made of Mo, Ti, and V based oxides/compounds) provides the basics of energy storage and a small structure variation can be observed during these processes. For example, as shown in figure 1.6a, during the discharge process of the electrode, Li^+ ions can be intercalated into the interlayer space of V_2O_5 (which is usually used as negative electrode in supercapacitor) and the deintercalation process can happen during the charge process.[34] The whole reaction can be described by the CV curves in figure 1.6b as well as the equation (3): [35, 36]

$$V_2O_5 + xLi^+ + xe^- \underset{Charge}{\overset{Discharge}{\rightleftharpoons}} Li_xV_2O_5 \ (0 \le x \le 1) \quad (3)$$

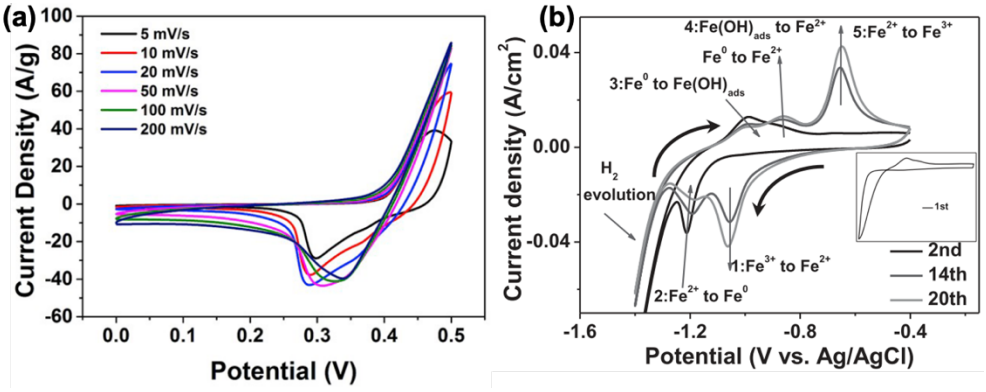

Figure 1.7. CV curves of (a) $Ni(OH)_2/NiMoO_4$ nanoplates electrode and (b) Fe_3O_4 nanorod array electrode. Reproduced with permission from Ref.[37, 38]

(2) Conversion: The energy is stored through converting the pristine material (which reacts with ions from the electrolyte) to the new phases, while the energy is released when the reversed reactions occur. Battery-type electrodes with conversion mechanism are usually made of Ni, Co oxides/hydroxides and iron oxides, etc. For example, $NiMoO_4$ as the positive electrode in hybrid supercapacitor with alkaline electrolyte has the reaction mechanisms as shown in equation (4-6) and the CV curves are shown in figure 1.7a:[37]

$$NiMoO_4 \leftrightarrow Ni^{2+} + MoO_4^{2-} \quad (4)$$

$$Ni^{2+} + 2OH^- \leftrightarrow Ni(OH)_2 \quad (5)$$

$$Ni(OH)_2 + OH^- \leftrightarrow NiOOH + H_2O + e^- \quad (6)$$

Li et al. has reported the phase change (along with the change of valence states) of Fe_3O_4 nanorod array electrode (as the negative electrode) during the CV tests (figure 1.7b).[38] The whole reaction can be summarized as follows:

$$Fe^{3+} \overset{OH^-}{\Longleftrightarrow} Fe^{2+} \overset{OH^-}{\Longleftrightarrow} Fe^0 \quad (7)$$

It is necessary to mention that the reason for calling the redox reaction of battery-type electrode material is a diffusion-limited process (or its redox reaction is sluggish) is that the redox reaction of battery-type electrode material usually involves in the ions from the electrolyte and it always takes time for the ions (or electrolyte) to diffuse (or penetrate) into the material in order to intercalate themselves into suitable positions or contact the limited electroactive sites of material to have the phase change reactions. In other words, the happening of the redox reaction is controlled by the diffusion rate of the ions travelling to the suitable intercalation positions or the limited electroactive sites of the electrode material.[39] Thus the reaction process of battery-type electrode is clearly slower than the process that only occurs on the surface of the electrode material, including EDLC electrode and pseudocapacitive electrode (which will be discussed in

the next paragraph). Figure 1.5d, which is about the kinetics analysis of the battery-type electrode based on the CV curves, will be discussed along with the kinetics analysis of the other two types of electrodes in the later section.

III. Pseudocapacitive electrodes

The pseudocapacitive electrode is at the middle stage of EDLC and battery-type electrodes and the energy is stored/released through fast and reversible faradaic redox reactions at the surface or near surface of the electrode materials (figure 1.5e).[26] As displayed in figure 1.5f and g, the typical CV curve of pseudocapacitive electrode has a near-rectangular shape with some small humbles (which represent the fast redox reactions) and its GCD profiles are almost linear.[23] Figure 1.5h, which is about the kinetics analysis of the pseudocapacitive electrode based on the CV curves, will be discussed along with the kinetics analysis of the other two types of electrodes in the later section.

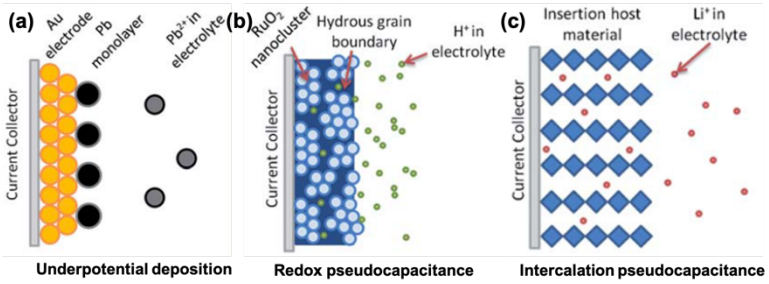

Figure 1.8. Schematic of (a) underpotential deposition, (b) redox pseudocapacitance and (c) Intercalation pseudocapacitance. Reproduced with permission and modified from Ref.[40]

To date, three types of pseudocapacitive mechanisms have been discovered:[23, 26, 28, 33]

(1) Underpotential deposition: Based on figure 1.8a, a monolayer of metal ions (such as Pb^{2+}) will be deposited on the surface of another metal (such as Au) when the potential reaches less negative that its reduction potential value (figure 1.8b). This process can also be indicated in this equation shown as follows:[41]

$$Au + xPb^{2+} + 2xe^{-} \leftrightarrow Au \cdot xPb \qquad (8)$$

(2) Redox pseudocapacitance: Under this mechanism, cations are adsorbed on the surface or near-surface of electrode material (such as MnO_2 and RuO_2) with a faradaic charge transfer during the charge process while a reversed process can be observed during the discharge process (figure 1.8b). For example, the pseudocapacitive behavior of RuO_2 electrode is believed to be originated from the surface adsorption/desorption of protons (H^+) along with the change of valence state of Ru element as shown in the following equation:[42]

$$RuO_2 + \delta H^+ + \delta e^- \leftrightarrow RuO_{2-\delta}(OH)_\delta \qquad (9)$$

Besides, MnO_2 has a surface adsorption along with the change of valence states mechanism as shown in the following equation:[43, 44, 45]

$$(MnO_2)_{surface} + C^+ + e^- \leftrightarrow (MnO_2^- C^+)_{surface} \quad (10)$$

Where C^+ represents Li^+, K^+ or Na^+. However, it has been reported that MnO_2 as pseudocapacitive material also involves in intercalation/deintercalation mechanism which will be introduced in the next paragraph.

(3) Intercalation pseudocapacitance: Although the related electrode materials have the mechanism of intercalation/deintercalation to store/release energy which is similar to some of the battery-type electrode materials, the absence of clearly crystallographic phase change during charging/discharging processes has make sure that the electrode materials with the mechanism of intercalation pseudocapacitance (such as MnO_2 and Nb_2O_5) have the reaction rate as fast as EDLC electrode (figure 1.8c). For example, it is proposed that MnO_2 electrode material can not only exhibit the mechanism of redox pseudocapacitance but also possess the mechanism of intercalation pseudocapacitance as the equation displayed below: [43, 44, 45]

$$MnO_2 + C^+ + e^- \leftrightarrow MnOOC^+ \qquad (11)$$

Where C^+ represents H^+, Li^+, K^+ or Na^+. In detail, Mn element is reduced from the valence state of 4+ to that of 3+ during the intercalation process, while it is oxidizes back to valence state of 4+ during the deintercalation process. In terms of Nb_2O_5, it is reported that its energy storage process is based on the intercalation/deintercalation of Li^+ which can be described the following equation:[46]

$$Nb_2O_5 + xLi^+ + xe^- \leftrightarrow Li_xNb_2O_5 \qquad (12)$$

1.3.2 Kinetic analysis

In order to thoroughly understand the kinetic differences of EDLC electrode, Battery-type electrode and pseudocapacitive electrode, a method that can quantify the kinetics and deconvolute the diffusion-controlled and surface-controlled processes for electrode materials based on the results from CV curves is firstly proposed by Dunn et al in 2007 as the equation (13) and (14) shown below.[47, 23]

$$i = k_1 v + k_2 v^{1/2} \qquad (13)$$

$$i/v^{1/2} = k_1 v^{1/2} + k_2 \qquad (14)$$

Where $k_1 v$ and $k_2 v^{1/2}$ from equation (13) represent the current contributions from surface-controlled capacitive process and diffusion-controlled process, respectively, and equation (14) is just equation (13) divided by $v^{1/2}$.[48, 49, 50] With these equations and CV curves measured from different scan rates, the current contributions from surface-controlled capacitive process and diffusion-controlled process can be differentiated. Moreover, these equations are simplified as equation (15) and equation (16) is obtained by a log-transformation from equation (15).

$$i_p = a v^b \qquad (15)$$

$$\log(i_p) = b \times \log(v) + \log(a) \qquad (16)$$

Where i_p is the peak current (A) , v is the scan rate (mV/s), and both a and b are the adjustable parameters that can be determined by linear fit calculation of $\log(i_p)$ versus $\log(v)$. Based on the calculated b value, it has two well-defined conditions. If b equals to 0.5, the electrode reaction is a diffusion-controlled process (battery-type electrode material). Whereas, if b equals to 1, the electrode reaction is a surface-controlled process (capacitive electrode material).[51, 52]

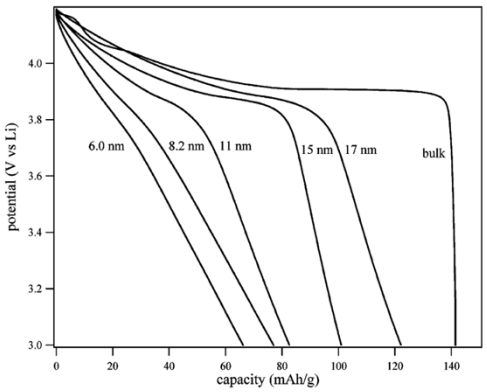

Figure 1.9. The discharge curves of $LiCoO_2$ electrode material with different particle sizes. Reproduced with permission from Ref.[53]

According to figure 1.4d and figure 1.5h, the typical b value of both EDLC electrode and pseudocapacitive electrode is 1, indicating that they are surface-controlled. In figure 1.5d, the b value of battery-type electrode is in a range of 0.5 to 1, which can be explained by the fact that when the battery-type electrode material has nanostructures, the specific surface area of the material can be dramatically increased so that the ion diffusion length can be largely shortened; in this way, the "bulk redox reaction" is basically changed to "surface redox reaction" and, thus, some battery-type electrode material can also exhibit pseudocapacitive behavior. This kind of material can be categorized as intrinsic pseudocapacitive material, compared with extrinsic pseudocapacitive material (such as MnO_2 and RuO_2) whose pseudocapacitive behaviors is not affected by its particle size.[23] For example, as shown in figure 1.9, when the particle size of

$LiCoO_2$ decreases of bulk to 6 nm, the plateaus of these discharge curves (which represent battery-type behavior) gradually disappear and, eventually, near-linear line (which indicates pseudocapacitive behavior) can be found.

1.3.3 Categories of supercapacitors

Table 1.1. Three types of supercapacitors categorized by electrodes with different charge storage mechanisms.

Negative electrode \ Positive electrode	EDLC-type electrode	Pseudocapacitive electrode	Battery-type electrode
EDLC-type electrode	Electric double layer capacitor EDLC	Asymmetric supercapacitor	Hybrid supercapacitor
Pseudocapacitive electrode	Asymmetric supercapacitor	Asymmetric supercapacitor	Hybrid supercapacitor
Battery-type electrode	Hybrid supercapacitor	Hybrid supercapacitor	Not supercapacitor

It is well known that supercapacitors can be categorized into three types (including electric double layer capacitor, asymmetric supercapacitor and hybrid supercapacitor as shown in Table 1.1) based on the electrodes with different mechanisms (including ELDC electrode, battery-type electrode and pseudocapacitive electrode which has discussed above).[53] In detail, electric double layer capacitor is made of two EDLC electrodes; asymmetric supercapacitor is constructed by one pseudocapacitive electrode and one EDLC electrode (or the other kind of pseudocapacitive electrode); hybrid supercapacitor is fabricated with one battery-type electrode and one EDLC electrode (or pseudocapacitive electrode).

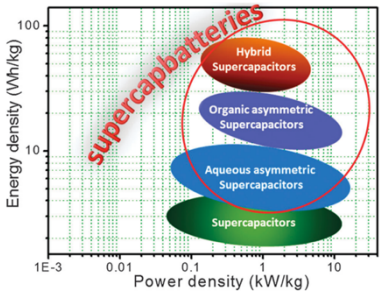

Figure 1.10. Comparison of the electrochemcial performance of symmetric supercapacitors (electric double layer capacitors), asymmetric supercapacitors and hybrid supercapacitors in Ragone plot. Reproduced with permission from Ref.[54]

In addition, according to the Ragone plot shown in figure 1.10, asymmetric supercapacitors can exhibit higher energy density than electric double layer capacitors; and hybrid supercapacitors cannot only provide the highest energy density among these three types of supercapacitors, but also maintain the same level of high power density. In order to realize these experimental results into practical devices, it is worth further research on both asymmetric supercapacitors and hybrid supercapacitors.

1.3.4 Electrolytes used in supercapacitors

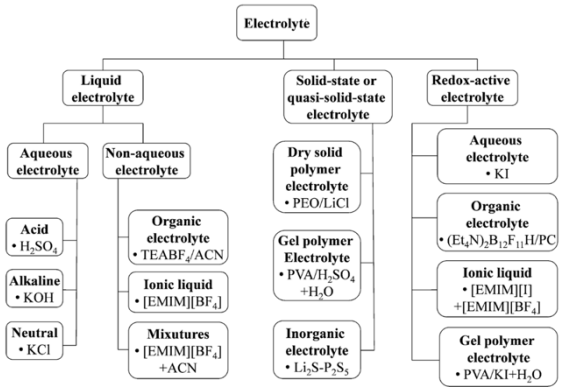

Figure 1.11. Categories of electrolytes used in supercapacitors. Reproduced with permission from Ref.[55]

The electrolytes used in supercapacitor can be classified into about three groups (including liquid electrolyte, solid-state (or quasi-solid-state electrolyte) and redox-active electrolyte) as shown in figure 1.11; and the electrolyte from the third group (which is redox-active electrolyte) can be obtained through modifying the electrolyte from the first two groups.[55] Briefly, in liquid electrolyte, aqueous electrolyte have higher safety and can provide higher ionic conductivity than non-aqueous electrolyte (so that lower internal resistance and higher power density in the prepared device can be achieved); but the working potential window of aqueous electrolyte is much narrower than that of non-aqueous electrolyte due to the thermodynamic limit of water decomposition. Besides, although the usage of solid-state (or quasi-solid-state)

electrolyte can avoid the leakage problem of liquid electrolyte, its complex fabrication processes and relatively low ionic conductivity (comparing with aqueous electrolyte) still need more research to improve. Therefore, the choices of using which type of electrolytes requires more consideration based on the practical applications.

Moreover, it interesting to notify that the redox-active electrolyte, which is based on adding redox active species into liquid electrolyte or solid-state (or quasi-solid-state) electrolyte, can dramatically boost the energy density of the prepared supercapacitor due to the extra charge transfer obtained from the redox reactions. In my opinion, this method is one of the most significant and effective strategies in improving the overall performance of electric double layer supercapacitors.

1. 4 Research objectives

The electrochemical performance of supercapacitors is found to be located at the middle stage of that of conventional capacitors and batteries. In other words, supercapacitors are capable of providing relatively higher energy density than conventional capacitors and higher power density than batteries, respectively. However, based on the performance, they are only suitable for applications requiring short term energy storage and rapid charge/discharge power supply. In order to achieve better overall performance than that of batteries or at least be used as the substitutions of batteries, pursuing higher energy density but maintain the high power density in supercapacitors are necessary. The four projects introduced in this dissertation are the investigations of us towards this ultimate goals.

1. 5 Dissertation overview

In general, multiple strategies have been utilized in order to achieve higher energy density but maintain high power density of supercapacitors.

(1) A hybrid electrochemical capacitor (EC) with enhanced energy density is realized by integrating functionalized carbon nanotube (FCNT) electrodes with redox-active electrolyte that has a neutral pH value (1M Na_2SO_4 and 0.5M KBr mixed aqueous solution). The negative electrode shows an electric double layer capacitor-type behavior. On the positive electrode, highly reversible Br^-/Br_3^- redox reactions take place, presenting a battery-type behavior, which contributes to increase the capacitance of the hybrid cell. The voltage window of the whole cell is extended up to 1.5 V because of the high over-potentials of oxygen and hydrogen evolution reactions in the neutral electrolyte. Compared with raw CNT, the FCNT has better wettability in the aqueous electrolyte and contributes to increase the electric double layer capacitance of the cell. As a result, the maximum energy density of 28.3 Wh kg^{-1} is obtained from the hybrid EC at 0.5 A g^{-1} without sacrificing its power density, which is around 4 times larger than that of the electrical double layer capacitor constructed by FCNT electrodes and 1M Na_2SO_4 electrolyte. Moreover, the discharge capacity retained 86.3 % of its initial performance after 10000 cycles of galvanostatic charge and discharge test (10 A/g), suggesting its long life cycle even at high current loading.

(2) To enhance the energy density of solid-state supercapacitors, a novel solid-state cell, made of redox-active polyvinyl alcohol (PVA) hydrogel electrolytes and functionalized carbon nanotube coated cellulose paper electrodes, was investigated in this work. Briefly, acidic PVA-[BMIM]Cl-Lactic acid-LiBr and neutral PVA-[BMIM]Cl-Sodium acetate-LiBr hydrogel polymer electrolytes are used as catholyte and anolyte, respectively. The acidic condition of the catholyte contributes to suppress the undesired irreversible reaction of Br^- and to extend the oxygen evolution reaction potential to a higher value than the redox potential of Br^-/Br_3^- reaction. The observed Br^-/Br_3^- redox activity at the cathode contributes to enhance the

cathode capacitance. The neutral condition of the anolyte helps extend the operating voltage window of the supercapacitor by introducing hydrogen evolution reaction overpotential to the anode. The electrosoprtion of nascent H on negative electrode also increases the anode capacitance. As a result, the prepared solid-state hybrid supercapacitor shows a broad voltage window of 1.6 V with high coulombic efficiency of 97.6 % and the highest energy density of 16.3 Wh/kg with power density of 932.6 W/kg at 2A/g were obtained. After 10000 cycles of GCD tests at the current density of 10 A/g, it exhibits great cyclic stability with 93.4% retention of the initial capacitance. In addition, robust capacitive performance can also be observed from the solid-state supercapacitor at different bending angles, indicating its great potential as a flexible energy storage device.

(3) Using bimetallic oxide as the electrode material of supercapacitor is emerging as a promising approach to supply better pseudocapacitive performance than that from the electrodes made of corresponding single metal oxides. Herein, Ni-Mn bimetallic oxide nanosheets (Ni-MnBMO) on carbon cloth substrate were synthesized through a facile hydrothermal method. With the help of cyclic voltammetry activation process, the prepared A-Ni-MnBMO electrode exhibits the maximum specific capacitance 574 F g^{-1} (within a potential range of -0.2-1.2 V vs. Ag/AgCl at 1 A g^{-1} after excluding the effects of OER) mainly due to the reversible redox reactions of Mn^{3+}/Mn^{4+}. Moreover, to prove its potential as the positive electrode in a supercapacitor, an asymmetric supercapacitor with a voltage range of 2.1 V is fabricated by using functional carbon nanotube as the negative electrode and 1M Na_2SO_4 as the electrolyte. As a result, the device can deliver a maximum energy density of 27 Wh kg^{-1} (at 0.5 A g^{-1}) and 82.3 % of its initial specific capacitance can be maintained after 8000 cycles of galvanostatic charge and discharge tests at 4 A g^{-1}.

(4) In order to improve the sluggish kinetics of the redox reactions occurring at the battery-type electrodes of hybrid supercapacitors, a Venus flytrap-like hierarchical NiCoMn-O@$NiMoO_4$@C nanosheet arrays electrode material are developed based on three aspects of considerations: 1. The developed NiCoMn-based trimetallic (NiCoMn-O) oxide has better electrical conductivity than any of its bimetallic or monometallic counterparts and the self-decorated nanoneedles on its surface can create more electroactive surface area for electrolyte to access. 2 $NiMoO_4$ layer is the most important redox active material in this composite since its high electrochemical activity in alkaline solution. 3. Carbon protection shell cannot only increase the electric conductivity of the composite but also improve its cycling stability via buffering the volume change during the charge/discharge processes. As a result, the obtained NiCoMn-O@$NiMoO_4$@C electrode can provide a maximum specific capacitance of 2189.5 F/g (at 0.25 A/g) and 81.6 % of its initial specific capacitance can be maintained after 1500 cycles GCD tests (at 6 A/g). The prepared NiCoMn-O@$NiMoO_4$@C//AC hybrid supercapacitor exhibits the maximum energy density of 59.9 Wh/kg (at 0.25 A/g) and its specific capacitance can maintain 88.3 % of its initial value after 3000 cycles GCD tests (at 6 A/g).

1. 6 References

(1) Höök, M.; Tang, X. Depletion of Fossil Fuels and Anthropogenic Climate Change-A Review. Energy Policy 2013, 52, 797–809.

(2) Ibrahim, H.; Ilinca, A.; Perron, J. Energy Storage Systems-Characteristics and Comparisons. Renew. Sustain. Energy Rev. 2008, 12, 1221–1250.

(3) Dincer, I. Renewable Energy and Sustainable Development: A Crucial Review. Renew. Sustain. Energy Rev. 2000, 4, 157–175.

(4) Wang, J.; Dong, S.; Ding, B.; Wang, Y.; Hao, X.; Dou, H.; Xia, Y.; Zhang, X. Pseudocapacitive Materials for Electrochemical Capacitors: From Rational Synthesis to Capacitance Optimization. National Science Review, 2017, 4, 71–90.

(5) Dekel, D. R. Review of Cell Performance in Anion Exchange Membrane Fuel Cells. J. Power Sources 2018, 375, 158–169.

(6) Appleby, A. J. From Sir William Grove to Today: Fuel Cells and the Future. J. Power Sources 1990, 29, 3–11.

(7) Andújar, J. M.; Segura, F. Fuel Cells: History and Updating. A Walk along Two Centuries. Renew. Sustain. Energy Rev. 2009, 13, 2309–2322.

(8) Merle, G.; Wessling, M.; Nijmeijer, K. Anion Exchange Membranes for Alkaline Fuel Cells: A Review. J. Memb. Sci. 2011, 377, 1–35.

(9) Chalk, S. G.; Miller, J. F. Key Challenges and Recent Progress in Batteries, Fuel Cells, and Hydrogen Storage for Clean Energy Systems. J. Power Sources 2006, 159, 73–80.

(10) Yu, X.; Tang, Z.; Sun, D.; Ouyang, L.; Zhu, M. Recent Advances and Remaining Challenges of Nanostructured Materials for Hydrogen Storage Applications. Prog. Mater. Sci. 2017, 88, 1–48.

(11) Roy, P.; Srivastava, S. K. Nanostructured Anode Materials for Lithium Ion Batteries. Journal of Materials Chemistry A, 2015, 3, 2454–2484.

(12) Tarascon, J. M.; Armand, M. Issues and Challenges Facing Rechargeable Lithium Batteries. Mater. Sustain. Energy A Collect. Peer-Reviewed Res. Rev. Artic. from Nat. Publ. Gr. 2010, 414, 171–179.

(13) Qiao, H.; Wei, Q. Functional Nanofibers in Lithium-Ion Batteries. Funct. Nanofibers their Appl. 2012, 197–208.

(14) Zhang, S. S. A Review on Electrolyte Additives for Lithium-Ion Batteries. J. Power Sources 2006, 162, 1379–1394.

(15) Li, Q.; Chen, J.; Fan, L.; Kong, X.; Lu, Y. Progress in Electrolytes for Rechargeable Li-Based Batteries and Beyond. Green Energy Environ. 2016, 1, 1–25.

(16) Wang, F.; Borodin, O.; Ding, M. S.; Gobet, M.; Vatamanu, J.; Fan, X.; Gao, T.; Eidson, N.; Liang, Y.; Sun, W.; et al. Hybrid Aqueous/Non-Aqueous Electrolyte for Safe and High-Energy Li-Ion Batteries. Joule 2018, 2, 927–937.

(17) Suo, L.; Borodin, O.; Gao, T.; Olguin, M.; Ho, J.; Fan, X.; Luo, C.; Wang, C.; Xu, K. "Water-in-Salt" Electrolyte Enables High-Voltage Aqueous Lithium-Ion Chemistries. Science (80-.). 2015, 350, 938–943.

(18) Liu, Z.; Li, H.; Zhu, M.; Huang, Y.; Tang, Z.; Pei, Z.; Wang, Z.; Shi, Z.; Liu, J.; Huang, Y.; et al. Towards Wearable Electronic Devices: A Quasi-Solid-State Aqueous Lithium-Ion Battery with Outstanding Stability, Flexibility, Safety and Breathability. Nano Energy 2018, 44, 164–173.

(19) Zhang, H.; Zhao, H.; Khan, M. A.; Zou, W.; Xu, J.; Zhang, L.; Zhang, J. Recent Progress in Advanced Electrode Materials, Separators and Electrolytes for Lithium Batteries. Journal of Materials Chemistry A, 2018, 6, 20564–20620.

(20) Zhu, R.; Feng, J.; Guo, Z. In Situ Observation of Dendrite Behavior of Electrode in Half and Full Cells. J. Electrochem. Soc. 2019, 166, A1107–A1113.

(21) Lu, J.; Chen, Z.; Pan, F.; Cui, Y.; Amine, K. High-Performance Anode Materials for Rechargeable Lithium-Ion Batteries. Electrochem. Energy Rev. 2018, 1, 35–53.

(22) Pilon, L.; Wang, H.; D'Entremont, A. Recent Advances in Continuum Modeling of Interfacial and Transport Phenomena in Electric Double Layer Capacitors. J. Electrochem. Soc. 2015, 162, A5158–A5178.

(23) Jiang, Y.; Liu, J. Definitions of Pseudocapacitive Materials: A Brief Review. Energy Environ. Mater. 2019, 2, 30–37.

(24) Iro, Z. S.; Subramani, C.; Dash, S. S. A Brief Review on Electrode Materials for Supercapacitor. Int. J. Electrochem. Sci. 2016, 11, 10628–10643.

(25) Schütter, C.; Pohlmann, S.; Balducci, A. Industrial Requirements of Materials for Electrical Double Layer Capacitors: Impact on Current and Future Applications. Adv. Energy Mater. 2019, 9, 1900334.

(26) Shao, Y.; El-Kady, M. F.; Sun, J.; Li, Y.; Zhang, Q.; Zhu, M.; Wang, H.; Dunn, B.; Kaner, R. B. Design and Mechanisms of Asymmetric Supercapacitors. Chem. Rev. 2018, 118, 9233–9280.

(27) Liu, Y. M.; Merlet, C.; Smit, B. Carbons with Regular Pore Geometry Yield Fundamental Insights into Supercapacitor Charge Storage. ACS Cent. Sci. 2019, 5, 1813–1823.

(28) Liu, J.; Wang, J.; Xu, C.; Jiang, H.; Li, C.; Zhang, L.; Lin, J.; Shen, Z. X. Advanced Energy Storage Devices: Basic Principles, Analytical Methods, and Rational Materials Design. Adv. Sci. 2018, 5.

(29) Liu, Y.; Fu, N.; Zhang, G.; Xu, M.; Lu, W.; Zhou, L.; Huang, H. Design of Hierarchical Ni-Co@Ni-Co Layered Double Hydroxide Core–Shell Structured Nanotube Array for High-Performance Flexible All-Solid-State Battery-Type Supercapacitors. Adv. Funct. Mater. 2017, 27, 1605307.

(30) Wang, H.; Liang, M.; Duan, D.; Shi, W.; Song, Y.; Sun, Z. Rose-like Ni3S4 as Battery-Type Electrode for Hybrid Supercapacitor with Excellent Charge Storage Performance. Chem. Eng. J. 2018, 350, 523–533.

(31) Yang, J.; Liu, W.; Niu, H.; Cheng, K.; Ye, K.; Zhu, K.; Wang, G.; Cao, D.; Yan, J. Ultrahigh Energy Density Battery-Type Asymmetric Supercapacitors: NiMoO4 Nanorod-Decorated Graphene and Graphene/Fe2O3 Quantum Dots. Nano Res. 2018, 11, 4744–4758.

(32) Liu, H.; Liu, X.; Wang, S.; Liu, H. K.; Li, L. Transition Metal Based Battery-Type Electrodes in Hybrid Supercapacitors: A Review. Energy Storage Materials, 2020, 28, 122–145.

(33) Yu, F.; Huang, T.; Zhang, P.; Tao, Y.; Cui, F. Z.; Xie, Q.; Yao, S.; Wang, F. Design and Synthesis of Electrode Materials with Both Battery-Type and Capacitive Charge Storage. Energy Storage Materials, 2019, 22, 235–255.

(34) Yao, X.; Zhao, Y.; Castro, F. A.; Mai, L. Rational Design of Preintercalated Electrodes for Rechargeable Batteries. ACS Energy Lett. 2019, 4, 771–778.

(35) Zhang, Y.; Jing, X.; Wang, Q.; Zheng, J.; Jiang, H.; Meng, C. Three-Dimensional Porous V2O5 Hierarchical Spheres as a Battery-Type Electrode for a Hybrid Supercapacitor with Excellent Charge Storage Performance. Dalt. Trans. 2017, 46, 15048–15058.

(36) Wu, J.; Gao, X.; Yu, H.; Ding, T.; Yan, Y.; Yao, B.; Yao, X.; Chen, D.; Liu, M.; Huang, L. A Scalable Free-Standing V 2 O 5 /CNT Film Electrode for Supercapacitors with a Wide Operation Voltage (1.6 V) in an Aqueous Electrolyte. Adv. Funct. Mater. 2016, 26, 6114–6120.

(37) Feng, Y.; Liu, L.; Liang, J.; Yao, W.; Tian, B.; Jiang, C.; Wu, W. Ni(OH)2/NiMoO4 Nanoplates for Large-Scale Fully-Printed Flexible Solid-State Supercapacitors. J. Power Sources 2019, 433, 126676.

(38) Li, R.; Wang, Y.; Zhou, C.; Wang, C.; Ba, X.; Li, Y. Carbon-Stabilized High-Capacity Ferroferric Oxide Nanorod Array for Flexible Solid-State Alkaline Battery – Supercapacitor Hybrid Device with High Environmental Suitability. 2015, 5384–5394.

(39) Lin, J.; Zhong, Z.; Wang, H.; Zheng, X.; Wang, Y.; Qi, J.; Cao, J.; Fei, W.; Huang, Y.; Feng, J. Rational Constructing Free-Standing Se Doped Nickel-Cobalt Sulfides Nanotubes as Battery-Type Electrode for High-Performance Supercapattery. J. Power Sources 2018, 407, 6–13.

(40) Augustyn, V.; Simon, P.; Dunn, B. Pseudocapacitive Oxide Materials for High-Rate Electrochemical Energy Storage. Energy and Environmental Science, 2014, 7, 1597–1614.

(41) Augustyn, V.; Simon, P.; Dunn, B. Pseudocapacitive Oxide Materials for High-Rate Electrochemical Energy Storage. Energy Environ. Sci. 2014, 7, 1597–1614.

(42) Rochefort, D.; Pont, A. L. Pseudocapacitive Behaviour of RuO2 in a Proton Exchange Ionic Liquid. Electrochem. commun. 2006, 8, 1539–1543.

(43) Toupin, M.; Brousse, T.; Bélanger, D. Charge Storage Mechanism of MnO2 Electrode Used in Aqueous Electrochemical Capacitor. Chem. Mater. 2004, 16, 3184–3190.

(44) Tanggarnjanavalukul, C.; Phattharasupakun, N.; Wutthiprom, J.; Kidkhunthod, P.; Sawangphruk, M. Charge Storage Mechanisms of Birnessite-Type MnO2 Nanosheets in Na2SO4 Electrolytes with Different PH Values: In Situ Electrochemical X-Ray Absorption Spectroscopy Investigation. Electrochim. Acta 2018, 273, 17–25.

(45) Subramanian, V.; Zhu, H.; Vajtai, R.; Ajayan, P. M.; Wei, B. Hydrothermal Synthesis and Pseudocapacitance Properties of MnO 2 Nanostructures. J. Phys. Chem. B 2005, 109, 20207–20214.

(46) Kim, J. W.; Augustyn, V.; Dunn, B. The Effect of Crystallinity on the Rapid Pseudocapacitive Response of Nb2O5. Adv. Energy Mater. 2012, 2, 141–148.

(47) Wang, J.; Polleux, J.; Lim, J.; Dunn, B. Pseudocapacitive Contributions to Electrochemical Energy Storage in TiO 2 (Anatase) Nanoparticles. J. Phys. Chem. C 2007, 111, 14925–14931.

(48) Dong, Y.; Li, D.; Gao, C.; Liu, Y.; Zhang, J. A Self-Assembled 3D Urchin-like Ti0.8Sn0.2O2-RGO Hybrid Nanostructure as an Anode Material for High-Rate and Long Cycle Life Li-Ion Batteries. J. Mater. Chem. A 2017, 5, 8087–8094.

(49) Tang, B.; Fang, G.; Zhou, J.; Wang, L.; Lei, Y.; Wang, C.; Lin, T.; Tang, Y.; Liang, S. Potassium Vanadates with Stable Structure and Fast Ion Diffusion Channel as Cathode for Rechargeable Aqueous Zinc-Ion Batteries. Nano Energy 2018, 51, 579–587.

(50) Ding, C.; Huang, T.; Tao, Y.; Tan, D.; Zhang, Y.; Wang, F.; Yu, F.; Xie, Q. Identifying the Origin and Contribution of Pseudocapacitive Sodium Ion Storage in Tungsten Disulphide Nanosheets for Application in Sodium-Ion Capacitors. J. Mater. Chem. A 2018, 6, 21010–21017.

(51) Dong, X.; Chen, L.; Liu, J.; Haller, S.; Wang, Y.; Xia, Y. Environmentally-Friendly Aqueous Li (or Na)-Ion Battery with Fast Electrode Kinetics and Super-Long Life. Sci. Adv. 2016, 2, 1–9.

(52) Zhang, J.; Chen, H.; Sun, X.; Kang, X.; Zhang, Y.; Xu, C.; Zhang, Y. High Intercalation Pseudocapacitance of Free-Standing T-Nb 2 O 5 Nanowires@carbon Cloth Hybrid Supercapacitor Electrodes . J. Electrochem. Soc. 2017, 164, A820–A825.

(53) Okubo, M.; Hosono, E.; Kim, J.; Enomoto, M.; Kojima, N.; Kudo, T.; Zhou, H.; Honma, I. Nanosize Effect on High-Rate Li-Ion Intercalation in LiCoO2 Electrode. J. Am. Chem. Soc. 2007, 129, 7444–7452.

(54) Dubal, D. P.; Ayyad, O.; Ruiz, V.; Gómez-Romero, P. Hybrid Energy Storage: The Merging of Battery and Supercapacitor Chemistries. Chem. Soc. Rev. 2015, 44, 1777–1790.

(55) Zhong, C.; Deng, Y.; Hu, W.; Qiao, J.; Zhang, L.; Zhang, J. A Review of Electrolyte Materials and Compositions for Electrochemical Supercapacitors. Chem. Soc. Rev. 2015, 44, 7484–7539.

CHAPTER 2. FUNCTIONALIZED CARBON NANOTUBE BASED HYBRID ELECTROCHEMICAL CAPACITORS USING NEUTRAL BROMIDE REDOX-ACTIVE ELECTROLYTE FOR ENHANCING ENERGY DENSITY

Xiaohui Tang, Yu Hui Lui, Bolin Chen, Shan Hu*

Department of Mechanical Engineering, Iowa State University, Ames, Iowa, 50010, USA
*Corresponding author Email: shanhu@iastate.edu

Modified from a manuscript published in "J. of Power Sources 352 (2017): 118-126."

Note: The supporting information is shown in APPENDIX A.

2.1 Abstract

A hybrid electrochemical capacitor (EC) with enhanced energy density is realized by integrating functionalized carbon nanotube (FCNT) electrodes with redox-active electrolyte that has a neutral pH value (1M Na_2SO_4 and 0.5M KBr mixed aqueous solution). The negative electrode shows an electric double layer capacitor-type behavior. On the positive electrode, highly reversible Br^-/Br_3^- redox reactions take place, presenting a battery-type behavior, which contributes to increase the capacitance of the hybrid cell. The voltage window of the whole cell is extended up to 1.5 V because of the high over-potentials of oxygen and hydrogen evolution reactions in the neutral electrolyte. Compared with raw CNT, the FCNT has better wettability in the aqueous electrolyte and contributes to increase the electric double layer capacitance of the cell. As a result, the maximum energy density of 28.3 Wh kg^{-1} is obtained from the hybrid EC at 0.5 A g^{-1} without sacrificing its power density, which is around 4 times larger than that of the electrical double layer capacitor constructed by FCNT electrodes and 1M Na_2SO_4 electrolyte. Moreover, the discharge capacity retained 86.3 % of its initial performance after 10000 cycles of galvanostatic charge and discharge test (10 A/g), suggesting its long life cycle even at high current loading.

2.2 Introduction

In order to make the best use of the green renewable energy sources (i.e. wind, solar, etc.), it is crucial to develop reliable energy-storage systems.[1, 2] Electrochemical capacitors (EC) or supercapacitors as one of the promising energy storage systems has attracted extensive research interests due to its long life cycle, high power density, and special bridging characteristics for the power/energy gap between the conventional batteries (with high energy density but low power density) and dielectric capacitors (with high power density but low energy density).[3, 4, 5, 6, 7, 8] However, for supercapacitor to become primary devices for energy storage, further improvement of energy density is still necessary.

$$E = \frac{1}{2} \cdot C_{SP} \cdot V^2 \cdot 1000/3600 \text{ (Wh kg}^{-1}\text{)} \qquad (1)$$

According to formula (1), energy density (E) accumulated in such capacitors is proportional to both the discharge specific capacitance (C_{SP}) and the square of output voltage window (V) which excludes the IR drop.[9] Therefore, by increasing the values of these two parameters, energy density can be definitely improved.

One of the methods for improving the specific capacitance, and consequently energy density, is using electrode materials with high specific surface area (SSA) (such as activated carbon (AC), graphene, carbon nanotube (CNT), etc), since the C_{SP} of an electric double layer capacitor is proportional to the SSA of the electrode as given by $C_{SP} = SSA \cdot \varepsilon/d$, where ε is the relative permittivity of the electrolyte solution, and d is the thickness of the double layer.[10, 11] Zheng et al. synthesized graphene/activated carbon nanosheet composite with high SSA (2106 $m^2\ g^{-1}$) for making supercapacitor electrode, exhibiting high specific capacitance up to 210 F g^{-1} in aqueous electrolyte. Its energy density can reach 22.3 Wh kg^{-1}, which is much higher than that of conventional supercapacitors based on activate carbon (5-6 Wh kg^{-1}).[12] Yan et al. created

supercapacitor by using hierarchical polyaniline nanowires/ordered bimodal mesoporous carbon composites with the SSA of 599 $m^2 g^{-1}$ as electrode material, providing a high specific capacitance of 517 F g^{-1}.[13] Want et al. utilized the three-dimensional flower-like and hierarchical porous carbon material with the SSA of 761.5 $m^2 g^{-1}$ to make the supercapacitor, which can deliver high capacitance of 294 F g^{-1} (2 mV s^{-1}) and high energy density of 15.9 Wh kg^{-1}.[14] Futaba et al. successfully synthesized densely packed and aligned single-walled carbon-nanotube with high specific surface area (1000 $m^2 g^{-1}$) and the energy density of the prepared supercapacitor is as high as 69.4 Wh kg^{-1} in organic electrolyte.[15]

On the other hand, many researchers have investigated hybrid supercapacitor systems by introducing redox reactions into one of the electrodes or electrolytes for achieving higher capacitance. Satish et al. made a lithium-ion hybrid supercapacitor by using carbon-coated $Li_3V_2(PO_4)$ electrode (battery-type half cell) and activated carbon electrode (capacitor-type half cell), delivering maximum energy densities of 27 Wh kg^{-1}.[16] Su et al. found that, by introducing p-phenylenediamine redox species into the electrolyte, the specific capacitance increased from 65 to 156 F g^{-1} at 2 A g^{-1}.[17] Recently, Yamazaki et al. reported a hybrid capacitor by introducing redox active bromide or iodide species to the surface of activated carbon positive electrode (battery-type half cell), showing 5 times higher energy density than conventional aqueous electric double-layer capacitor.[18]

Apart from specific capacitance, the increase of voltage window can also help enhance the energy density. By using non-aqueous electrolytes, large voltage window can be obtained, for example, organic electrolytes (2.5 to 3.0 V) and ionic liquids (up to 4 V).[19] However, they have the disadvantages of high cost, fire hazard, and low conductivity. Aqueous electrolyte, on the other hand, is low-cost, nonflammable, and highly conductive. For the most commonly used

aqueous electrolytes (e.g. KOH, H_2SO_4), the main disadvantage is their relatively low electrochemical window (less than 1.229 V).[20] However, Abbas et al. reported that the use of neutral aqueous electrolytes (such as lithium, sodium and potassium sulfates) can achieve a wider voltage window up to 1.6 V based on activated carbon electrodes owing to the large over-potential of hydrogen evolution.[21] Besides, Demarconnay et al., Wang et al., Tian et al. and Jiménez-Cordero et al. have also claimed similar results.[22, 23, 24, 25] Therefore, using neutral aqueous electrolyte is an encouraging idea for improving the voltage window of supercapacitors.

In this paper, we develop a functionalized carbon nanotube (FCNT) based hybrid ECs by introducing potassium bromide (KBr) into neutral aqueous electrolyte as redox species and using sodium sulfate (Na_2SO_4) as supporting salt. This type of supercapacitor combines the high capacitance introduced by the Br^-/Br_3^- redox pair and the high voltage window enabled by the neutral electrolyte. Hence, a high energy density of 28.3 Wh kg^{-1} (at 0.5 A g^{-1}) is obtained, which is around 4 times larger than that from electric double layer capacitor (EDLC) with the same FCNT electrode materials. The Br^-/Br_3^- redox reaction is very facile, enabling the hybrid capacitors to have power density as high as that of EDLC. Moreover, the discharge capacity of the hybrid capacitor retained 86.3 % of its initial value after 10000 cycles of galvanostatic charge and discharge (GCD) test at 10 A g^{-1}, suggesting its long life cycle even at high current loading.

2.3 Methods

2.3.1 Materials

Carbon nanotube (CNT, Timesnano, single wall, purity: >95%, specific surface area: >1075 m^2 g^{-1}), sodium sulfate (Na_2SO_4, Fisher Chemical, USA, formula weight: 142.04 g mol^{-1}), nitric acid (HNO_3, Fisher Chemical, USA, 68-70% w/w%), sulfuric acid (H_2SO_4, Fisher chemical, USA, 95-98 w/w%), potassium bromide (KBr, Sigma-Aldrich Co. LLC., USA,

formula weight: 119 g mol^{-1}), potassium hydroxide (KOH, Fisher Chemical, USA, formula weight: 56.1056 g mol^{-1}), dimethylformamide (DMF, Sigma-Aldrich Co. LLC., USA, formula weight: 73.09 g moL^{-1}), kapton polyimide film (McMaster-Carr, USA), cation exchange membrane (Membrane International, INC., USA). All chemical reagents are in analytical grade and used as received.

2.3.2 Preparation of electrodes

FCNT was obtained and dispersed into deionized water by using a modified acid treatment dispersion method.[26, 27] Briefly, 100mg raw CNTs were added into 40 mL of acid mixture of sulfuric acid (98 wt. %) and nitric acid (69 wt. %) in a volume ratio of 3:1 and stirred for 10 mins at the temperature of 110 ºC. The mixture was then diluted to 200 mL. The obtained FCNT were collected by membrane filtration and washed by deionized water to remove residual acids. Finally, the FCNT were uniformly dispersed into 50mL of DI water through a 30 mins probe sonication. The concentration of the solution is near 2 mg mL^{-1}. This FCNT water dispersion was then transferred on the surface of kapton film by drop casting method, where kapton film is used as substrate and FCNT is used as both electrode active material and current collector. The mass loading of each electrode is 0.5 mg. The prepared FCNT electrodes were then immersed into 12 M HNO_3 for 30 mins at room temperature and quenched in deionized water. The electrodes made of the hydrophobic raw CNT are also prepared for comparison. Specifically, 10 mg of raw CNT was dispersed into DMF and, after probe sonicating for 30 mins, 20 mL of CNT/DMF dispersion with the concentration of 0.5 mg mL^{-1} was obtained. Then, 1 mL of CNT/DMF dispersion was drop casted on the surface of kapton film. After evaporating the DMF solution, a raw CNT based electrode was obtained.

2.3.3 Voltage windows in different electrolytes

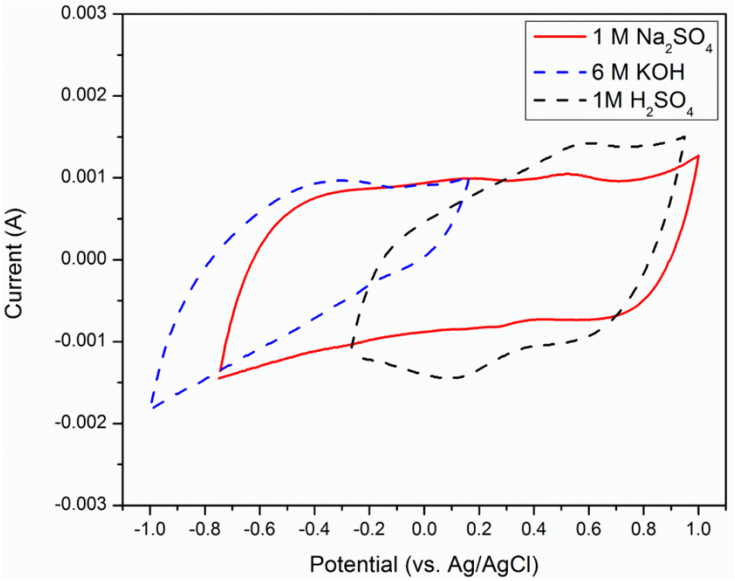

Figure 2.1. Voltage windows measurement of FCNT electrode in the base, acid and neutral electrolytes.

The voltage windows of FCNT electrode in the base (6M KOH, pH=14), acid (1M H_2SO_4, pH=0.36) and neutral (1M Na_2SO_4, pH=6.3) electrolytes are measured in a three-electrode cyclic voltammetry system, respectively, where FCNT is used as working electrode, platinum mesh as counter electrode, and Ag/AgCl (1M KCl) as reference electrode. As shown in figure 2.1, the voltage window of FCNT electrode in neutral electrolyte is -0.75 to 1 V (vs. Ag/AgCl), which is wider than that in acid (-0.276 to 0.952 V vs. Ag/AgCl) and base (-1.062 to 0.167 V vs. Ag/AgCl) electrolytes. This result also gives the maximum and minimum potentials, which could be applied to the FCNT electrode without causing irreversible oxidation and reduction of the electrolyte. According to the standard reduction potential table, the potentials for oxygen evolution reaction (OER) and hydrogen evolutions reaction (HER) in aqueous electrolyte (with pH=0) are 0 and 1.229 V (vs. NHE, or -0.236 and 0.993 V vs. Ag/AgCl), respectively. It is noticed that those potentials will shift by -0.059 V for each pH value increases (as described in formula 2).[28, 29]

$$E = E^0\text{-}0.059\times pH \text{ (V)} \qquad (2)$$

Based on calculation, the exact potentials for HER and OER (at pH=6.3) are -0.3717 and 0.8573 V vs. NHE, or -0.6077 and 0.6213 V vs. Ag/AgCl. And thus, the voltage window should be limited in 1.229 V. However, in 1M Na_2SO_4 neutral electrolyte, it can be observed that the potential for HER is driven to a more negative value -0.75 V (vs. Ag/AgCl) than the calculated -0.6077 V (vs. Ag/AgCl), and the potential for OER is driven to a more positive value of 1 V (vs. Ag/AgCl) than 0.6213 V (vs. Ag/AgCl). With the aforementioned over-potentials of HER and OER, the voltage window is expanded from 1.229 V to 1.5 V.

2.3.4 Assembly of supercapacitor

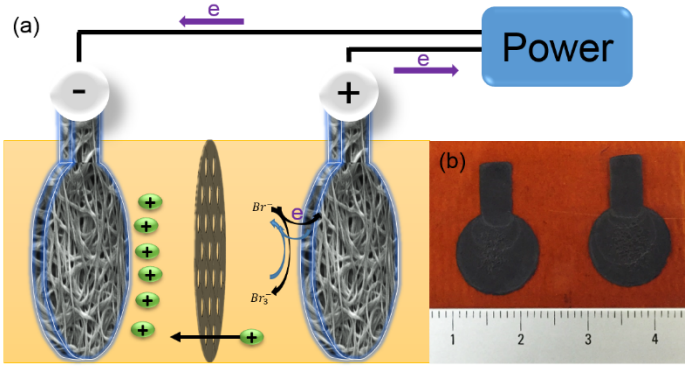

Figure 2.2. (a) The schematic illustration of the redox-active electrolyte supercapacitor.

As shown in figure 2.2a, the two electrodes made of FCNT (figure 2.2b) separated by cation exchange membrane are immersed into 1M Na_2SO_4+0.5M KBr mixed solution (FCNT|1M Na_2SO_4+0.5M KBr|FCNT). Here, KBr is the redox additive, providing Br^- for redox reactions (shown in formula 3), and Na_2SO_4 is used as supporting salt for lowering the internal resistance of electrolyte. The measured pH value of the mixed solution is 6.8, which is close to neutral. The cation exchange membrane (CEM) can block the migration of Br_3^- ions between two

electrodes but allow the transport of cations across the membrane. More detailed discussion of the membrane can be found in figure S2.8 of supplemental material.

$$2Br^- \Leftrightarrow Br_2 + 2e^- \overset{Br^-}{\Leftrightarrow} Br_3^-,\ E^0=0.834\ V\ vs\ Ag/AgCl\ ^{30,31} \quad (3)$$

In addition, for comparing the performance change caused by redox additive, an EDLC made of FCNT electrodes and 1 M Na_2SO_4 electrolyte (FCNT|1M Na_2SO_4|FCNT) is fabricated as well.

2.3.5 Characterization

Scanning electron microscopy (SEM) was recorded on a FEI Quanta 250 FEG Scanning Electron Microscope (FEI, USA). X-ray photoelectron spectroscopy (XPS) measurements were performed on a Kratos Amicus X-ray Photoelectron Spectrometer (Kratos, Japan). The water contact angle was measured by using a Ramé-hart 100-00 Contact Angle Goniometer with a droplet of 1uL deionized water. Cyclic voltammetry (CV), electrochemical impedance spectroscopy (EIS), and galvanostatic charge/discharge (GCD) were obtained on a computer-controlled potentiostat/galvanostat system (Gamry Reference 3000 Electrochemical Station, Gamry, USA). The assembled supercapacitor was tested under a two-electrode system for CV and GCD tests. During the GCD tests, an Ag/AgCl (1M KCl solution) reference electrode was inserted in between the positive and negative electrodes in order to measure the potential profile of each electrode. A three-electrode system, where the working electrode is the FCNT, platinum (Pt) mesh was counter electrode and Ag/AgCl (1M KCl solution) was the reference electrode, was also used for other CV tests. All the electrochemical tests were done at room temperature.

2.3.6 Other calculation equations

Specific capacitance (C_{SP}) and power density (P) are two important parameters for evaluating the performance of supercapacitors. They can be calculated by formula (4) and (5), respectively.

$$\text{Specific capacitance: } C_{SP} = \frac{C}{m} \text{ (F g}^{-1}\text{)} \qquad (4)$$

$$\text{Average power density: } P = \frac{E}{t} \cdot 3600 \text{ (W kg}^{-1}\text{)} \qquad (5)$$

Where C (F) is the capacitance of the supercapacitor, m (g) is the mass of active material on both electrodes, t is the discharge time.[9, 32, 33]

2.4 Results and discussion

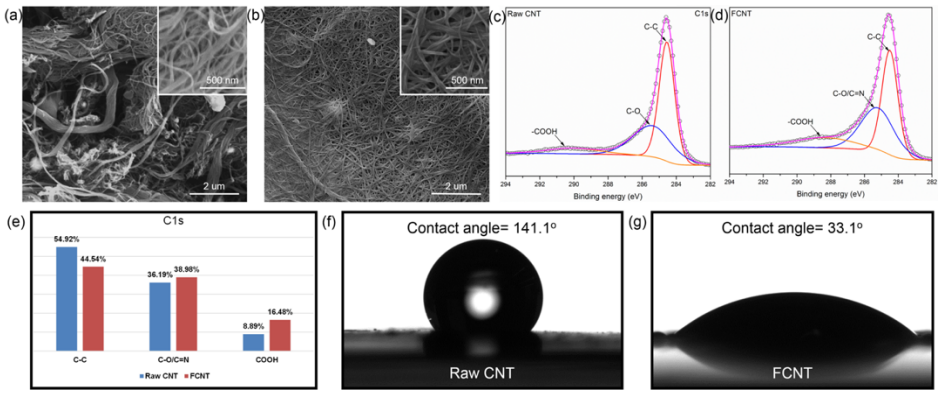

Figure 2.3. SEM images of (a) raw CNT and (b) FCNT with the magnification of 15000 X (Scale bar 2 um). The insets show the enlarged areas with the magnification of 50000 X (scale bar: 500 nm). XPS C1s spectrums of (c) raw CNT and (d) FCNT. (e)The content change of chemical components detected from XPS C1s spectrum. The contact angle measurements of (f) raw CNT and (g) FCNT electrodes.

The morphologies of the as-received raw CNT and FCNT are characterized by SEM. As shown in figure 2.3a, some nanotubes in the raw CNT sample do not exist in the form of individual tubes but agglomerate to each other forming large CNT bundles. However, after acid treatment, most of the CNT bundles untangle into individual nanotubes or smaller bundles (figure 2.3b), which can expose larger specific surface area than that in raw CNT.[34] Moreover,

after acid treatment and drop casting process, the structure of CNTs becomes more densified, which can increase the contact area among CNT networks and, thus, lower the electrode resistance. Furthermore, the wettability of electrode material is improved by introducing carboxyl group through acid treatment, which can increase the contact between electrode surface and aqueous electrolyte.[35, 36, 37] The effective SSA of FCNT and raw CNT electrodes are investigated by using aqueous methylene blue (MB) adsorption method (whose detail information is discussed in Supplemental material). The calculated SSA for FCNT electrode is 1463.077 $m^2 g^{-1}$ and for CNT electrode is 914.353 $m^2 g^{-1}$, revealing that higher SSA in FCNT electrode can be utilized in aqueous solution than that in raw CNT electrode due to better wettability after acid treatment. The electrochemical active surface area (EASA) of FCNT and raw CNT electrodes are also evaluated in Na_2SO_4 aqueous electrolyte through the CV measurements at a narrow potential window (0.3-0.6 V) without any faradic process (figure S2.1), since it is believed that all capacitance here is contributed by EDLC and its value is linearly proportional to the EASA.[38] The testing result shows that FCNT electrode can provide higher electrical double layer specific capacitance than raw CNT electrode and, thus, the EASA of FCNT electrode is larger than that of raw CNT electrode, indicating its better electrochemical performance in aqueous electrolyte, which is consistent with that from MB absorption method. Therefore, even without the contribution of redox active electrolyte, comparing with raw CNT electrode, FCNT electrode with higher EASA (or effective SSA) can produce higher specific capacitance and larger energy density can be achieved. The higher EASA of FCNT is likely ascribed to its better wettability in aqueous electrolyte as proven by the water contact angle test shown in figure 2.3f and g. It can be noticed that, after acid treatment, the surface wettability of

FCNT electrode shows obvious hydrophilic nature with water contact angle of 33.1°, which is better than that of 141.1° for raw CNT electrode.

The atomic concentration of oxygen increases from 2.75 % to 14.18 % after acid treatment suggesting the possibility of introducing carboxyl group (XPS full spectrums are shown in figure S2.2a and b and the corresponding atomic concentration changes are displayed in figure S2.2c and d). Besides, nitrogen doping with the atomic concentration of 0.62 % is also found in FCNT and its narrow-scan spectrum in figure S2.3 reveals that it has three components.[39] Further analysis of C1s narrow-scan spectrum is also implemented. It can be observed that the C1s spectrum from raw CNT (figure 2.3c) can be resolved into three components centered at 284.5 eV (C-C), 285.4 eV (C-O), 290 eV (-COOH) and the same components can be distinguished from FCNT C1s spectrum as well (figure 2.3d).[40, 41, 42, 43] Importantly, the content change of chemical components shown in figure 2.3e indicates that, after acid treatment, the content of carboxyl group increased from 8.89 % to 16.48 %, which is the main reason for the increase of oxygen in FCNT discussed before. With the help of carboxyl group on FCNT surface, the surface wettability of the CNT electrode is improved, which not only offers more accessible electrode surface for ions in the electrolyte, but also increases the ionic conductivity at electrode-electrolyte interfaces.[44] These effects are confirmed by the EIS measurements with FCNT and raw CNT electrodes shown in figure S2.4. Specifically, larger electrical double layer capacitance, indicating larger ion-accessible electrode surface, and smaller charge transfer resistance at electrode-electrolyte interface, due to higher ionic conductivity at the interface, were observed from FCNT-based electrode compared with that from raw CNT one. Detailed discussion of the EIS measurements can be found in the supporting information. Besides, it is worth to notice that the peak around 285.4 eV, which has been ascribed to C-O

bonding in raw CNT, is detected in FCNT (285.22 eV) and a slightly rise of its content (from 36.19 % to 38.98 %) is also found. This result can be explained by the combination effects of carbon atom oxidation during acid treatment and the small amount of nitrogen doping, since C-O and C=N bonds are overlapped with each other.[45]

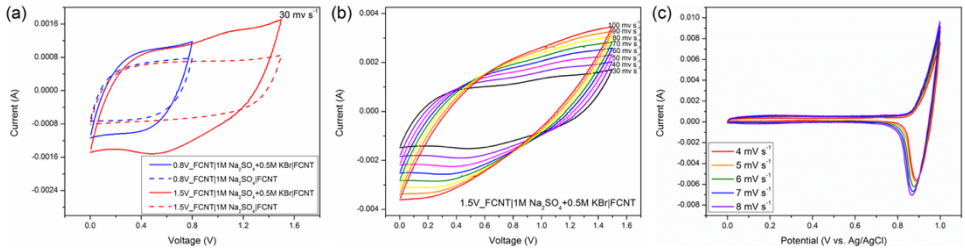

Figure 2.4. (a) CV curves of FCNT|1M Na_2SO_4|FCNT and FCNT|1M Na_2SO_4+0.5M KBr|FCNT supercapacitors up to 0.8 V (blue curve) and 1.5V (red curve). (b) CV curves of FCNT|1M Na_2SO_4+0.5M KBr|FCNT supercapacitor at different scan rates at the voltage window of 1.5 V. (c) CV curves of Br^-/Br_3^- redox reactions on the surface of FCNT electrodes measured in 1M Na_2SO_4+0.5M KBr electrolyte.

The voltage windows of FCNT|1M Na_2SO_4|FCNT and FCNT|1M Na_2SO_4+0.5M KBr|FCNT supercapacitors are detected by CV using a two-electrode system (See figure S2.5). Its result shows that the maximum voltage of each cell is around 1.5 V. CV curves of FCNT|1M Na_2SO_4|FCNT supercapacitor and FCNT|1M Na_2SO_4+0.5M KBr|FCNT supercapacitor are compared by plotting the CV curves together in figure 2.4a in order to evaluate the effects of redox additive (KBr) and different voltage windows. These CV tests are carried out at the scan rate of 30 mV s^{-1} in the voltage window of 0–0.8 V (blue curve) and 0–1.5V (red curve), respectively. As shown in figure 2.4a, FCNT|1M Na_2SO_4|FCNT supercapacitor (dash curve) has rectangular CV curves, which is a characteristic of a pure electrostatic capacitor, indicating fast charge and discharge behavior, while CV curves from FCNT|1M Na_2SO_4+0.5M KBr|FCNT supercapacitor are not rectangular due to the redox reactions (solid curve). Besides, the larger CV area of FCNT|1M Na_2SO_4+0.5M KBr|FCNT supercapacitor compared with that of

FCNT|1M Na_2SO_4|FCNT supercapacitor demonstrates the higher capacitance obtained by adding KBr redox additives. Another reason for this phenomenon is the increased ionic conductivity of the electrolyte after the addition of KBr. Figure 2.4b shows the CV curves of FCNT|1M Na_2SO_4+0.5M KBr|FCNT supercapacitor measured at the voltage window of 0 to 1.5 V from 30 mV s^{-1} to 100 mV s^{-1}. The relatively rectangular shape of these CV curves indicates the stable performance of the cell even at high scan rate. The similar result is obtained from the CV curves of FCNT|1M Na_2SO_4|FCNT supercapacitor shown in figure S2.6. As shown in figure 2.4c, CV tests in a three-electrode system was used to detect the redox reactions of Br^-/Br_3^- on the surface of FCNT electrode in 1M Na_2SO_4+0.5M KBr electrolyte. For different scan rates (4, 5, 6, 7, 8 mV s^{-1}), the CV curves have an incomplete oxidation peak starting roughly from 0.82 to 1 V (vs Ag/AgCl) during the anodic scan.[46] Furthermore, during the cathodic scan, the positions of reduction peaks only slightly shift from o.8895 to 0.8695 V as the scan rate increases from 4 to 8 mV s^{-1}, suggesting the high reversibility of this reaction. These redox peaks are ascribed to the redox reaction of Br^-/Br_3^- as shown in formula 3 rather than the electro- adsorption/desorption of bromide species, because the standard potential for Br^-/Br_3^- redox reaction at pH=6.8 is c.a. 0.834 V vs. Ag/AgCl, which is very close to the observed redox peaks. On the other hand, the electro- adsorption/desorption of Br^- in neutral electrolyte happens at around 0.2 V vs. Ag/AgCl, which is far to the left of the observed redox peaks.[47, 48] Besides, according to formula 3, Br_2 can spontaneously accept Br^- to form Br_3^-, helping Br_2 dissolve into water.[49]

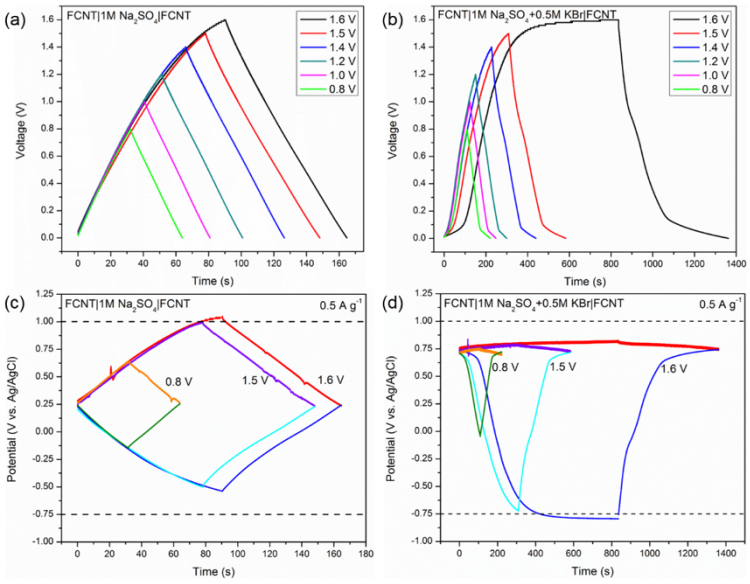

Figure 2.5. GCD of (a) FCNT|1M Na_2SO_4|FCNT and (b) FCNT|1M Na_2SO_4+0.5M KBr|FCNT supercapaciors measured at different voltage window at a current density of 0.5 A g^{-1}. Potential change profiles of positive electrode and negative electrode (vs. Ag/AgCl) obtained from (c) FCNT|1M Na_2SO_4|FCNT and (d) FCNT|1M Na_2SO_4+0.5M KBr|FCNT supercapacitors at the voltage windows of 0.8, 1.5 and 1.6 V (0.5 A g^{-1}).

The GCD of FCNT electrodes in 1M Na_2SO_4 electrolyte (FCNT|1M Na_2SO_4|FCNT) are shown in figure 2.5a. Generally, as the voltage window increases, longer charge and discharge time are required. When the charge/discharge voltage window is increased from 0.8 V to 1.5 V, a series of symmetric GCD curves consisting of linear lines are observed showing their high energy efficiency. In addition, the low value of IR drop (See table S2.2) indicates its low internal resistance, which has been confirmed by the EIS tests. When a voltage window of 1.6 V is applied (black line), the charge curve shows a slightly nonlinear shape, which is asymmetric to the corresponding discharge curve where a straight line is observed, indicating the occurrence of irreversible electrochemical reaction. In the similar GCD tests of FCNT|1M Na_2SO_4+0.5M KBr|FCNT supercapacitor shown in figure 2.5b, with voltage window ranging from 0.8 V to 1.5 V, both of the charge and discharge curves have an obvious nonlinear shape because of the Br^- /Br_3^- reactions, but their overall shape is symmetric. However, the charge curve obtained at the

voltage window of 1.6 V shows a large plateau when the voltage is over 1.5 V (black line), which is not observed in the discharge curve, suggesting a violent irreversible reaction happens. Besides, the discharge time is obviously shorter than the charge time, suggesting its low energy efficiency. The IR drop of this cell also has a low value (See table S2.3) revealing its low internal resistance. Detailed discussions about the energy efficiency and other performances will be done on the later sections.

In order to gain a deeper understanding of the processes involved in the operation of FCNT|1M Na_2SO_4|FCNT and FCNT|1M Na_2SO_4+0.5M KBr|FCNT supercapacitor at different voltage windows, the potential change profiles of positive and negative electrodes have been recorded simultaneously. For FCNT|1M Na_2SO_4|FCNT supercapacitor showed in figure 2.5c, the potential difference applied to the positive and negative electrodes are almost the same at different voltage windows. This result is consistent with the performance of typical symmetric EDLC. In the 1.5 V test, the maximum potential of positive electrode is below the electrolyte oxidation limit (1 V) and the minimum potential of negative electrode is well above the electrolyte reduction limit (-0.75 V), indicating its safe working range. However, in the 1.6 V test, even though the minimum potential of negative electrode is safe, the maximum potential of positive electrode is above the electrolyte oxidation limit, meaning the irreversible oxygen evolution reaction can happen. This result can be used to explain the asymmetric GCD profile (1.6 V) in figure 2.5a. The detailed electrodes potential profile of FCNT|1M Na_2SO_4+0.5M KBr|FCNT supercapacitor is given in figure 2.5d. Unlike the behavior of EDLC, it can be noticed that the potential difference on each electrode is totally different, suggesting their different energy storage mechanisms. On the positive electrode, a battery-type charge/discharge curves are observed, i.e. the positive electrode potential stays constant or changes slightly in a

small range due to the occurrence of fast Br^-/Br_3^- reactions. Notice that the positive electrode potential is always within the electrolyte oxidation limit.[50] On the negative electrode, the capacitor-type behavior is noticed. In the 1.5 V test, the negative electrode potential drops and increases over a wider range than that of the positive one, revealing that most potential change is distributed to the negative electrode. But the minimum value of negative electrode potential does not exceed the electrolyte reduction limit, suggesting its safe working range. Besides, in all profiles, two small plateaus can be observed at the beginning of charge process and the end of discharge process when the negative electrode potential is close to potential on positive electrode where the Br^-/Br_3^- reactions can happen. Hence, these two plateaus are ascribed to the weak Br^-/Br_3^- reactions at the negative electrode. Moreover, when the applied voltage window is 1.6 V, a large plateau can be found on the negative electrode profile (blue line) (figure 2.5d). On this plateau, the negative electrode is charged to a place where its potential is lower than the electrolyte reduction limit. Thus, the irreversible hydrogen evolution reaction, which is destructive to the cell, happens. Results shown in figure 2.5d can further confirm the maximum voltage window of FCNT|1M Na_2SO_4+0.5M KBr|FCNT supercapacitor is 1.5 V instead of 1.6V.

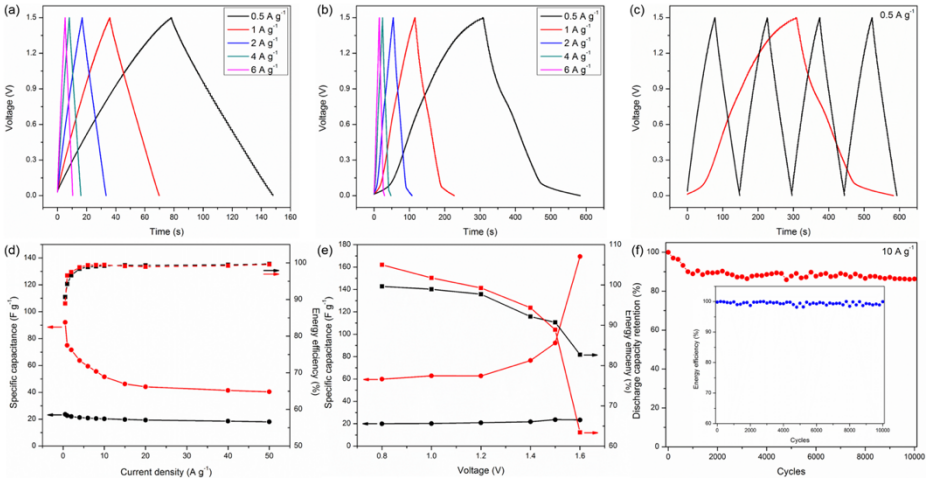

Figure 2.6. GCD profiles of (a) FCNT|1M Na_2SO_4|FCNT and (b) FCNT|1M Na_2SO_4+0.5M KBr|FCNT supercapacitors at different current densities. (c) Galvanostatic charge and discharge

curves of FCNT|1M Na_2SO_4|FCNT and FCNT|1M Na_2SO_4+0.5M KBr|FCNT supercapacitors at a current density of 0.5 A g^{-1}. Discharge specific capacitance (considering the total mass of active material in the supercapacitor) and energy efficiency of FCNT|1M Na_2SO_4|FCNT and FCNT|1M Na_2SO_4+0.5M KBr|FCNT supercapacitors estimated from galvanostatic charge and discharge (d) within a voltage window of 1.5V at different current densities and (e) within various voltage windows at the current density of 0.5 A g^{-1}. (f) GCD curves during a 10000 cycle test at the current density of 10 A g^{-1}. Inset image shows the energy efficiency during the 10000 cycles.

Figure 2.6a and b give the GCD curves of FCNT|1M Na_2SO_4|FCNT supercapacitor and FCNT|1M Na_2SO_4+0.5M KBr|FCNT supercapacitor at different current densities (0.5, 1, 2, 4, 6 A g^{-1}). In figure 2.6a, linear charge and discharge curves are obtained at different current densities because of electrical double-layer behavior. The high symmetric profile and low IR drop (See table S2.4) indicate its high energy efficiency and low internal resistance. As shown in figure 2.6b, the charge and discharge profiles of FCNT|1M Na_2SO_4+0.5M KBr|FCNT supercapacitor are no longer linear, due to the redox reactions from Br^-/Br_3^- redox additives, but the charge and discharge time are still relatively symmetric for all current densities, which is a good sign for having high energy and coulombic efficiency. The IR drop in this supercapacitor is also very small (see table S2.5) indicating low internal resistance even at high current densities. Figure 2.6c shows the comparison of GCD profiles of these two supercapacitors at the current density of 0.5 A g^{-1}. Obviously, the charge and discharge time of FCNT|1M Na_2SO_4+0.5M KBr|FCNT supercapacitor is about 4 times longer than that of FCNT|1M Na_2SO_4|FCNT supercapacitor due to the additional capacitance introduced by Br^-/Br_3^- redox reaction. The discharge specific capacitance (left axis) and energy efficiency (right axis) of FCNT|1M Na_2SO_4|FCNT supercapacitor and FCNT|1M Na_2SO_4+0.5M KBr|FCNT supercapacitor at different current densities are plotted in figure 2.6d. It can be seen that FCNT|1M Na_2SO_4+0.5M KBr|FCNT supercapacitor delivers the maximum specific capacitance of 92.12 F g^{-1} at 0.5 A g^{-1}, which is about 4 times larger than that of FCNT|1M Na_2SO_4|FCNT supercapacitor (23.65 F g^{-1} at

0.5 A g^{-1}). As the current density increases, the specific capacitance of FCNT|1M Na_2SO_4+0.5M KBr|FCNT supercapacitor decreases and stabilizes at 40.38 F g^{-1} at 50 A g^{-1}, which is still more than twice that of FCNT|1M Na_2SO_4|FCNT supercapacitor (18.06 F g^{-1}). The energy efficiency of FCNT|1M Na_2SO_4+0.5M KBr|FCNT supercapacitor increases from 88.9% (0.5 A g^{-1}) to 99.6% (50 A g^{-1}), while the energy efficiency of FCNT|1M Na_2SO_4|FCNT supercapacitor increases from 90.7% (0.5 A g^{-1}) to 99.7% (50 A g^{-1}). At lower current densities, the lower energy efficiency shown on both FCNT|1M Na_2SO_4|FCNT and FCNT|1M Na_2SO_4+0.5M KBr|FCNT supercapacitors than that at higher current density is caused by the occurrence of irreversible oxygen evolution reaction (OER) and hydrogen evolution reaction (HER) during the charge processes, respectively. In detail, as the 1.5 V GCD test (0.5 A g^{-1}) of FCNT|1M Na_2SO_4|FCNT supercapacitor shown in figure 2.5c, the maximum potential of positive electrode is close to 1V, the electrolyte oxidation limit (1 V), meaning that the irreversible OER may happen during the charge process, which can definitely decrease the energy efficiency. However, as the current density increases, the values of IR drop become relatively larger than at lower current (See Table S2.4 and 2.5). Therefore, at high current density, the actual potential of positive electrode (applied potential minus the IR drop) will not reach the electrolyte oxidation limit, and the irreversible OER will not happen. Thus, the high energy efficiency at high current density can be explained. The similar situation may happen in FCNT|1M Na_2SO_4+0.5M KBr|FCNT supercapacitor as well. As its 1.5 V GCD test (0.5 A g^{-1}) shown in figure 2.5d, even though the negative electrode potential does not exceed the electrolyte reduction limit (-0.75 V), its value is still very close to -0.75 V, suggesting the high possibility of occurrence of irreversible HER, which can also decrease the energy efficiency. When the current density increases, the value of IR drop will increase, which causes the actual negative electrode potential to stay above

the electrolyte reduction limit. Therefore, the energy efficiency can have high value at high current density. Figure 2.6e shows the values of discharge capacitance and energy efficiency in both types of supercapacitors as a function of voltage window at the current density of 0.5 A g^{-1}. From 0.8 V to 1.6 V, the values of specific capacitances in FCNT|1M Na_2SO_4|FCNT supercapacitor are stable at around 20 F g^{-1}, while the energy efficiency decreases from 99.66% at 0.8 V to 87.72% at 1.6 V. Comparing with FCNT|1M Na_2SO_4|FCNT supercapacitor, the discharge specific capacitances in FCNT|1M Na_2SO_4+0.5M KBr|FCNT supercapacitor increases dramatically from 59.89 F g^{-1} at 0.8 V to 92.12 F g^{-1} at 1.5 V and then reaches up to 169.5 F g^{-1} at 1.6 V. However, the energy efficiencies decrease to 63.42% at 1.6 V compared with 88.9% at 1.5 V. This result can further confirm that 1.5 V is a better voltage window in this supercapacitor than 1.6 V, since relatively high specific capacitance and energy efficiency can be achieved simultaneously at 1.5 V. It is worth to notice that the energy efficiencies at 0.8V and 1V have exceeded over 100% a little bit. This may be caused by incomplete discharge in the previous GCD cycles. More importantly, the reason for the decrease of energy efficiency when increasing the voltage window in both types of supercapacitors is that, as the voltage window is increased, the negative electrode potential gradually reaches the irreversible hydrogen evolution potential, which leads to energy consumption during the charge process that cannot be recovered later during discharge.[21, 31] The cyclic stability of FCNT|1M Na_2SO_4+0.5M KBr|FCNT supercapacitor is shown in figure 2.6f. It is noticed that about 86.3% of the initial discharge capacity can be retained after 10000 cycles at a high current density of 10 A g^{-1} confirming its good cyclic stability even at high current loading. Besides, figure S2.7 shows the last 5 cycles of this test, indicating the stable GCD profile even after 10000 cycles. The energy efficiency during the 10000 cycles (shown in the inset) are consistently larger than 98%, further suggesting its good

cyclic stability in term of energy efficiency. The high retention of both capacity and energy efficiency can prove the good durability of the capacitor even that has been used for 10000 times GCD tests.

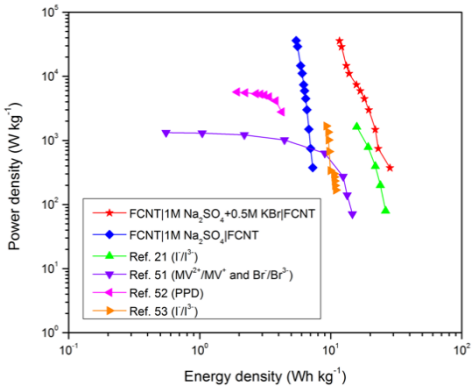

Figure 2.7. Ragone plot of FCNT|1M Na_2SO_4+0.5M KBr|FCNT supercapacitor and FCNT|1M Na_2SO_4|FCNT supercapacitor. Data are overlaid on the performance of different electrochemical devices from the works of other groups.[21, 51, 52, 53]

Ragone plot given in figure 2.7 shows the performance of FCNT|1M Na_2SO_4+0.5M KBr|FCNT supercapacitor (red) and FCNT|1M Na_2SO_4|FCNT supercapacitor (blue) by plotting the energy density vs. power density. It is worth to notice that the output voltage used to calculate the energy density using formula 1 is the discharge voltage after excluding the IR drop. Overall, the energy density of FCNT|1M Na_2SO_4+0.5M KBr|FCNT supercapacitor is more than twice larger than that of FCNT|1M Na_2SO_4|FCNT supercapacitor, while the power density is almost the same. It can be concluded that, by adding the redox reaction into EDLC, the energy density has been greatly increased without sacrificing the power density suggesting its potential for supplying the high energy density and high power density at the same time. The highest energy density of Na_2SO_4+0.5M KBr supercapacitor is 28.3 Wh kg^{-1} obtained 0.5 A g^{-1} with the power density of 372.1 W kg^{-1} and the highest power density in this supercapacitor is 35.8 KW kg^{-1} obtained at 50 A g^{-1} with the energy density of 11.7 Wh kg^{-1}. The performance data from the published literature are also displayed in figure 2.7 for comparison.

2.5 Conclusion

In this work, a functionalized carbon nanotube (FCNT) based hybrid ECs has been developed by adding KBr redox additive into neutral electrolyte. The KBr redox-active electrolyte with a neutral pH value can not only provide additional capacitance due to highly reversible Br^-/Br_3^- reaction, but also extend the voltage window up to 1.5 V owing to the high over-potential for oxygen and hydrogen evolution reactions on FCNT electrode in neutral electrolyte. The introduction of carboxyl functional group to the CNT surface via acid treatment can help improve the wettability of electrode material, which offers more accessible electrode surface for ions in electrolyte, and enhanced ionic conductivity at electrode-electrolyte interfaces. As a result, an energy density of 28.3 Wh kg^{-1} at 0.5 A g^{-1} has been achieved with the redox-mediated hybrid EC, which is around 4 times larger than that from the EDLC with the same FCNT electrodes. It can also be concluded that, by adding the redox reaction into EDLC, the energy density has been greatly increased without sacrificing the power density suggesting its potential for supplying the high energy density and high power density at the same time. Moreover, the discharge capacity retained 86.3 % of its initial performance after 10000 cycles of galvanostatic charge and discharge test (10 A g^{-1}), suggesting its long cycle life even at high current loading. This work offers a possible pathway for achieving both high energy density and high power density with ECs.

2.6 References

(1) Larcher, D.; Tarascon, J.-M. Towards Greener and More Sustainable Batteries for Electrical Energy Storage. Nat. Chem. 2015, 7, 19–29.

(2) Kim, J.-K.; Mueller, F.; Kim, H.; Jeong, S.; Park, J.-S.; Passerini, S.; Kim, Y. Eco-Friendly Energy Storage System: Seawater and Ionic Liquid Electrolyte. ChemSusChem 2016, 9, 42–49.

(3) Hall, P. J.; Bain, E. J. Energy-Storage Technologies and Electricity Generation. Energy Policy 2008, 36, 4352–4355.

(4) Xiang, F.; Mukherjee, R.; Zhong, J.; Xia, Y.; Gu, N.; Yang, Z.; Koratkar, N. Scalable and Rapid Far Infrared Reduction of Graphene Oxide for High Performance Lithium Ion Batteries. Energy Storage Mater. 2015, 1, 9–16.

(5) Chen, H.; Cong, T. N.; Yang, W.; Tan, C.; Li, Y.; Ding, Y. Progress in Electrical Energy Storage System: A Critical Review. Prog. Nat. Sci. 2009, 19, 291–312.

(6) Wu, J.; Yu, H.; Fan, L.; Luo, G.; Lin, J.; Huang, M. A Simple and High-Effective Electrolyte Mediated with p-Phenylenediamine for Supercapacitor. J. Mater. Chem. 2012, 22, 19025–19030.

(7) Faraji, S.; Ani, F. N. The Development Supercapacitor from Activated Carbon by Electroless Plating - A Review. Renew. Sustain. Energy Rev. 2015, 42, 823–834.

(8) Wang, G.; Zhang, L.; Zhang, J. A Review of Electrode Materials for Electrochemical Supercapacitors. Chem. Soc. Rev. 2012, 41, 797–828.

(9) Khomenko, V.; Raymundo-Piñero, E.; Béguin, F. A New Type of High Energy Asymmetric Capacitor with Nanoporous Carbon Electrodes in Aqueous Electrolyte. J. Power Sources 2010, 195, 4234–4241.

(10) Zhang, L. L.; Zhou, R.; Zhao, X. S. Carbon-Based Materials as Supercapacitor Electrodes. J. Mater. Chem. 2009, 38, 2520–2531.

(11) Frackowiak, E.; Béguin, F. Carbon Materials for the Electrochemical Storage of Energy in Capacitors. Carbon N. Y. 2001, 39, 937–950.

(12) Zheng, C.; Zhou, X.; Cao, H.; Wang, G.; Liu, Z. Synthesis of Porous Graphene/Activated Carbon Composite with High Packing Density and Large Specific Surface Area for Supercapacitor Electrode Material. J. Power Sources 2014, 258, 290–296.

(13) Yan, Y.; Cheng, Q.; Zhu, Z.; Pavlinek, V.; Saha, P.; Li, C. Controlled Synthesis of Hierarchical Polyaniline Nanowires/Ordered Bimodal Mesoporous Carbon Nanocomposites with High Surface Area for Supercapacitor Electrodes. J. Power Sources 2013, 240, 544–550.

(14) Wang, Q.; Yan, J.; Wang, Y.; Wei, T.; Zhang, M.; Jing, X.; Fan, Z. Three-Dimensional Flower-like and Hierarchical Porous Carbon Materials as High-Rate Performance Electrodes for Supercapacitors. Carbon N. Y. 2014, 67, 119–127.

(15) Futaba, D. N.; Hata, K.; Yamada, T.; Hiraoka, T.; Hayamizu, Y.; Kakudate, Y.; Tanaike, O.; Hatori, H.; Yumura, M.; Iijima, S. Shape-Engineerable and Highly Densely Packed

Single-Walled Carbon Nanotubes and Their Application as Super-Capacitor Electrodes. Nat. Mater. 2006, 5, 987–994.

(16) Satish, R.; Aravindan, V.; Ling, W. C.; Madhavi, S. Carbon-Coated Li3V2(PO4)3 as Insertion Type Electrode for Lithium-Ion Hybrid Electrochemical Capacitors: An Evaluation of Anode and Cathodic Performance. J. Power Sources 2015, 281, 310–317.

(17) Su, L.; Gong, L.; Lü, H.; Xü, Q. Enhanced Low-Temperature Capacitance of MnO2 Nanorods in a Redox-Active Electrolyte. J. Power Sources 2014, 248, 212–217.

(18) Yamazaki, S.; Ito, T.; Murakumo, Y.; Naitou, M.; Shimooka, T.; Yamagata, M.; Ishikawa, M. Hybrid Capacitors Utilizing Halogen-Based Redox Reactions at Interface between Carbon Positive Electrode and Aqueous Electrolytes. J. Power Sources 2016, 326, 580–586.

(19) Ma, Y.; Chang, H.; Zhang, M.; Chen, Y. Graphene-Based Materials for Lithium-Ion Hybrid Supercapacitors. Adv. Mater. 2015, 27, 5296–5308.

(20) Li, Q.; Chen, J.; Fan, L.; Kong, X.; Lu, Y. Progress in Electrolytes for Rechargeable Li-Based Batteries and Beyond. Green Energy Environ. 2016, 1, 1–25.

(21) Abbas, Q.; Babuchowska, P. Sustainable AC / AC Hybrid Electrochemical Capacitors in Aqueous Electrolyte Approaching the Performance of Organic Systems. 2016, 326, 652–659.

(22) Demarconnay, L.; Raymundo-Piñero, E.; Béguin, F. A Symmetric Carbon/Carbon Supercapacitor Operating at 1.6 v by Using a Neutral Aqueous Solution. Electrochem. commun. 2010, 12, 1275–1278.

(23) Wang, Q.; Yan, J.; Wang, Y.; Ning, G.; Fan, Z.; Wei, T.; Cheng, J.; Zhang, M.; Jing, X. Template Synthesis of Hollow Carbon Spheres Anchored on Carbon Nanotubes for High Rate Performance Supercapacitors. Carbon N. Y. 2013, 52, 209–218.

(24) Tian, Y.; Xue, R.; Zhou, X.; Liu, Z.; Huang, L. Double Layer Capacitor Based on Active Carbon and Its Improved Capacitive Properties Using Redox Additive Electrolyte of Anthraquinonedisulphonate. Electrochim. Acta 2015, 152, 135–139.

(25) Jiménez-Cordero, D.; Heras, F.; Gilarranz, M. A.; Raymundo-Piñero, E. Grape Seed Carbons for Studying the Influence of Texture on Supercapacitor Behaviour in Aqueous Electrolytes. Carbon N. Y. 2014, 71, 127–138.

(26) Hu, S.; Rajamani, R.; Yu, X. Flexible Solid-State Paper Based Carbon Nanotube Supercapacitor. Appl. Phys. Lett. 2012, 100.

(27) Yu, X.; Rajamani, R.; Stelson, K. A.; Cui, T. Fabrication of Carbon Nanotube Based Transparent Conductive Thin Films Using Layer-by-Layer Technology. Surf. Coatings Technol. 2008, 202, 2002–2007.

(28) Tsuchida, N.; Muir, D. M. Potentiometric Studies on the Adsorption of Au(CN)2 and Ag(CN)2 onto Activated Carbon. Metall. Trans. B 1986, 17, 523–528.

(29) Li, L.; Fu, Y.; Manthiram, A. Imidazole-Buffered Acidic Catholytes for Hybrid Li–Air Batteries with High Practical Energy Density. Electrochem. commun. 2014, 47, 67–70.

(30) Wang, Z. S.; Sayama, K.; Sugihara, H. Efficient Eosin Y Dye-Sensitized Solar Cell Containing Br-/Br3-Electrolyte. J. Phys. Chem. B 2005, 109, 22449–22455.

(31) Bard, A. J.; Faulkner, L. R. Electrochemical Methods: Fundamentals and Applications; Wiley New York, 1980; Vol. 2.

(32) Zhang, X.; Wang, L.; Peng, J.; Cao, P.; Cai, X.; Li, J.; Zhai, M. A Flexible Ionic Liquid Gelled PVA-Li2SO4 Polymer Electrolyte for Semi-Solid-State Supercapacitors. Adv. Mater. Interfaces 2015, 2, 1500267.

(33) Hao, C.; Yang, B.; Wen, F.; Xiang, J.; Li, L.; Wang, W.; Zeng, Z.; Xu, B.; Zhao, Z.; Liu, Z.; et al. Flexible All-Solid-State Supercapacitors Based on Liquid-Exfoliated Black-Phosphorus Nanoflakes. Adv. Mater. 2016, 3194–3201.

(34) Zhao, X.; Chu, B. T. T.; Ballesteros, B.; Wang, W.; Johnston, C.; Sykes, J. M.; Grant, P. S. Spray Deposition of Steam Treated and Functionalized Single-Walled and Multi-Walled Carbon Nanotube Films for Supercapacitors. Nanotechnology 2009, 20, 065605.

(35) Balram, A.; Santhanagopalan, S.; Hao, B.; Yap, Y. K.; Meng, D. D. Electrophoretically-Deposited Metal-Decorated CNT Nanoforests with High Thermal/Electric Conductivity and Wettability Tunable from Hydrophilic to Superhydrophobic. Adv. Funct. Mater. 2016, 2571–2579.

(36) Jin, H.; Wang, X.; Gu, Z.; Polin, J. Carbon Materials from High Ash Biochar for Supercapacitor and Improvement of Capacitance with HNO3 Surface Oxidation. J. Power Sources 2013, 236, 285–292.

(37) Wang, W.; Liu, W.; Zeng, Y.; Han, Y.; Yu, M.; Lu, X.; Tong, Y. A Novel Exfoliation Strategy to Significantly Boost the Energy Storage Capability of Commercial Carbon Cloth. Adv. Mater. 2015, 3572-3578.

(38) Liang, H.; Gandi, A. N.; Anjum, D. H.; Wang, X.; Schwingenschlögl, U.; Alshareef, H. N. Plasma-Assisted Synthesis of NiCoP for Efficient Overall Water Splitting. Nano Lett. 2016, acs.nanolett.6b03803.

(39) Podila, R.; Chacón-Torres, J.; Spear, J. T.; Pichler, T.; Ayala, P.; Rao, a. M. Spectroscopic Investigation of Nitrogen Doped Graphene. Appl. Phys. Lett. 2012, 101, 123108.

(40) Shao, Y.; Zhang, S.; Engelhard, M. H.; Li, G.; Shao, G.; Wang, Y.; Liu, J.; Aksay, I. A.; Lin, Y. Nitrogen-Doped Graphene and Its Electrochemical Applications. J. Mater. Chem. 2010, 20, 7491–7496.

(41) Yang, Z.; Xu, M.; Liu, Y.; He, F.; Gao, F.; Su, Y.; Wei, H.; Zhang, Y. Nitrogen-Doped, Carbon-Rich, Highly Photoluminescent Carbon Dots from Ammonium Citrate. Nanoscale 2014, 6, 1890–1895.

(42) Sahoo, M.; Sreena, K. P.; Vinayan, B. P.; Ramaprabhu, S. Green Synthesis of Boron Doped Graphene and Its Application as High Performance Anode Material in Li Ion Battery. Mater. Res. Bull. 2015, 61, 383–390.

(43) Aria, A. I.; Gharib, M. Dry Oxidation and Vacuum Annealing Treatments for Tuning the Wetting Properties of Carbon Nanotube Arrays. J. Vis. Exp. 2013, e50378.

(44) Shen, J.; Liu, A.; Tu, Y.; Foo, G.; Yeo, C.; Chan-Park, M. B.; Jiang, R.; Chen, Y. How Carboxylic Groups Improve the Performance of Single-Walled Carbon Nanotube Electrochemical Capacitors? Energy Environ. Sci. 2011, 4, 4220.

(45) Wang, Y.; Shao, Y.; Matson, D. W.; Li, J.; Lin, Y. Nitrogen-Doped Graphene and Its Application in Electrochemical Biosensing. ACS Nano 2010, 4, 1790–1798.

(46) Chang, Z.; Wang, X.; Yang, Y.; Gao, J.; Li, M.; Liu, L.; Wu, Y. Rechargeable Li//Br Battery: A Promising Platform for Post Lithium Ion Batteries. J. Mater. Chem. A 2014, 2, 19444–19450.

(47) Magnussen, O. M.; Ocko, B. M.; Wang, J. X.; Adzic, R. R. In-Situ X-Ray Diffraction and STM Studies of Bromide Adsorption on Au(111) Electrodes. J. Phys. Chem. 1996, 100, 5500–5508.

(48) Garcia-Araez, N.; Climent, V.; Herrero, E.; Feliu, J.; Lipkowski, J. Thermodynamic Studies of Bromide Adsorption at the Pt(1 1 1) Electrode Surface Perchloric Acid Solutions: Comparison with Other Anions. J. Electroanal. Chem. 2006, 591, 149–158.

(49) Zhao, Y.; Ding, Y.; Song, J.; Peng, L.; Goodenough, J. B.; Yu, G. A Reversible Br2/Br− Redox Couple in the Aqueous Phase as a High-Performance Catholyte for Alkali-Ion Batteries. Energy Environ. Sci. 2014, 7, 1990–1995.

(50) Díaz, P.; González, Z.; Santamaría, R.; Granda, M.; Menéndez, R.; Blanco, C. Enhanced Energy Density of Carbon-Based Supercapacitors Using Cerium (III) Sulphate as Inorganic Redox Electrolyte. Electrochim. Acta 2015, 168, 277–284.

(51) Chun, S.-E.; Evanko, B.; Wang, X.; Vonlanthen, D.; Ji, X.; Stucky, G. D.; Boettcher, S. W. Design of Aqueous Redox-Enhanced Electrochemical Capacitors with High Specific Energies and Slow Self-Discharge. Nat. Commun. 2015, 6, 7818.

(52) Yu, H.; Wu, J.; Lin, J.; Fan, L.; Huang, M.; Lin, Y.; Li, Y.; Yu, F.; Qiu, Z. A Reversible Redox Strategy for SWCNT-Based Supercapacitors Using a High-Performance Electrolyte. Chemphyschem 2013, 14, 394–399.

(53) Sankar, K. V.; Kalai Selvan, R. Improved Electrochemical Performances of Reduced Graphene Oxide Based Supercapacitor Using Redox Additive Electrolyte. Carbon N. Y. 2015, 90, 260–273.

CHAPTER 3. REDOX-ACTIVE HYDROGEL POLYMER ELECTROLYTES WITH DIFFERENT PH VALUES FOR ENHANCING THE ENERGY DENSITY OF THE HYBRID SOLID-STATE SUPERCAPACITOR

Xiaohui Tang, Yu Hui Lui, Abdul Rahman Merhi, Bolin Chen, Shaowei Ding, Bowei Zhang,

and Shan Hu*

Department of Mechanical Engineering, Iowa State University, Ames, Iowa, 50010, USA
*Corresponding author Email: shanhu@iastate.edu

Modified from a manuscript published in "ACS Appl. Mater. Interfaces 9, no. 51 (2017): 44429-44440."

Note: The supporting information is shown in APPENDIX B.

3.1 Abstract

To enhance the energy density of solid-state supercapacitors, a novel solid-state cell, made of redox-active polyvinyl alcohol (PVA) hydrogel electrolytes and functionalized carbon nanotube coated cellulose paper electrodes, was investigated in this work. Briefly, acidic PVA-[BMIM]Cl-Lactic acid-LiBr and neutral PVA-[BMIM]Cl-Sodium acetate-LiBr hydrogel polymer electrolytes are used as catholyte and anolyte, respectively. The acidic condition of the catholyte contributes to suppress the undesired irreversible reaction of Br^- and to extend the oxygen evolution reaction potential to a higher value than the redox potential of Br^-/Br_3^- reaction. The observed Br^-/Br_3^- redox activity at the cathode contributes to enhance the cathode capacitance. The neutral condition of the anolyte helps extend the operating voltage window of the supercapacitor by introducing hydrogen evolution reaction overpotential to the anode. The electrosoprtion of nascent H on negative electrode also increases the anode capacitance. As a result, the prepared solid-state hybrid supercapacitor shows a broad voltage window of 1.6 V with high coulombic efficiency of 97.6 % and the highest energy density of

16.3 Wh/kg with power density of 932.6 W/kg at 2A/g were obtained. After 10000 cycles of GCD tests at the current density of 10 A/g, it exhibits great cyclic stability with 93.4% retention of the initial capacitance. In addition, robust capacitive performance can also be observed from the solid-state supercapacitor at different bending angles, indicating its great potential as a flexible energy storage device.

3.2 Introduction

Among numerous electrochemical energy storage devices, supercapacitors have drawn a lot of research attentions due to their higher energy density than dielectric capacitors and higher power density than batteries.[1, 2] However, traditional supercapacitors using liquid-state electrolytes fail to meet the energy storage requirement of emerging portable and wearable electronics, due to their bulkiness and risk of electrolyte leakage.[3, 4] Therefore, much research effort has been devoted to developing supercapacitors using solid-state electrolytes.

In comparison to liquid-state electrolytes (i.e. aqueous and organic solutions of salts or ionic liquids), solid-state electrolytes (e.g. dry solid polymer electrolytes, gel polymer electrolytes, micro/nano-composite polymer electrolytes, etc.) have the advantages of stabilized form and thus minimal need for device packaging (because of the solid-state property that can eliminate the risk of electrolyte leakage).[5, 6, 7] Among those, hydrogel polymer electrolytes, constructed by a combination of polymeric cross-linked network and aqueous solution, stand out for their excellent ionic conductivity, low fire hazard, and low cost. Comparing with dry solid-polymer electrolytes with the ionic conductivity of 10^{-8} and 10^{-7} S/cm, hydrogel polymer electrolytes can provide ionic conductivity as high as ca. 10^{-3} S/cm without losing their structural stability.[6, 8] For instance, Chodankar et al. successfully made a PVA-$LiClO_4$ hydrogel polymer electrolyte with an ionic conductivity of 48 mS/cm.[9] Zhang et al. systematically investigated the

PVA-[BMIM]Cl-Li_2SO_4 hydrogel polymer electrolyte and, after optimizing the content of [BMIM]Cl and Li_2SO_4, a free-standing hydrogel polymer with the maximum ionic conductivity of 37 mS/cm was achieved.[10]

So far, various electric double layer supercapacitors made of solid-state hydrogel polymer electrolytes have been reported in literatures. For example, Batisse et al. developed an electric double layer supercapacitor by using activated carbon as active electrode material and PVA-Na_2SO_4 hydrogel as electrolyte. The cell can supply an energy density of 13 Wh/Kg and a power density of 106 W/Kg at the current of 0.2 A/g.[11] Besides, Xu et al. used graphene hydrogel film electrodes and PVA-H_2SO_4 hydrogel polymer electrolyte to make an electric double layer supercapacitor with an energy density of 6.5 Wh/Kg and a power density of 287.4 W/Kg at the current density of 1 A/g.[12]

Recently, many research groups have demonstrated that solid-state supercapacitor's energy density can be drastically boosted by adding redox-active species into the hydrogel polymer electrolyte. For example, Sun et al. made a PVA-H_2SO_4-ARS (Alizarin Red S) hydrogel that was used as electrolyte and sandwiched by two activated carbon electrodes. The testing result shows that the prepared solid-state supercapacitor has an energy density of 25 Wh/Kg with a power density of 1581 W/Kg at the current density of 2 A/g.[13] Fan et al. developed a flexible supercapacitor by utilizing activated carbon as electrodes and PVA-H_2SO_4-KI-$VOSO_4$ hydrogel as electrolyte. The resulting energy density is 25.4 Wh/Kg with corresponding power density of 190 W/Kg at the current density of 0.5 A/g.[14] Li et al. reported a supercapacitor made of carbon cloth coated by PVA-PANI hydrogel as redox-active electrolyte and PVA-H_2SO_4 hydrogel as separator. The test results showed that an energy density of 18.7 Wh/Kg and a power density of 107 W/Kg were obtained at the current density of 0.25 A/g.[15]

$$2Br^- \Leftrightarrow Br_2 + 2e^- \overset{Br^-}{\Longleftrightarrow} Br_3^-, \text{E}^0\text{=1.066 V vs. NHE} \quad (1)$$

Bromide/tribromide (Br^-/Br_3^-) redox reaction (equation 1), which is known as an efficient and reversible reaction and has a very high redox potential (1.066 V vs. NHE), is promising as a redox additive to the catholyte for enhanced cathode capacitance.[16, 17, 18, 19, 20, 21] However, at neutral condition, the redox potential of Br^-/Br_3^- is above the thermodynamic oxygen evolution reaction (OER) potential, which may hinder the occurrence of this reaction. Moreover, under neutral and base condition, Br^- could be irreversibly oxidized to the unstable BrO^-, reducing the cyclability of the cathode. Fortunately, this highly irreversible reaction has been shown to be greatly suppressed in acidic mediums. Thus, it is necessary to create an acidic condition in the catholyte for dual purposes: (1) to shift the OER potential positively and ensure that Br^-/Br_3^- redox reaction can proceed before OER occurs, and (2) to suppress the formation of unstable BrO^-.

Another strategy to enhance the energy density of supercapacitors using hydrogel polymer electrolyte is to extend the voltage window. For catholyte with Br^-/Br_3^- redox activity, the cathode potential will be pinned at the redox potential of Br^-/Br_3^-, and most of the potential change happens at the anode. To achieve extended voltage window, it is necessary to extend the anode's working potential range, which is inevitably limited by the hydrogen evolution reaction (HER) for hydrogel electrolytes. It has been reported that carbon material can exhibit a high overpotential of HER when it is used as anode in neutral medium.[22] Therefore, the use of neutral anolyte having high HER overpotential together with acidic catholyte with Br^-/Br_3^- redox reaction in a supercapacitor can promise enhanced energy density, by taking advantages of both high capacitance contributed by reversible Br^-/Br_3^- redox reaction on the positive electrode, and high operating voltage window mostly extended by the negative electrode. Similar design

has been proven in a liquid-state hybrid supercapacitor by Frackowiak's group. Briefly, it has been reported that, by operating positive electrode in KI aqueous solution (which is a neutral electrolyte with redox additive) and negative electrode in KOH solution (which is an alkaline electrolyte for electric double layer capacitor), the working voltage of the supercapacitor can be increased to 1.5 V and the calculated energy density is greatly improved.[23] Moreover, solid-state electrolytes offer unique advantages for implementing electrolytes with different pH values than liquid-state electrolytes. Because of their stabilized forms, it is easier to separate solid-state electrolytes than to separate their liquid counterparts when assembling them into a supercapacitor cell. Effective separation of the catholyte and anolyte is essential for achieving wide voltage window and low self-discharge as discussed in details in Section 3.

In the present work, we develop the acidic PVA-[BMIM]Cl-Lactic acid-LiBr (PVA-BC-LA-LiBr) hydrogel catholyte and neutral PVA-[BMIM]Cl-Sodium acetate-LiBr (PVA-BC-SA-LiBr) hydrogel anolyte with high conductivity and great mechanical properties by using a combination of solution casting and freeze-thaw methods. In detail, polyvinyl alcohol (PVA) was used as host polymer and 1-Butyl-3-methylimidazolium chloride ([BMIM]Cl) was the plasticizer. Lactic acid ($CH_3CH(OH)COOH$) and sodium acetate (CH_3COONa) are the water-soluble components utilized to adjust the pH value of hydrogels. Besides, lithium bromide (LiBr) salt is not only a redox additive, providing Br^-/Br_3^- redox pair, but also the supporting salt for increasing the ionic conductivity of hydrogel. The amount of LiBr added into the hydrogel are optimized to achieve the highest ionic conductivity. Finally, the prepared gel electrolytes are sandwiched by functionalized carbon nanotube (FCNT) coated cellulose paper electrodes with high hydrophilicity to form a flexible supercapacitor device and Nafion 117 is used as the separator. The electrochemical performances are characterized and analyzed in detail.

3.3 Methods

3.3.1 Materials

Carbon nanotube (CNT, product name: TNSAR, Timesnano, single wall, purity: >95%, specific surface area: >1075 m^2g^{-1}), poly(vinyl alcohol) (PVA, Sigma-Aldrich Co. LLC., USA, molecular weight: 89000-98000 g mol^{-1}, 99 % hydrolysis), 1-Butyl-3-methylimidazolium chloride ([BMIM]Cl, Sigma-Aldrich Co. LLC., USA, molecular weight: 174.67 g mol^{-1}), sodium acetate (CH_3COONa, Fisher Chemical, USA, formula weight: 82.0343 g mol^{-1}), lithium bromide (LiBr, Sigma-Aldrich Co. LLC., USA, formula weight: 86.845 g mol^{-1}), lactic acid ($CH_3CH(OH)COOH$, Fisher Chemical, USA, formula weight: 90.08 g mol^{-1}, 85 % w/w), Nafion 117 membrane (Fuel Cell Store, USA), Ag wire (diameter: 0.375 mm, Warner Instruments). All chemical reagents are in analytical grade and used as received.

3.3.2 Preparation of PVA based hydrogel polymer electrolytes and FCNT-coated cellulose paper (FCP) electrode

PVA based hydrogel polymer electrolytes were prepared by a combination of solution casting and freeze-thaw methods. For catholyte, 106 mg lactic acid, 9 g [BMIM]Cl and a certain amount of LiBr were fully dissolved in 10 mL deionized water. LiBr is served as the redox additive which provides sufficient Br^- for the redox reaction shown in equation 1. The obtained solution has a pH value of 1.42 (acidic). After that, 3 g PVA was added into the mixed solution under agitation at 90 ^oC until it becomes homogeneous. For anolyte, 82 mg CH_3COONa, 9 g [BMIM]Cl and a certain amount of LiBr were fully dissolved in 10 mL deionized water. The obtained solution has a pH value of 7.03 (neutral). Then, similarly, 3 g PVA was added into the mixed solution under agitation at 90 ^oC until a homogeneous solution was formed. Finally, the prepared PVA based solutions were poured into a plastic petri dish and frozen at -80 ^oC for 12 h.

After thawing for 30 min, the free-standing acidic PVA-BC-LA-LiBr and neutral PVA-BC-SA-LiBr hydrogels were obtained.

The active material of the electrodes is the functionalized carbon nanotube (FCNT) with enhanced hydrophilicity which has been described in detail in our previous work.[19] The high hydrophilicity of FCNT can help increase the contact between FCP electrodes and PVA hydrogel electrolytes.[24] The FCNT-coated cellulose paper (FCP) electrodes are prepared by simply drop-casting the FCNT onto the cellulose papers. After that, copper foils were attached onto the prepared FCP electrodes through silver paste and used as electric connection for electrochemical tests. According to the measurement (figure S3.1), the weight of the single electrode is around 30 mg and the area of the electrode is 2x3 cm^2. It is necessary to mention that, for single electrode, the active area that contacts with the electrolyte is 2x2 cm^2 and its corresponding mass loading of the active material is about 0.5 mg. The extra 1x2 cm^2 area of the electrode is used to make connection with copper foil through silver paste and protected by plastic film and is considered inactive for energy storage.

3.3.3 Assembly of the solid-state hybrid supercapacitor

The solid-state hybrid supercapacitor was fabricated through a simple freeze-thaw method. In detail, two pieces of FCP electrodes were soaked into the acidic and neutral PVA solutions, respectively, under a vacuum condition for 2 hrs, in order to make sure that the PVA solutions were fully adsorbed by the electrode material. Then, a Nafion 117 membrane (as separator) was inserted in between the two prepared FCP electrodes and the sandwich sample was frozen in the refrigerator at -80 ^oC for 12 hrs. After thawing for 30 min at room temperature, the solid-state hybrid supercapacitor was obtained (The schematic illustration of this supercapacitor is shown in figure 3.3 of section 3).

3.3.4 Instrumental Characterization

Thermal gravimetric analysis (TGA), differential scanning calorimetry (DSC) and mass spectrum (MS) data were collected from a Netzsch STA449 F1 DSC/TGA-MS/IR (Netzsch, USA). Scanning electron microscopy (SEM) was recorded on a FEI Quanta 250 FEG Scanning Electron Microscope (FEI, USA). Transmission electron microscopy (TEM) image was collected by 2007 JEOL 2100 200 kV scanning and transmission electron microscope. Raman spectroscopy was tested by using DXR Disperse Raman Microscope (Thermal scientific inc., USA). Cyclic voltammetry (CV), electrochemical impedance spectroscopy (EIS) and galvanostatic charge and discharge (GCD) were obtained on a potentiostat/galvanostat system (Gamry Reference 3000 Electrochemical Station, Gamry, USA). Before the tests, all prepared supercapacitors were activated by running a 5-cycle CV (0-1.6 V) at the scan rate of 30 mV/s and, then, pre-charging the cell at a constant current density of 2 A/g to 1.6 V for 1 h. After activation, large amount of Br_3^- were generated on the surface of positive electrode (as shown in equation 1). All the electrochemical tests were done at room temperature.

3.3.5 Other calculation equations

The average specific capacitance of the supercapacitor (C_{cell}, F/g), coulombic efficiency (ε_c), energy density (E, Wh/kg) and average power density (P, W/kg) were calculated according to the following equations.

$$C_{cell} = \frac{2I\int Vdt}{V^2|_{V_i}^{V_f}} \quad \textbf{(2)}$$

$$\varepsilon_c = \frac{I \cdot t_{discharge}}{I \cdot t_{charge}} = \frac{t_{discharge}}{t_{charge}} \quad \textbf{(3)}$$

$$E = I\int Vdt \quad \textbf{(4)}$$

$$P = \frac{E}{t} \quad \textbf{(5)}$$

where I is the current density (A/g, the total mass loading of active material is 1 mg for one cell), t is the time ($t_{discharge}$ is the discharge time and t_{charge} is the charge time), V is the voltage (V_i is the initial voltage and V_f is the final voltage) during the discharge process.[25, 26, 27]

3.4 Results and discussion

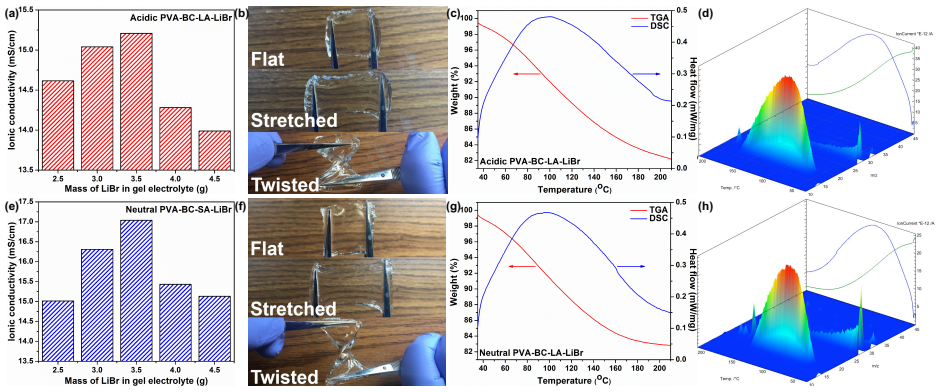

Figure 3.1. (a) Ionic conductivity of the acidic PVA-BC-LA-LiBr hydrogel with different amounts of LiBr and (b) photographs of the flexible acidic PVA-BC-LA-LiBr hydrogel. (c) TGA-DSC and (d) 3D mass spectrum (with respect to temperature) of acidic PVA-BC-LA-LiBr hydrogel. (e) Ionic conductivity of the neutral PVA-BC-SA-LiBr hydrogel with different amounts of LiBr and (f) photographs of the flexible neutral PVA-BC-SA-LiBr hydrogel. (g) TGA-DSC and (h) 3D mass spectrum (with respect to temperature) of neutral PVA-BC-SA-LiBr hydrogel.

In order to optimize the performance of the supercapacitor, the ionic conductivity of the electrolyte has to be adjusted to the best value by tuning the content of the LiBr salt. It is reported that the ionic conductivity of the solid-state hydrogel polymer electrolyte can be measured by using EIS test and the related calculation equation is

$$\sigma = \frac{L}{R_s \times S} \times 1000 \text{ (mS/cm)} \qquad \textbf{(6)}$$

Where L (cm) and S (cm^2) is the distance between the two testing stainless steel electrodes and the geometric area of the electrode/electrolyte interface, respectively.[28] R_s (Ω) is the resistance of the solid-state electrolyte, which is measured from the value of intercept of Nyquist plot with the real axis through EIS test.[29] As shown in figure 3.1a, the ionic conductivity of acidic PVA-BC-LA-LiBr hydrogel depends on the content of LiBr at room temperature. It can

be observed that, with the increase of LiBr from 2.5 to 3.5 g, the ionic conductivity increases quickly and reaches the highest value of 15.2 mS/cm, when the amount of LiBr is 3.5 g. It is because that LiBr here can provide free ions for improving the ionic conductivity of the hydrogel. However, as the amount of added LiBr is beyond 3.5 g (from 3.5 to 4.5 g), the ionic conductivity of the electrolyte will decrease gradually, which can be explained by the reason that higher amount of LiBr can cause the aggregation of free ions and the crystallization of LiBr in hydrogel polymer electrolyte system, which results in the decrease of ionic conductivity.[30, 31] Figure 3.1b illustrates that the prepared acidic PVA-BC-LA-LiBr hydrogel can be stretched and twisted and still return to its original form, revealing its excellent mechanical property and great potential for making flexible devices. To study the condition of water in acidic PVA-BC-LA-LiBr hydrogel, TGA and DSC analysis was performed in the argon atmosphere from room temperature to 210 ºC at a heating rate of 5 ºC/min. As the TGA curve shown in figure 3.1c, starting at 35 ºC, it can be observed that the mass of the hydrogel keeps dropping and maintains 91.9 % of its initial weight when the temperature reaches 100 ºC. From the DSC curve, the maximum heat flow is also located at around 100 ºC, which is corresponding to the boiling point of water. After 100 ºC, the mass of the hydrogel still drops at a high rate and reaches a plateau with 82.1 % of its initial weight at the final temperature of 210 ºC. The components of the mass loss at different temperatures are detected by the mass spectrum versus temperature shown in figure 3.1d. It can be recognized that, the majority of the mass loss during the test is contributed by the single component with the mass weight of 18 (from about 40 to 190 ºC), which is ascribed to water molecules (figure S3.2a). It is worth to notice that, besides the peak value of mass loss at around 100 ºC, the water molecules continue to come out from the hydrogel until 170 ºC, which is much higher than the boiling point of water. This phenomenon can help prove that,

besides the free water, there is also another type of water called freezable bound water existing in the hydrogel, which plays a significant role in maintaining the flexibility and stiffness of the PVA based hydrogel.[32, 33, 34] In addition, the same tests have also been done on the neutral PVA-BC-SA-LiBr hydrogel shown in figure 3.1e-h. From figure 3.1e, the maximum ionic conductivity (17 mS/cm) of the neutral PVA-BC-SA-LiBr hydrogel is obtained when 3.5 g of LiBr is added. Figure 3.1f shows that neutral PVA-BC-SA-LiBr hydrogel has the same mechanical property as acidic PVA-BC-LA-LiBr hydrogel. From the TGA, DSC and mass spectrum shown in figure 3.1g and h, the mass loss trend is similar to the result from neutral PVA-BC-SA-LiBr hydrogel and, at 210 °C, 82.8% of its initial weight is maintained. The main part of mass loss is found from 50 to 170 °C and can be attributed to water molecules as well (figure S3.2b).

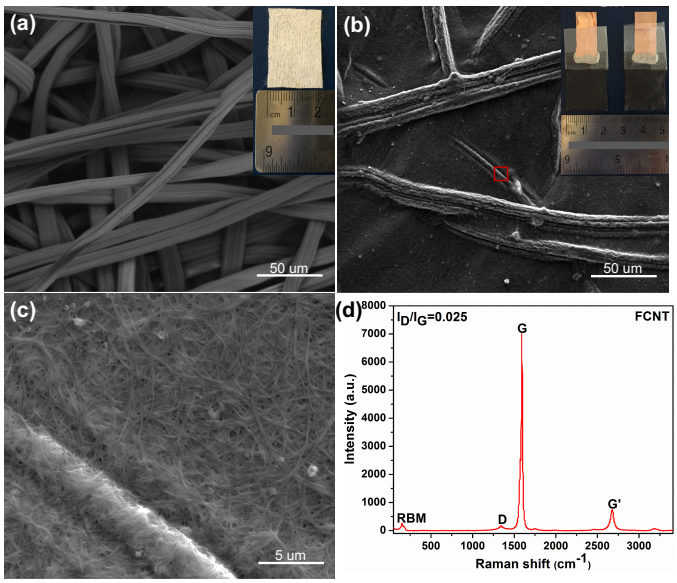

Figure 3.2. (a) SEM image (500 x, scale bar: 50 um) and photograph (inset) of cellulose paper. (b) SEM image (500 x, scale bar: 50 um) and photograph (inset) of FCNT-coated cellulose paper electrodes. (c) High-magnification SEM image (5000 x, scale bar: 5 um) of the area enclosed by the red box from figure 3.2b and (d) Raman spectroscopy of FCNT.

The structure and morphology of the FCP electrode are characterized by SEM. Figure 3.2a shows the SEM image of the pure cellulose paper (The photograph of cellulose paper is displayed in the inset). It can be observed that the cellulose paper is made of cross-linked fibers with the average diameter of about 15 um. After the drop-casting process, as shown in figure 3.2b, the flexible and conductive FCP electrodes are prepared (displayed in the inset) and FCNT well infiltrates into the macroporous structure of cellulose fibers, which grants the high conductivity to the cellulose paper. Furthermore, figure 3.2c gives a high-magnification SEM image of the area enclosed by the red box from figure 3.2b. It is recognized that FCNT not only infiltrates into interspace of the cellulose network, but also covers the surface of the cellulose fibers, revealing the good adsorption of FCNT into cellulose papers merely through an easy drop-casting method. Besides, figure 3.2d shows the Raman spectroscopy of FCNT at 532 nm. It can be observed that the peak at around 153 cm^{-1} can be ascribed to the radical breathing mode and the peak at 1588 cm^{-1} is G mode. The vibration at 1342 cm^{-1} can be attributed to D mode, which reflects the degree of structural detects.[35, 36] The intensity ratio of D mode to G mode (I_D/I_G) of the FCNT is 0.025, which is marginally higher than that (I_D/I_G=0.018) of raw CNT displayed in figure S3.3, indicating the functionalization only affected the structure of CNT slightly. In addition, the single-wall structure of FCNT is confirmed by TEM as shown in figure S3.4.

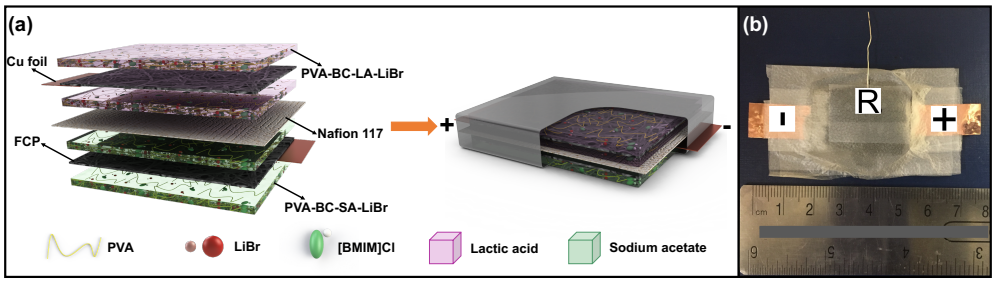

Figure 3.3. (a) Schematic illustration of the supercapacitor and (b) its corresponding photograph.

The schematic of supercapacitor (SC) made of asymmetric acid and neutral electrolytes (hereafter denoted as LA-SA hybrid SC) are shown in figure 3.3a. Briefly, a catholyte (which is acidic PVA-BC-LA-LiBr hydrogel), an anolyte (which is neutral PVA-BC-SA-LiBr hydrogel), and a separator (made of Nafion 117 membrane) are sandwiched between two FCP electrodes. Then, an Ag wire was inserted into the catholyte and used as a pseudo-reference electrode. After the freeze-thaw process for overnight, the cell is wrapped by a plastic tape for protection purpose and its photograph is shown in figure 3.3b. For comparison purpose, a cell with only acid electrolyte (hereafter denoted as LA hybrid SC) and a cell made of neutral electrolyte (hereafter denoted as SA hybrid SC) are also prepared for further tests, respectively.

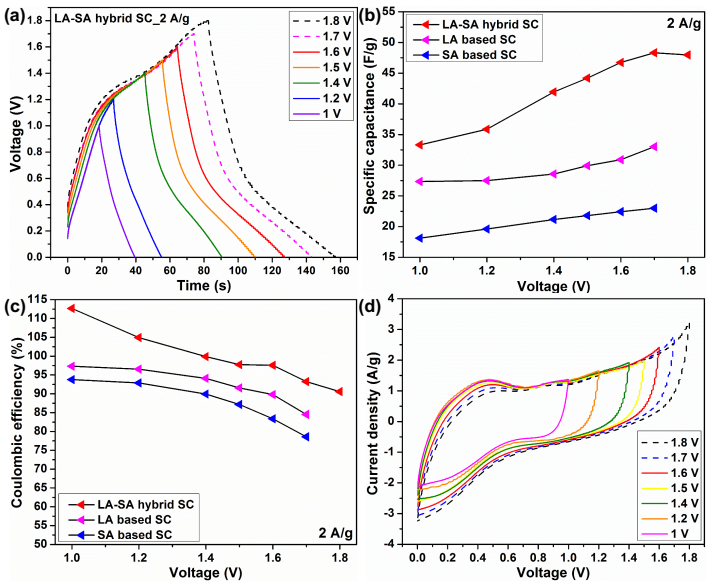

Figure 3.4. (a) GCD profiles of LA-SA hybrid SCs with various voltage windows at the current density of 2 A/g. (b) Discharge specific capacitance (considering the total mass of active material in the supercapacitors) and (c) coulombic efficiencies of LA-SA hybrid SC, LA and SA hybrid SCs calculated from GCD tests with various voltage windows at the current density of 2 A/g. (d) CV curves of LA-SA hybrid SC obtained at different voltage windows.

The GCD profiles of LA-SA hybrid SC at different voltage windows (from 1 to 1.8 V) are shown in figure 3.4a. It can be noticed that the charge and discharge profiles do not change

linearly which indicates the charge storage mechanism of LA-SA hybrid SC is not merely electric double layer but involves faradic redox reactions. Besides, as the increase of applied voltage, it is reasonable to see that the charge and discharge time are increased. The specific capacitances calculated from the discharge processes of different voltages and their corresponding coulombic efficiency are plotted in figure 3.4b and c, respectively. Evidently, the specific capacitances and coulombic efficiencies of LA-SA hybrid SC are overall larger than those of SA and LA hybrid SCs. In detail, with the increase of voltage window from 1 to 1.8 V, the specific capacitance of LA-SA hybrid SC increases from 33 to 48 F/g, while its coulombic efficiency drops from 112.6 % to 90.6 %. For SA hybrid SC, with the increase of voltage window from 1 to 1.7 V, its specific capacitance increases from 18 to 23 F/g and the corresponding coulombic efficiency drops from 93.8 % to 78.6 %. As the voltage window of LA hybrid SC is increased from 1 to 1.7V, the specific capacitance increases from 27 to 33 F/g, but the coulombic efficiency decreases from 97.3 % to 84.5 %.

The reason of LA-SA hybrid SC with the coulombic efficiency over 100% at 1 V is discussed below. As shown in figure S3.5, the GCD curve of LA-SA hybrid SC at 1V, the discharge time is a little bit longer than its charge time which makes the coulombic efficiency to be higher than 100%. This result can be explained by the analysis of the corresponding potential variation profiles (vs. Ag wire) of positive and negative electrodes shown in figure S3.5 (red and blue curves). For the charge process, the potential of the positive electrode stabilizes at around 1 V (vs. Ag wire) as a plateau, representing the oxidation reaction of Br^- to Br^{3-}, and the potential of negative electrode shows a linear drop, indicating the behavior of electric double layer capacitor (EDLC). For the discharge process, the potential of positive electrode also gives a plateau (the reduction reaction of Br^{3-} to Br^-). However, the potential change of negative

electrode not only shows the electric double layer behavior, but also exhibits a pseudo-capacitive behavior: the potential profile's slope changes at around 0.4 V vs. Ag wire. This change of slope corresponds to the nascent hydrogen (H) desorption peak around 0.4 V vs. Ag wire in figure 3.6c, indicating that H desorption occurs. The desorption process of nascent H on the negative electrode helps extend the discharge time.[37] As a result, the coulombic efficiency is over 100%.

The adsorbed H is produced through a pre-activation process, which is applied after the SC is fabricated to generate Br_3^- in the catholyte for improving the reversibility of Br^-/Br_3^- redox reaction. Briefly, during the GCD activation process, the supercapacitor is charged to 1.6 V and kept at this voltage for 1 hour. The potential of negative electrode reaches about -0.6 V (vs. Ag wire) and H can be produced (note the H adsorption peak at around -0.5V vs Ag wire in figure 3.6c). More detailed information of H electrosorption will be discussed later. As a result, the coulombic efficiency is over 100%.

In order to determine the most suitable voltage window of the LA-SA hybrid SC, CV curves obtained at different voltage windows are analyzed together with coulombic efficiency. It is necessary to mention that high coulombic efficiency is essential for a battery-type supercapacitor device with a high energy density. Therefore, using coulombic efficiency as one of the criteria to determine the operating voltage window of SC is reasonable and has been used in many publications.[22, 38, 39] As shown in figure 3.4d, comparing with the CV curves obtained from 1 to 1.5 V, there is a slightly increase of anodic current at 1.6 V, but rapid increase of anodic current at both 1.7 and 1.8 V which is caused by the electrolyte decomposition. Besides, it can be observed that, with the increase of voltage window, the coulombic efficiency of all three SCs decrease. For the trade-off between minimizing the negative effect of electrolyte decomposition, maximizing the operating voltage window, and ensuring the high coulombic

efficiency, 1.6 V was used as the operating voltage window to further investigate the electrochemical performance of the LA-SA hybrid SC. The detailed data of figure 3.4b and c can be found in table S3.2-3.4.

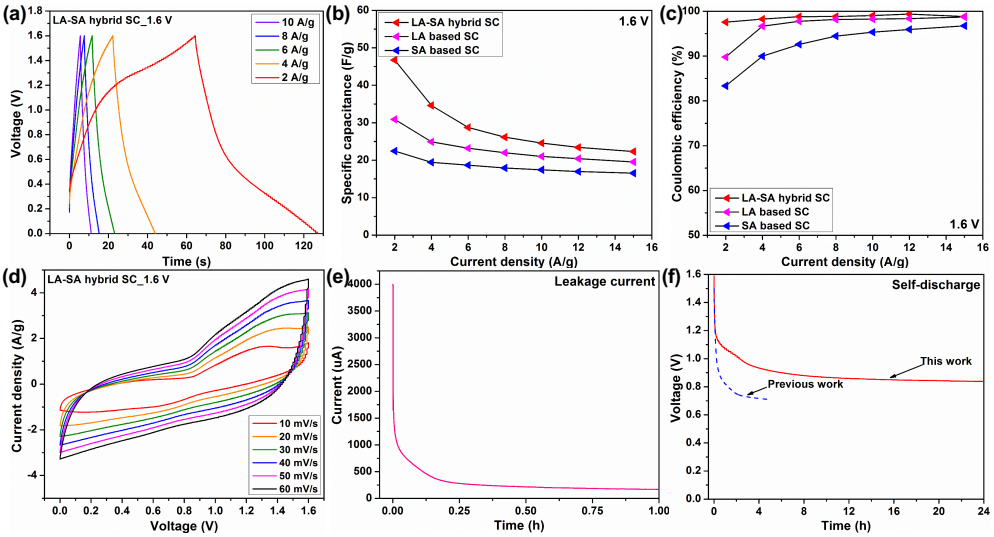

Figure 3.5. (a) GCD profiles of LA-SA hybrid SC at various current densities with a voltage window of 1.6 V. (b)Discharge specific capacitance and (c) coulombic efficiency of LA-SA hybrid SC, LA and SA hybrid SCs at various current densities at the voltage window of 1.6 V. (d) Two-electrode CV curves of LA-SA hybrid SC at different scan rates. (e) Leakage current and (f) self-discharge profile of LA-SA hybrid SC, compared with our previously reported redox-mediated aqueous supercapacitor.[19]

The GCD profiles of LA-SA hybrid SC at different current densities (2, 4, 6, 8, 10 A/g) are shown in figure 3.5a. It can be noticed that the GCD curves have obvious non-linear profiles, suggesting the faradic processes involved charge storage mechanism. From figure 3.5b, it can be observed that the specific capacitance of LA-SA hybrid SC is large than the other two types of SCs and the related explanation will be proposed in the later paragraph. With the increase of current density from 2 to 15 A/g, its specific capacitance decreases from 47 to 22 F/g, retained about 47 % of its initial value, which is not as good as the electric double layer capacitor without redox additive, but comparable with Li ion batteries.[40] Figure 3.5c gives the coulombic efficiencies of these three types of SCs at different current densities under the voltage window of

1.6 V. It can be recognized that, at all current densities, the coulombic efficiency of LA-SA hybrid SC is better than the other two cells. The detailed data can be found in table S3.5-3.7. Besides, the CV curves of LA-SA hybrid SC measured in a two electrode system is given in figure 3.5d and these curves do not have the rectangular shapes (which can represent the typical electric double layer behavior), but show some peaks indicating certain redox reactions have happened during the CV tests. In addition, the supercapacitor in the charged state always has a thermodynamic driving force to self-discharge due to the higher free energy compared to its discharged state.[41] For practical application purpose, leakage current and self-discharge are of great importance. As shown in figure 3.5e, the leakage current of LA-SA hybrid SC drops dramatically from 3.96 mA to 280.4 uA in the first 15 min and stabilized at 169.5 uA after 1 h. This small leakage current value indicates less self-discharging reactions caused by less shuttling of redox species between the anolyte and catholyte.[18] According to figure 3.5f, after 24 h's measurement, the voltage of LA-SA hybrid SC retained about 0.837 V from 1.6 V, which is around 52.3 % of its initial voltage. This result is better than our previously reported redox-mediated aqueous supercapacitor (which retained about 0.717 V from 1.5 V) due to the less shuttling of redox species in the solid-state electrolyte and the effective electrolytes separation contributed by Nafion 117 membrane.[19]

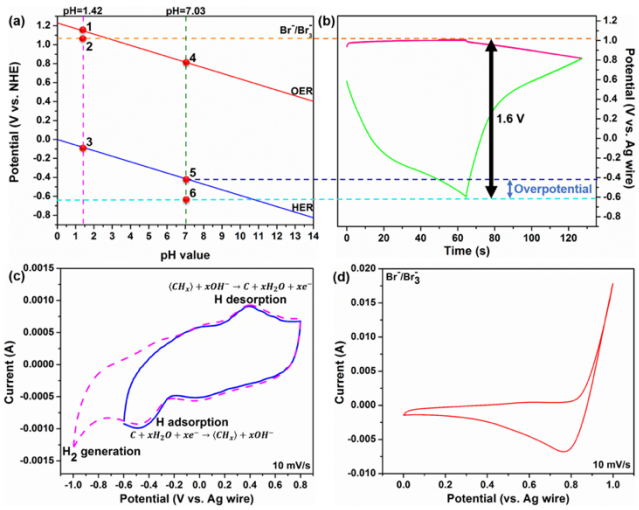

Figure 3.6. (a) Stability diagram of water and (b) potential variation profiles (vs. Ag wire) of positive and negative electrodes. (c) CV curves of negative electrode scanned at different potential range through a three electrode system and the scan rate is 10 mV/s. (d) CV curves of positive electrode through a three electrode system (10 mV/s).

Figure 3.6a gives the stability diagram of water calculated by the Nernst equation $E = E^0 - 0.059 \times pH$ (V), which reflect the changes of oxidization and reduction potentials for water versus the pH values at room temperature when no overpotentials exist.[42, 43, 44] In detail, as the pH increases from 0 to 14, the water oxidation potential (i.e. oxygen evolution reaction, OER represented by red full line) shifts from 1.229 to 0.403 V (vs. NHE) and, similarly, with the increase of pH value (from 0 to 14), the water reduction potential (i.e. hydrogen evolution reaction, HER represented by blue full line) decreases from 0 to -0.826 V. Besides, the potential of Br^-/Br_3^- redox reactions (equation 1) is also marked in figure 3.6a (represented by yellow dash line).[37, 38]

The potential variations of the positive and negative electrodes of LA-SA hybrid SC during GCD tests (at the current density of 2 A/g) are detected by using Ag wire as pseudo-reference electrode and shown in figure 3.6b. It can be observed that, during the charge process, the potential of positive electrode is stabilized at 1.009 V vs. Ag wire (point 2 in figure 3.6a),

which can be ascribed to the oxidation reaction of Br^- to Br_3^- (1.066 vs. NHE) in equation 1. In the discharge process, the potential of positive electrode drops slowly and exhibits an overall stable profile, indicating the reduction reaction of Br_3^- to Br^-. Therefore, during charge and discharge processes, the potential of positive electrode is pinned at the redox potential of Br^-/Br_3^-, which is within the OER limit (point 1 in figure 3.6a) meaning the overpotential of OER does not contribute to the extended voltage window and the voltage window is strongly determined by the HER overpotential of the negative electrode. For the potential of negative electrode, the non-linear potential variation profiles during both charge and discharge processes indicate that the charge storage mechanism of negative electrode is not only electric double layer but also involves some faradic processes, considering the plateaus observed at around -0.4 V (in charge process) and 0.4 V (in discharge process). As reported by work from Frackowial's group, during the charge process, the decomposition of water-based electrolyte on negative electrode made of carbon may result in the production of nascent hydrogen (H) before the hydrogen (H_2) evolution.[23, 47, 48 ,49] The corresponding chemical reaction equation is shown equation 7. Then, the produced nascent H is partially adsorbed and fixed on the surface of carbon material as shown in equation 8. After that, the desorption of nascent H following the inverse of equation 8 will occur in the discharge process. The overall nascent hydrogen electrosorption (including adsorption and desorption processes) can be summarized by equation 9.[48, 49]

$$H_2O + e^- \leftrightarrow H + OH^- \quad \textbf{(7)}$$

$$\langle C \rangle + xH \leftrightarrow \langle CH_X \rangle \quad \textbf{(8)}$$

$$C + xH_2O + xe^- \leftrightarrow \langle CH_X \rangle + xOH^- \quad \textbf{(9)}$$

Where $\langle C \rangle$ represents the carbon material and $\langle CH_X \rangle$ represents the hydrogen adsorbed carbon material. To verify if the aforementioned nascent H adsorption/desorption process could

happen at the negative electrode of the LA-SA hybrid SC, the CV curve was tested from the negative electrode, which is obtained by scanning a three-electrode cell between -0.6 V-0.8 V (blue full line in figure 3.6c), with the SC's negative electrode as the working electrode, an Ag wire as the pseudo-reference electrode, and the SC's positive electrode as the counter electrode in a LA-SA hybrid SC. It can be observed that the peak at around -0.4 V (vs. Ag wire) is the adsorption of nascent H and the peak at around 0.4 V (vs. Ag wire) can be ascribed to the desorption of nascent H, which agrees with Frackowial and coworkers' report. The electrosorption of nascent H can enhance the pseudo-capacitance of supercapacitors and extend the overpotential for HER.[37, 50 ,51] In addition, a CV curve, tested from the same three-electrode cell but with a potential range of -1 V-0.8 V vs. Ag wire, is also plotted in figure 3.6c (pink dash line in figure 3.6c). This curve is mostly overlapped with the previous CV curve, but the extra potential scan to -1 V (vs. Ag wire) induces a rapid increase of reduction current indicating that the generation of H_2 starts at around -0.7 to -0.8 V, lower than the operating potential limit of the negative electrode (-0.6 V vs. Ag wire, point 6 in figure 3.6a). In addition, no obvious potential plateau at -0.6 V vs Ag wire is observed from the GCD curve (figure 3.6b). These observations serve as strong evidence that HER does not happen at the negative electrode probably due to extended HER overpotential. This can further justify our previous discussion on the determination of operational voltage window to avoid excessive generation of H_2 at the negative electrode.

Moreover, to confirm the Br^-/Br_3^- redox activity at the cathode, another CV test is performed between 0 to 1V vs. Ag wire using the positive electrode as working electrode, an Ag wire as the pseudo-reference electrode and negative electrode as the counter electrode (figure 3.6d). In detail, an incomplete oxidation peak starting approximately from 0.79 to 1 V (vs. Ag

wire) is achieved during the forward scan and, during the backward scan, the reduction peak is located at around 0.76 V (vs. Ag wire), revealing the good reversibility of the reaction. In addition, this CV has the same shape as those reported for Br^-/Br_3^- reaction, which further demonstrates the occurrence of Br^-/Br_3^- redox reaction on the positive electrode.[19, 52]

The reasons for the lower specific capacitance of LA hybrid SC is discussed in the following. As shown in the electrode potential profiles (figure S3.7a), when operating at the voltage window of 1.6V, LA hybrid SC's positive electrode stays at the redox potential of Br^-/Br^{3-} with the catholyte's pH value of 1.42 (point 2 in figure 3.6a), similar to that of the LA-SA hybrid SC. However, its negative potential shows less significant plateau during both charge and discharge processes compared with that of LA-SA hybrid SC, indicating weakened H electrosoprtion on the carbon surface in the acidic condition of anolyte.[51] The weaker H electrosorption on the negative electrode of LA hybrid SC compared with that of LA-SA hybrid SC could explain why the former has lower pseudo-capacitance than the later. In addition, the lower potential limit of the negative electrode (-0.6 V vs Ag wire) is well below the thermodynamic HER potential for the LA electrolyte (point 3 in figure 3.6a). Hence, the potential plateau towards the end of charge is most likely due to the irreversible HER, which could also reduce the capacitance of the LA hybrid SC. The lower coulombic efficiency of LA hybrid SC (89.8 %) compared with LA-SA hybrid SC at 1.6 V voltage window (97.6 %) also indicates that more significant irreversible HER happen in LA hybrid SC.

Similarly, the SA hybrid SC also has lower discharge capacitance than LA-SA hybrid SC. But unlike the case of LA hybrid SC, the irreversible redox reaction at the positive electrode is the cause for its low capacitance. According to the potential variation profile of SA hybrid SC shown in figure S3.7b, it can be noticed that the upper potential limit of positive electrode is at

about 0.73 V (vs. Ag wire) instead of the potential of Br^-/Br^{3-} redox reaction (1.009 V vs. Ag wire or 1.066 V vs. NHE) or the thermodynamic OER potential in pH=7.03 (point 6 in figure 3.6a). Besides, it has been reported that under SA electrolyte's neutral pH condition, it is more likely for the Br^- to turn into BrO^- rather than Br^{3-} and the corresponding reaction equation is given by equation 10.[53] The redox potential for Br^-oxidized to BrO^- is 0.76 V (vs. NHE), which agrees with the potential measured through Ag wire pseudo-reference electrode (0.73 V vs. Ag wire in figure S3.7b). After BrO^- is generated it will be spontaneously converted to BrO_3^- and Br^- following a disproportionate reaction shown in equation 10.[54]

$$Br^- + 2OH^- \rightarrow BrO^- + H_2O + 2e^-, \text{ E}^0\text{=0.76 V vs. NHE} \quad \textbf{(10)}$$

$$3BrO^- \rightarrow BrO_3^- + 2Br^- \quad \textbf{(11)}$$

Due to the spontaneous reaction of (11), the reaction of (10) becomes highly irreversible, which is reflected by the fast decrease of positive electrode potential during discharge. Because of the irreversibility, the discharge capacitance of SA hybrid SC is greatly reduced compared to that of LA-SA hybrid SC, whose cathode reaction is dominated by the highly reversible Br^-/Br^{3-} redox reaction because the reaction of (10) was suppressed in its acidic catholyte.[53]

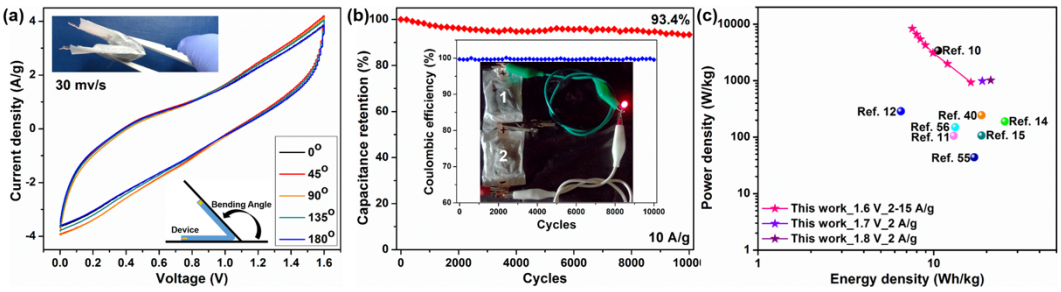

Figure 3.7. (a) CV curves of the LA-SA hybrid SC with bending angles of 0°, 45°, 90°, 135° and 180° at a scan rate of 30 mv/s. (b) Capacitance retention during a 10000 cycle test at the current density of 10 A/g, its coulombic efficiency (inset) during this 10000 cycles and the LED driven by two LA-SA hybrid SCs connected in series (inset). (c) Ragone plot of LA-SA hybrid SC.

In order to evaluate the potential of the LA-SA hybrid SC as flexible energy storage device, the CV performance of the LA-SA hybrid SC is tested under different bending angles (0^o, 45^o, 90^o, 135^o and 180^o) at a scan rate of 30 mv/s shown in figure 3.7a. It can be observed that the CV curves at different bending conditions are almost the same, indicating that the bending has nearly no effect on the capacitive performance. The cyclic stability of LA-SA hybrid SC is shown in figure 3.7b. It is noticed that about 93.4 % of the initial discharge capacitance can be retained after 10000 cycles at a high current density of 10 A/g, demonstrating its good cyclic stability at high current loading. The coulombic efficiency during the 10000 cycles (shown in the inset) is consistently close to 100%, further suggesting its good cyclic stability. However, when the lower current densities (such as 6 A/g and 2 A/g) are applied, the measured capacitances have more degradation (shown in figure S3.9). This may be caused by the diffusion of generated Br_3^- away from the FCNT surface which results in the irreversibility of Br^-/Br_3^- redox reactions. In order to solve the diffusion of soluble redox couples in redox-enhanced electrochemical capacitor, Seung Joon Yoo et al. recently proposed that if the reactant of reversible redox couples is water soluble but the product after charging process is in solid state, by immobilizing the solid product on the surface of porous electrode material, the cycle life of the capacitor can be dramatically increased.[21] Therefore, this strategy will be investigated in our future work to solve the capacitance decay problem.

As shown in figure S3.6, after cycling test, the color of the electrolyte near anode (or positive) electrode turned into yellowish color, which is characteristic of Br_3^-.[19, 45] Since BrO_3^- is colorless in solution, this visual inspection confirms that the irreversible reaction given in equation 9 and 10 did not occur at the cathode of the LA-SA hybrid SC, demonstrating the importance of having acidic conditions for catholyte with Br^-/Br^{3-} redox activity. The LED

powered by two LA-SA hybrid SCs connected in series is also displayed in the inset of figure 3.7b. The energy density and power density of the LA-SA hybrid SC are calculated and plotted in Ragone plot shown in figure 3.7c. The highest energy density of LA-SA hybrid SC is 16.3 Wh/kg obtained at 2A/g with the power density of 932.6 W/kg when the SC is charged to 1.6 V. Besides 1.6 V, the corresponding data of LA-SA hybrid SC measured at the voltage window of 1.7 and 1.8 V are also given in table S3.2. It can be noticed that, comparing with the data obtained from 1.6 V, the energy density and power density of LA-SA hybrid SC obtained from 1.7 V is 18.9 Wh/kg and 985.5 W/kg. The energy density and power density increase to 21.1 Wh/kg and 1017.3 W/kg when it operates at 1.8 V. The performance from other recently reported work using PVA hydrogel electrolyte are also included in figure 3.7c for comparison and detailed description is shown in table S3.8.[10, 11, 12, 14, 15, 40 ,57, 58] It is necessary to mention that the some of the reported results may be overestimated, since they used $C_{cell} = \frac{I \cdot \Delta t}{\Delta V \cdot m}$ (rather than equation 2) to calculate the specific capacitance while their GCD curves is clearly non-linear, where I is the discharge current, Δt is the discharge time, ΔV is the voltage drop during the discharge process (excluding IR drop) and m is the total mass of the active material from the two electrodes.[25]

3.5 Conclusion

Novel solid-state supercapacitor made of redox-active hydrogel electrolytes and functionalized carbon nanotube coated cellulose paper (FCP) electrodes has been developed in this work. Specifically, acidic PVA-[BMIM]Cl-Lactic acid-LiBr and neutral PVA-[BMIM]Cl-Sodium acetate-LiBr hydrogel polymer electrolytes are prepared through a combination of solution casting and freeze-thaw method, and later used as catholyte and anolyte, respectively. And the FCP electrodes were prepared by drop-casting FCNT solution onto cellulose papers. The

different pH values of the hydrogel electrolytes, as adjusted by the lactic acid and sodium acetate, bring three major benefits for enhancing the energy density of the hybrid supercapacitor: (1) it results in high cathode capacitance contributed from reversible Br^-/Br_3^- redox reaction on positive electrode; (2) it brings high voltage window mostly extended by negative electrode; and (3) it increase the anode capacitance by the electrosorption phenomenon of nascent H on negative electrode. As a result, the prepared solid-state hybrid supercapacitor shows a broad voltage window of 1.6 V at coulombic efficiency of 97.6 % and the highest energy density of 16.3 Wh/kg with power density of 932.6 W/kg at 2A/g. After 10000 cycles of GCD tests at 10A/g, it exhibits great cyclic stability with 93.4% retention of the initial capacity. In addition, robust capacitive performance can also be observed from the solid-state supercapacitor at different bending angles (0^o, 45^o, 90^o, 135^o and 180^o), indicating its great potential as a flexible energy storage device. Future work will be to investigate strategies to immobilize the redox pair inside the porous electrode to improve the cyclic stability of the hybrid SC and to eliminate the use of expensive separator membrane such as the Nafion 117.[21]

3.6 References

(1) Pech, D.; Brunet, M.; Durou, H.; Huang, P.; Mochalin, V.; Gogotsi, Y.; Taberna, P.-L.; Simon, P. Ultrahigh-Power Micrometre-Sized Supercapacitors Based on Onion-like Carbon. Nat. Nanotechnol. 2010, 5, 651–654.

(2) Yu, S.; Yang, N.; Zhuang, H.; Mandal, S.; Williams, O. A.; Yang, B.; Huang, N.; Jiang, X. Battery-like Supercapacitors from Diamond Networks and Water-Soluble Redox Electrolytes. J. Mater. Chem. A 2017, 5, 1778–1785.

(3) Pang, H.; Zhang, Y.-Z.; Run, Z.; Lai, W.-Y.; Huang, W. Amorphous Nickel Pyrophosphate Microstructures for High-Performance Flexible Solid-State Electrochemical Energy Storage Devices. Nano Energy 2015, 17, 339–347.

(4) Luo, W.; Gong, Y.; Zhu, Y.; Li, Y.; Yao, Y.; Zhang, Y.; Fu, K. K.; Pastel, G.; Lin, C.; Mo, Y. Reducing Interfacial Resistance between Garnet-Structured Solid-State Electrolyte and Li-Metal Anode by a Germanium Layer. Adv. Mater. 2017, 29, 1606042.

(5) Zhang, Y. Z.; Wang, Y.; Cheng, T.; Lai, W. Y.; Pang, H.; Huang, W. Flexible Supercapacitors Based on Paper Substrates: A New Paradigm for Low-Cost Energy Storage. Chem. Soc. Rev. 2015, 44, 5181–5199.

(6) Agrawal, R. C.; Pandey, G. P. Solid Polymer Electrolytes: Materials Designing and All-Solid-State Battery Applications: An Overview. J. Phys. D. Appl. Phys. 2008, 41, 223001.

(7) Arya, A.; Sharma, A. L. Polymer Electrolytes for Lithium Ion Batteries: A Critical Study. Ionics, 2017, 23, 497–540.

(8) Choudhury, N. A.; Sampath, S.; Shukla, A. K. Hydrogel-Polymer Electrolytes for Electrochemical Capacitors : An Overview. Energy Environ. Sci. 2009, 2, 55–67.

(9) Chodankar, N. R.; Dubal, D. P.; Lokhande, A. C.; Lokhande, C. D. Ionically Conducting PVA-LiClO4 Gel Electrolyte for High Performance Flexible Solid State Supercapacitors. J. Colloid Interface Sci. 2015, 460, 370–376.

(10) Zhang, X.; Wang, L.; Peng, J.; Cao, P.; Cai, X.; Li, J.; Zhai, M. A Flexible Ionic Liquid Gelled PVA-Li2SO4 Polymer Electrolyte for Semi-Solid-State Supercapacitors. Adv. Mater. Interfaces 2015, 2, 1500267.

(11) Batisse, N.; Raymundo-Piñero, E. A Self-Standing Hydrogel Neutral Electrolyte for High Voltage and Safe Flexible Supercapacitors. J. Power Sources 2017, 348, 168–174.

(12) Xu, Y.; Lin, Z.; Huang, X.; Liu, Y.; Huang, Y.; Duan, X. Flexible Solid-State Supercapacitors Based on Three-Dimensional Graphene Hydrogel Films. ACS Nano 2013, 7, 4042–4049.

(13) Sun, K.; Ran, F.; Zhao, G.; Zhu, Y.; Zheng, Y. High Energy Density of Quasi-Solid-State Supercapacitor Based on Redox-Mediated Gel Polymer Electrolyte. RSC Adv. 2016, 6, 55225–55232.

(14) Fan, L.; Zhong, J.; Wu, J.; Lin, J.; Huang, Y. Improving the Energy Density of Quasi-Solid-State Electric Double-Layer Capacitors by Introducing Redox Additives into Gel Polymer Electrolytes. J. Mater. Chem. A 2014, 2, 9011.

(15) Li, W.; Lu, H.; Zhang, N.; Ma, M. Enhancing the Properties of Conductive Polymer Hydrogels by Freeze-Thaw Cycles for High-Performance Flexible Supercapacitors. ACS Appl. Mater. Interfaces 2017, 9, 20142–20149.

(16) Pan, F.; Wang, Q. Redox Species of Redox Flow Batteries: A Review. Molecules, 2015, 20, 20499–20517.

(17) Soloveichik, G. L. Flow Batteries: Current Status and Trends. Chem. Rev. 2015, 115, 11533–11558.

(18) Chun, S.-E.; Evanko, B.; Wang, X.; Vonlanthen, D.; Ji, X.; Stucky, G. D.; Boettcher, S. W. Design of Aqueous Redox-Enhanced Electrochemical Capacitors with High Specific Energies and Slow Self-Discharge. Nat. Commun. 2015, 6, 7818.

(19) Tang, X.; Lui, Y. H.; Chen, B.; Hu, S. Functionalized Carbon Nanotube Based Hybrid Electrochemical Capacitors Using Neutral Bromide Redox-Active Electrolyte for Enhancing Energy Density. J. Power Sources 2017, 352, 118–126.

(20) Yamazaki, S.; Ito, T.; Murakumo, Y.; Naitou, M.; Shimooka, T.; Yamagata, M.; Ishikawa, M. Hybrid Capacitors Utilizing Halogen-Based Redox Reactions at Interface between Carbon Positive Electrode and Aqueous Electrolytes. J. Power Sources 2016, 326, 580–586.

(21) Yoo, S. J.; Evanko, B.; Wang, X.; Romelczyk, M.; Taylor, A.; Ji, X.; Boettcher, S. W.; Stucky, G. D. Fundamentally Addressing Bromine Storage through Reversible Solid-State Confinement in Porous Carbon Electrodes: Design of a High-Performance Dual-Redox Electrochemical Capacitor. J. Am. Chem. Soc. 2017, 139, 9985–9993.

(22) Khomenko, V.; Raymundo-Piñero, E.; Béguin, F. Optimisation of an Asymmetric Manganese Oxide/Activated Carbon Capacitor Working at 2V in Aqueous Medium. J. Power Sources 2006, 153, 183–190.

(23) Fic, K.; Meller, M.; Frackowiak, E. Interfacial Redox Phenomena for Enhanced Aqueous Supercapacitors. J. Electrochem. Soc. 2015, 162, A5140–A5147.

(24) Chen, B.; Jiang, Y.; Tang, X.; Pan, Y.; Hu, S. Fully-Packaged Carbon Nanotube Supercapacitors by Direct Ink Writing on Flexible Substrates. ACS Appl. Mater. Interfaces 2017, 9, 28433–28440.

(25) Roldán, S.; Barreda, D.; Granda, M.; Menéndez, R.; Santamaría, R.; Blanco, C. An Approach to Classification and Capacitance Expressions in Electrochemical Capacitors Technology. Phys. Chem. Chem. Phys. 2015, 17, 1084–1092.

(26) Laheäär, A.; Przygocki, P.; Abbas, Q.; Béguin, F. Appropriate Methods for Evaluating the Efficiency and Capacitive Behavior of Different Types of Supercapacitors. Electrochem. commun. 2015, 60, 21–25.

(27) Sheng, L.; Jiang, L.; Wei, T.; Liu, Z.; Fan, Z. Spatial Charge Storage within Honeycomb-Carbon Frameworks for Ultrafast Supercapacitors with High Energy and Power Densities. Adv. Energy Mater. 2017, 7, 1700668.

(28) Feng, E.; Ma, G.; Sun, K.; Yang, Q.; Lei, Z. RSC Advances Electrolyte and Separator Applying Supercapacitors. RSC Adv. 2016, 6, 75896–75904.

(29) Zhou, D.; He, Y.; Liu, R.; Liu, M.; Du, H.; Li, B.; Cai, Q. In Situ Synthesis of a Hierarchical All-Solid-State Electrolyte Based on Nitrile Materials for High-Performance Lithium- Ion Batteries. Adv. Energy Mater. 2015, 5, 1500353.

(30) Yu, H.; Wu, J.; Fan, L.; Lin, Y.; Xu, K.; Tang, Z.; Cheng, C.; Tang, S.; Lin, J.; Huang, M.; et al. A Novel Redox-Mediated Gel Polymer Electrolyte for High-Performance Supercapacitor. J. Power Sources 2012, 198, 402–407.

(31) Jannasch, P. Ion Conducting Electrolytes Based on Aggregating Comblike Poly(Propylene Oxide). Polymer (Guildf). 2001, 42, 8629–8635.

(32) Wang, T.; Gunasekaran, S. State of Water in Chitosan–PVA Hydrogel. J. Appl. Polym. Sci. 2006, 101, 3227–3232.

(33) Nakaoki, T.; Yamashita, H. Bound States of Water in Poly(Vinyl Alcohol) Hydrogel Prepared by Repeated Freezing and Melting Method. J. Mol. Struct. 2008, 875, 282–287.

(34) Wang, Y. Effect of Water State and Polymer Chain Motion on the Mechanical Properties of a Bacterial Cellulose and Polyvinyl Alcohol (BC/PVA) Hydrogel. RSC Adv. 2015, 5, 25525–25531.

(35) Li, L.; Wang, Y.; Sun, H.; Duan, L.; Wang, X.; Si, J. Single-Walled Carbon Nanotube Solution-Based Saturable Absorbers for Mode-Locked Fiber Laser. Opt. Eng. 2015, 54, 086103.

(36) Eklund, P. C.; M., H. J.; A., J. R. Vibrational Modes of Carbon Nanotubes; Spectroscopy and Theory. Carbon N. Y. 1995, 33, 959–972.

(37) Fic, K.; Meller, M.; Frackowiak, E. Strategies for Enhancing the Performance of Carbon / Carbon Supercapacitors in Aqueous Electrolytes. Electrochim. Acta 2014, 128, 210–217.

(38) Wang, X.; Chandrabose, R. S.; Jian, Z.; Xing, Z.; Ji, X. A 1.8 V Aqueous Supercapacitor with a Bipolar Assembly of Ion-Exchange Membranes as the Separator. J. Electrochem. Soc. 2016, 163, A1853–A1858.

(39) Stoller, M. D.; Ruoff, R. S. Best Practice Methods for Determining an Electrode Material's Performance for Ultracapacitors. Energy Environ. Sci. 2010, 3, 1294.

(40) Zhong, J.; Fan, L.-Q.; Wu, X.; Wu, J.-H.; Liu, G.-J.; Lin, J.-M.; Huang, M.-L.; Wei, Y.-L. Improved Energy Density of Quasi-Solid-State Supercapacitors Using Sandwich-Type Redox-Active Gel Polymer Electrolytes. Electrochim. Acta 2015, 166, 150–156.

(41) El-Kady, M. F.; Kaner, R. B. Scalable Fabrication of High-Power Graphene Micro-Supercapacitors for Flexible and on-Chip Energy Storage. Nat. Commun. 2013, 4, 1475.

(42) Tsuchida, N.; Muir, D. M. Potentiometric Studies on the Adsorption of Au(CN)2 and Ag(CN)2 onto Activated Carbon. Metall. Trans. B 1986, 17, 523–528.

(43) Li, L.; Fu, Y.; Manthiram, A. Imidazole-Buffered Acidic Catholytes for Hybrid Li–Air Batteries with High Practical Energy Density. Electrochem. commun. 2014, 47, 67–70.

(44) Walter, M. G.; Warren, E. L.; McKone, J. R.; Boettcher, S. W.; Mi, Q.; Santori, E. A.; Lewis, N. S. Solar Water Splitting Cells. Chem. Rev. 2010, 110, 6446–6473.

(45) Wang, Z. S.; Sayama, K.; Sugihara, H. Efficient Eosin Y Dye-Sensitized Solar Cell Containing Br-/Br3-Electrolyte. J. Phys. Chem. B 2005, 109, 22449–22455.

(46) Bard, A. J.; Faulkner, L. R. Electrochemical Methods: Fundamentals and Applications; Wiley New York, 1980; Vol. 2.

(47) Fic, K.; Lota, G.; Meller, M.; Frackowiak, E. Novel Insight into Neutral Medium as Electrolyte for High-Voltage Supercapacitors. Energy Environ. Sci. 2012, 5, 5842–5850.

(48) Béguin, F.; Presser, V.; Balducci, A.; Frackowiak, E. Carbons and Electrolytes for Advanced Supercapacitors. Adv. Mater. 2014, 26, 2219–2251.

(49) Abbas, Q.; Ratajczak, P.; Béguin, F. Sodium Molybdate - an Additive of Choice for Enhancing the Performance of AC/AC Electrochemical Capacitors in a Salt Aqueous Electrolyte. Faraday Discuss. 2014, 172, 199–214.

(50) Batisse, N.; Raymundo-Piñero, E. A Self-Standing Hydrogel Neutral Electrolyte for High Voltage and Safe Flexible Supercapacitors. J. Power Sources 2017, 348, 168–174.

(51) Fic, K.; Meller, M.; Frackowiak, E. Interfacial Redox Phenomena for Enhanced Aqueous Supercapacitors. J. Electrochem. Soc. 2015, 162, A5140–A5147.

(52) Chang, Z.; Wang, X.; Yang, Y.; Gao, J.; Li, M.; Liu, L.; Wu, Y. Rechargeable Li//Br Battery: A Promising Platform for Post Lithium Ion Batteries. J. Mater. Chem. A 2014, 2, 19444–19450.

(53) Zhao, Y.; Ding, Y.; Song, J.; Peng, L.; Goodenough, J. B.; Yu, G. A Reversible Br2/Br− Redox Couple in the Aqueous Phase as a High-Performance Catholyte for Alkali-Ion Batteries. Energy Environ. Sci. 2014, 7, 1990–1995.

(54) Janssen, F.; Kanij, J. Bromine Tracer Study of the Chlorination with Hypochlorite in a Buffered and a Non-Buffered Aqueous Solution Containing Chloride, Bromide and Phenol as Model Compound. Water Res. 1981, 15, 463–468.

(55) Wang, K.; Xu, M.; Gu, Y.; Gu, Z.; Hua, Q. Symmetric Supercapacitors Using Urea-Modified Lignin Derived N-Doped Porous Carbon as Electrode Materials in Liquid and Solid Electrolytes. J. Power Sources 2016, 332, 180–186.

(56) Ma, G.; Dong, M.; Sun, K.; Feng, E.; Lei, Z. A Redox Mediator Doped Gel Polymer as an Electrolyte and Separator for a High Performance Solid State Supercapacitor. J. Mater. Chem. A 2015, 3, 4035–4041.

(57) Jiang, M.; Zhu, J.; Chen, C.; Lu, Y.; Pampal, E. S.; Luo, L.; Zhu, P.; Zhang, X. Superior High-Voltage Aqueous Carbon/Carbon Supercapacitors Operating with in Situ Electrodeposited Polyvinyl Alcohol Borate Gel Polymer Electrolytes. J. Mater. Chem. A 2016, 4, 16588–16596.

(58) Wang, K.; Xu, M.; Gu, Y.; Gu, Z.; Hua, Q. Symmetric Supercapacitors Using Urea-Modi Fi Ed Lignin Derived N-Doped Porous Carbon as Electrode Materials in Liquid and Solid Electrolytes. J. Power Sources 2016, 332, 180–186.

(59) Roldán, S.; Barreda, D.; Granda, M.; Menéndez, R.; Santamaría, R.; Blanco, C. An Approach to Classification and Capacitance Expressions in Electrochemical Capacitors Technology. Phys. Chem. Chem. Phys. 2015, 17, 1084–1092.

CHAPTER 4. NI-MN BIMETALLIC OXIDE NANOSHEETS AS HIGH-PERFORMANCE ELECTRODE MATERIALS FOR ASYMMETRIC SUPERCAPACITORS

Xiaohui Tang, Bowei Zhang, Yui Hui Lui and Shan Hu*

Department of Mechanical Engineering, Iowa State University, Ames, Iowa, 50010, USA
*Corresponding author Email: shanhu@iastate.edu

Modified from a manuscript published in "J. of Energy Storage 25 (2019): 100897."

Note: The supporting information is shown in APPENDIX C.

4.1 Abstract

Using bimetallic oxide as the electrode material of supercapacitor is emerging as a promising approach to supply better pseudocapacitive performance than that from the electrodes made of corresponding single metal oxides. Herein, Ni-Mn bimetallic oxide nanosheets (Ni-MnBMO) on carbon cloth substrate were synthesized through a facile hydrothermal method. With the help of cyclic voltammetry activation process, the prepared A-Ni-MnBMO electrode exhibits the maximum specific capacitance 574 F g^{-1} (within a potential range of -0.2-1.2 V vs. Ag/AgCl at 1 A g^{-1} after excluding the effects of OER) mainly due to the reversible redox reactions of Mn^{3+}/Mn^{4+}. Moreover, to prove its potential as the positive electrode in a supercapacitor, an asymmetric supercapacitor with a voltage range of 2.1 V is fabricated by using functional carbon nanotube as the negative electrode and 1M Na_2SO_4 as the electrolyte. As a result, the device can deliver a maximum energy density of 27 Wh kg^{-1} (at 0.5 A g^{-1}) and 82.3 % of its initial specific capacitance can be maintained after 8000 cycles of galvanostatic charge and discharge tests at 4 A g^{-1}.

4.2 Introduction

With the rapid development of renewable electricity generation technologies and modern electronic equipment, novel energy storage devices are becoming more important than at any

time in the past.[1, 2, 3] Among the existing energy storage technologies, supercapacitors have attracted worldwide attention of the researchers due to its long cycle life, fast charge/discharge rate and high power density.[4, 5, 6] However, because of their intrinsically low energy density compared with batteries, the applications of traditional supercapacitors in practical situations are still hindered, motivating researchers to keep investigating new supercapacitors with improved performance. Recently, asymmetric supercapacitors (ASCs) consisting of one pseudocapacitve electrode and one electric double-layer capacitive (EDLC) electrode in aqueous electrolyte is emerging quickly. The energy density of ASCs can be dramatically boosted by the fast reversible redox reactions on the surface of pseudocapacitive electrodes (such as metal oxides and conductive polymers), while the relatively high power density can still be maintained owing to the characteristics of the EDLC electrode (which stores charges through the surface adsorption/desorption of ions).[7, 8, 9] Furthermore, this asymmetric design can help extend the operating voltage window of supercapacitors beyond the thermodynamic limit of aqueous electrolyte (1.23 V) to about 2 V. [8, 10] Therefore, ASCs can be considered as one of the most suitable energy storage devices that has the capability of bridging the energy/power performance gap between batteries and conventional capacitors.

Many materials have been investigated as electrode materials for ASCs. It is well known that EDLC electrode is typically made of high-surface-area carbon materials (e.g. carbon nanotube, graphene and activated carbon) and their corresponding performances have been thoroughly researched.[11, 12] On the other hand, transition metal oxides, hydroxides, sulfides, phosphides with redox activities within the electrochemical window of aqueous electrolytes have been investigated as possible pseudocapacitive electrode materials for ASCs.[5, 13, 14] Among these, manganese dioxide (MnO_2) has attracted the attention of many researchers because of its low

cost (compared with RuO_2), low toxicity, abundance in the Earth's crust, high work function and large theoretical specific capacitance (about 1370 F g^{-1}), etc.[15, 16] After Lee and Goodenough firstly used amorphous $MnO_2 \cdot nH_2O$ as the supercapacitor electrode in 2 M KCl electrolyte and showed the specific capacitance of 200 F g^{-1} (at 5 mV s^{-1}), many more have investigated MnO_2 with novel morphologies and structures in order to achieve electrodes with larger specific capacitances and devices with higher energy densities.[17, 18] For example, Vinny et al. synthesized bristle-like α-MnO_2 nanoparticles on multiwall carbon nanotube which exhibited a specific capacitance of 255 F g^{-1} (at 2 mV s^{-1}) in 1M Na_2SO_4.[19] Lee et al. successfully embedded mesoporous MnO_2 into carbon nanotube network (MnO_2@CNT) and the obtained electrode material showed a specific capacitance of 337 F g^{-1} (1 mV s^{-1}) in 1 M Na_2SO_4.[6] Obviously, these experimental results are still much lower than the theoretical specific capacitance. Thus, it is still necessary for researchers to exploring new types of MnO_2 based pseudocapacitive electrode materials.

Recently, it has been reported that mixed metal oxides (MMOs), typically bimetallic oxides (BMO) containing at least one transition metal element, can exhibit improved pseudocapacitive performance with more active sites, higher stability and better electrical conductivity than their corresponding single metal oxides due to the synergetic effects between the two metal elements.[20, 21, 22, 23, 24, 25, 26] Therefore, it is expected that by incorporating other metal elements (such as Ni) into MnO_2, the prepared BMO electrode may exhibit better pseudocapacitive performance than that of MnO_2 electrode. In addition, Jabeen et al. proposed that the pseudocapacitance of MnO_2 can be enhanced by incorporating Na ion into MnO_2 to partially reduce Mn^{4+} in MnO_2 to Mn^{3+} in order to induce the Mn^{3+}/Mn^{4+} redox reactions.[27, 28] For the same purpose, we planned to incorporate Ni element into MnO_2. Considering that Ni^{2+}

has higher valence state than Na^+, it is expected to produce more Mn^{3+} and induce more pseudocapacitance from Mn^{3+}/Mn^{4+} redox reactions.

Herein, a facile one-step hydrothermal method is reported to synthesize Ni-Mn bimetallic oxide (Ni-MnBMO) nanosheets on the surface of carbon cloth substrate. The synthesized Ni-MnBMO nanosheets were then electrochemically activated by cyclic voltammetry (CV) and used as the electrode of a supercapacitor in the neutral 1M Na_2SO_4 electrolyte. The activated Ni-MnBMO electrode (A-Ni-MnBMO) achieves the maximum specific capacitance value of 510 F g^{-1} (at 5 mV s^{-1}) from CV test, which is much larger than the result from the MnO_2 electrode. It is found that the pseudocapactive performance of A-Ni-MnBMO electrode is contributed by the redox reactions of Mn^{3+}/Mn^{4+} along with Na^+ insertion/desertion process. The reversibility and activity of this key redox reaction in A-Ni-MnBMO are improved by the combination of introduced Ni element (which can change the electronic structure of MnO_2) and Na^+ insertion/desertion (which can create more active sites on electrode material during the activation process). In order to demonstrate A-Ni-MnBMO electrode as a potential positive electrode material for energy storage applications, an ASC with a voltage window of 2.1 V named as A-Ni-MnBMO//FCNT supercapacitor is fabricated by incorporating A-Ni-MnBMO electrode as positive electrode and functional carbon nanotube (FCNT) as negative electrode in 1M Na_2SO_4 electrolyte. The device exhibits a maximum energy density of 27 Wh kg^{-1} (at 0.5 A g^{-1}) with a power density of 486.6 W kg^{-1} and 82.3 % of its initial specific capacitance can be retained after 8000 cycles of GCD tests at a current density of 4 A g^{-1}.

4.3 Methods

4.3.1 Materials

Carbon cloth (ELAT® hydrophilic plain-cloth, FuelCellsEtc), potassium permanganate ($KMnO_4$, Fisher Chemical, formula weight: 158.03 g mol^{-1}), iron (III) sulfate pentahydrate ($Fe_2(SO_4)_3•5H_2O$, ACROS Organics, formula weight: 489.96 g mol^{-1}), nickel nitrate hexahydrate ($Ni(NO_3)_2•6H_2O$, Fisher Chemical, formula weight: 290.82 g mol^{-1}), sulfuric acid (H_2SO_4, Fisher Chemical, formula weight: 98.08 g mol^{-1}, 95-98 % reagent grade), nitric acid (HNO_3 , Fisher Chemical, formula weight: 63.012 g mol^{-1}, 68-70 % reagent grade) ,sodium sulfate (Na_2SO_4, Fisher Chemical, formula weight: 142.04 g mol^{-1}), deionized water, carbon nanotube (CNT, product name: TNSAR, Timesnano, single wall, purity: > 95 %, specific surface area: > 1075 m^2 g^{-1}) and kapton polyimide film (McMaster-Carr, USA). All chemical reagents are in analytical grade and used as received.

4.3.2 Synthesis of A-Ni-MnBMO electrode

A-Ni-MnBMO electrode was synthesized on carbon cloth by a facile hydrothermal process. Typically, 0.69 g $Ni(NO_3)_2•6H_2O$ and 0.125 g $KMnO_4$ (which implies the molar ratio between Ni and Mn elements is 1.5 : 0.5 in the precursor) were dissolved in 80 mL of deionized water and, then, 0.048 g $Fe_2(SO_4)_3•5H_2O$ and 18 µL H_2SO_4 were also added into the solution with magnetic stirring at room temperature for 20 min. The resulting solution was transferred into a 100 mL autoclave in which a piece of carbon cloth with the dimension of 4x4 cm^2 was vertically placed. After that, the autoclave was heated to 150 ^oC in a box oven and maintained at this temperature for 6 h. Then, the sample was taken out of the autoclave at room temperature and washed by deionized water and ethanol for several times to remove the loosely attached products. Finally, the obtained sample was dried in a vacuum oven at 60 ^oC for 3 h. The mass

loading of Ni-Mn bimetallic oxide electrode (Ni-MnBMO) is about 0.5 mg/cm^2. Then, the sample was activated via cyclic voltammetry (CV) scans between -0.2 and 1.3 V (vs. Ag/AgCl) 1 M Na_2SO_4 electrolyte for 1000 cycles to obtain A-Ni-MnBMO electrode. At the 500th cycle, the cycling was stopped to replace the used electrolyte with freshly prepared one and the cycling was resumed to complete the rest 500 cycles. Moreover, the electrode samples made of precursors with different molar ratios between Ni and Mn elements (such as Ni:Mn=0:2, Ni:Mn=0.5:1.5, Ni:Mn=1:1 and Ni:Mn=2:0) were also synthesized and the morphology of these samples are investigated by SEM shown in figure S4.1. Besides, the hydrophilic FCNT dispersed in water is prepared through a modified acid treatment method.[29, 30] Briefly, 100 mg raw single wall CNTs were added into 40 mL of acid mixture of sulfuric acid (98 wt %) and nitric acid (69 wt %) with a volume ratio of 3:1 and stirred for 10 min at the temperature of 110 °C. The mixture was then diluted to 200 mL drop by drop. The obtained FCNT were collected by membrane filtration and washed by deionized water to remove residual acids. Finally, the FCNT were uniformly dispersed into 50 mL of DI water through a 30 min probe sonication. Then, the prepared FCNT was drop casted on the surface of kapton polyimide film to make FCNT electrode. The mass loading of a typical FCNT electrode (2x2 cm^2) is about 1 mg.

4.3.3 Preparation of A-Ni-MnBMO//FCNT supercapacitor

In order to demonstrate that A-Ni-MnBMO electrode can be used as a potential positive electrode material for energy storage applications, an ASC named as A-Ni-MnBMO//FCNT supercapacitor is fabricated by utilizing A-Ni-MnBMO electrode as positive electrode, FCNT electrode as negative electrode and 1 M Na_2SO_4 as electrolyte. The schematic illustration is shown in figure S4.5a.

4.3.4 Calculation equations

The specific capacitance of different electrodes and devices can be calculated from CV curves and GCD curves according to equation (1) and (4), respectively.

$$C_{sp} = [\int_{V_1}^{V_2} IdV \,/2vm(V_2 - V_1)] \times 10^6 \qquad (1)$$

where C_{sp} (F g^{-1}) is specific capacitance, $V_2 - V_1$ (V) are potential range of CV, I (A) is current, V (V) is potential, v (mV s^{-1}) is scan rate of CV curve and m (mg) is the mass loading of active materials in electrodes. For a cell level calculation, the value of m is 1.5 mg which the sum of active material on both electrodes. (In detail, it is the sum of 0.5 mg from A-Ni-MnBMO electrode and 1 mg from FCNT electrode.)

Since the measured discharge curves of electrodes and devices are not strictly linear, in order not to overestimate the energy density, the energy density of electrodes and devices are calculated by equation (2). The corresponding power density and coulombic efficiency can be calculated by equation (3) and (5), respectively.

$$E = I \int V \, dt \times 1000/3600 \qquad (2)$$

Where E (Wh kg^{-1}) is energy density, I (A g^{-1}) is current density, V (V) is the potential or voltage from GCD curve and t (s) is time.

$$P = E/t_{discharge} \qquad (3)$$

Where P (W kg^{-1}) is power density, E (Wh kg^{-1}) is energy density and $t_{discharge}$ (h) is the discharge time.

$$C_{SP} = 2E/(V_{max}^2 \times 3.6) \qquad (4)$$

Where C_{sp} (F g^{-1}) is specific capacitance, E (Wh kg^{-1}) is energy density and V_{max} (V) is the discharge potential or voltage excluding IR drop.

$$\eta = t_{discharge}/t_{charge} \times 100\,\% \qquad (5)$$

Where $t_{discharge}$ (s) is the discharge time of GCD curve and t_{charge} (s) is the charge time of GCD curve.

4.3.5 Instrumental characterization

Scanning electron microscopy (SEM) images, energy dispersive spectroscopy (EDS) and the corresponding elemental mapping were recorded on a FEI Quanta 250 FEG scanning electron microscope (FEI). X-ray photoelectron spectroscopies (XPS) were tested in a Kratos Amicus X-ray Photoelectron Spectrometer (Kratos, Japan). X-ray diffraction (XRD) spectrums were measured from a Rigaku XRD SmartLab. CV, electrochemical impedance spectroscopy (EIS), and galvanostatic charge and discharge (GCD) curves were obtained on a potentiostat/galvanostat system (Gamry Reference 3000 Electrochemical Station, Gamry). The reference electrode used in electrochemical tests is Ag/AgCl (immersed in 1 M KCl).

4.4 Results and discussion

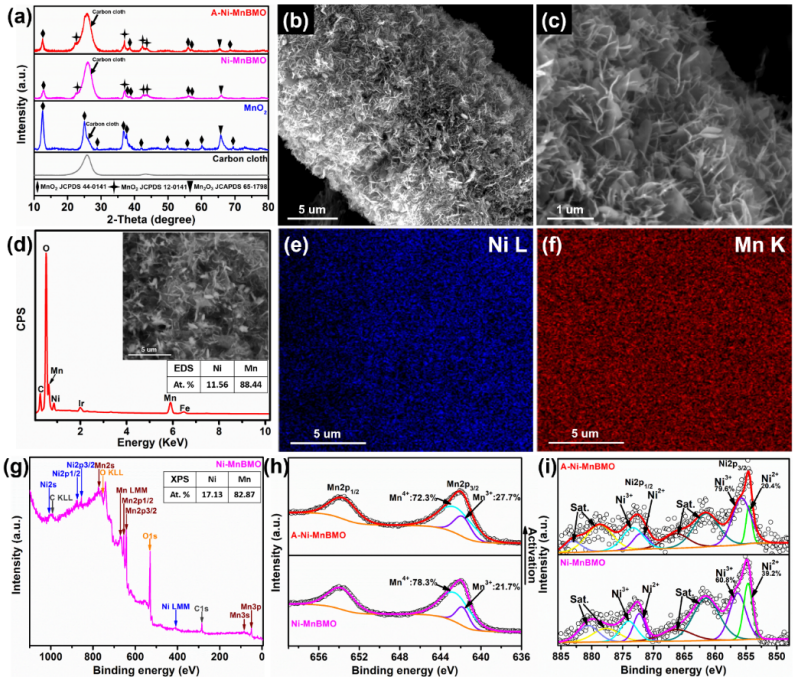

Figure 4.1. (a) XRD spectrums of different sample electrodes. SEM images of Ni-MnBMO electrode with different magnifications: (b) 5000x, scale bar: 5 um and (c) 23000x, scale bar: 1 um. (d) EDS spectrum of Ni-MnBMO electrode. The inset is the selected SEM area for EDS and

elemental mapping. The corresponding elemental mapping results for (e) Ni and (f) Mn elements. (g) Survey XPS spectrum of Ni-MnBMO electrode. (h) Mn2p core-level XPS spectrum of Ni-MnBMO and A-Ni-MnBMO electrodes. (i) Ni2p core-level XPS spectrum of Ni-MnBMO and A-Ni-MnBMO electrodes.

In order to detect structural differences in electrode materials synthesized from precursors with and without Ni ions added, XRD is provided in figure 4.1a for detailed analysis. When Ni ions are not added into the precursor, the XRD spectrum of the product (in blue color) confirms the generation of MnO_2 (according to the JCPDS #44-0141) and the valence state of most Mn element should be 4+. However, one diffraction peak (around 66 degrees) which can be ascribed to Mn_2O_3 (JCPDS #65-1798) is found, suggesting that not all the precursors have been completely transferred to MnO_2 after hydrothermal process. The XRD spectrum in magenta color gives the result of Ni-MnBMO. Most of the peaks can be indexed to MnO_2 (JCPDS #44-0141) and one peak around 66 degrees can also be indexed to Mn_2O_3 (JCPDS #65-1798), but its intensity becomes much smaller. Interestingly, it can be found that, after Ni ions are added into the precursor, several peaks that can be ascribed to other type of MnO_2 (JCPDS #12-0141) occurs on XRD spectrum. This phase change caused by the addition of Ni element can be used as the proof for the formation of Ni-MnBMO with partial substitution of Mn by Ni.[31] The XRD spectrum of A-Ni-MnBMO electrode only shows a minor difference (which is probably caused by Na^+ insertion/extraction) from that of Ni-MnBMO electrode, revealing the good stability of the material. As shown in figure 4.1b and c, the morphology of Ni-MnBMO electrode is investigated by SEM with different magnifications. It can be observed that Ni-MnBMO nanosheets with the approximate thickness of 20-30 nm (The thickness of nanosheets are measured in figure S4.2) are uniformly grown on the surface of carbon fiber and the space among nanosheets can create abundant pathways for transporting active ions from electrolyte to the surface of electrode material. In figure 4.1d, the EDS spectrum of Ni-MnBMO electrode

(The inset is the selected SEM area for EDS and elemental mapping.) indicates that the atomic ratio between Ni and Mn elements is about 11.56 % to 88.44 %, and the corresponding elemental mapping images shown in figure 4.1e and f unambiguously demonstrates the homogeneous distribution of Ni and Mn elements, suggesting the successfully formation of Ni-MnBMO. The surface chemical composition and the chemical states of Ni and Mn elements in Ni-MnBMO and A-Ni-MnBMO electrodes are analyzed by XPS. In figure 4.1g, the survey XPS spectrum confirms the existence of Ni, Mn, C and O elements which are the signals from the produced Ni-MnBMO and carbon cloth substrate. Moreover, the atomic ratio between Ni and Mn investigated by this survey XPS spectrum is 17.13 % to 82.87 %, which is close to the result measured from EDS. The survey XPS spectrum of A-Ni-MnBMO electrode (displayed in figure S4.3a) can not only show the signal of Ni, Mn, O and C, but also the signal of Na which can be ascribed to the hydrated Na^+ ions in the inter-layer of MnO_2.[32] The chemical states of Mn element in Ni-MnBMO and A-Ni-MnBMO electrodes are investigated by the high-resolution Mn2p core-level XPS spectrum (shown in figure 4.1h). From Ni-MnBMO to A-Ni-MnBMO, the content of Mn^{4+} is decreased from 78.3% to 72.3%, indicating the partial reduction of Mn element from Mn^{4+} to Mn^{3+}. This conclusion can be confirmed by Mn3s core-level XPS spectrum (shown in figure S4.3b), where the peak separation value indicates the mean Mn oxidation state and the increase of peak separation suggests the reduction of Mn element. The partial reduction of Mn element is reported to be caused by the effect of pre-insertion of cation ions during Na+ insertion/desertion process.[27, 28] The high-resolution Ni2p core-level XPS spectrum of Ni-MnBMO electrode (magenta curve shown in figure 4.1i) can be fitted into two spin-orbit doublets and two shake-up satellites (marked as Sat.), indicating the presence of Ni^{2+} and Ni^{3+}. The peaks appeared at 854.6 eV and 856.3 eV correspond to the Ni^{2+} located at octahedral sites and Ni^{3+} located at tetrahedral

sites, respectively.[33] The existence of Ni element may come from the partial substitution of Mn atoms by Ni atoms during hydrothermal process and the electrochemical behavior of Ni element can be affected by the chemical state change of Mn. One evidence to prove this assumption is that, after activation process, Mn element has been partially reduced (as discussed above in figure 4.1h) and, in the meanwhile, the content of Ni^{3+} increases (like the calculation result of Ni2p3/2 shown in figure 4.1i) from 60.8% to 79.6%, suggesting the partial oxidation of Ni element. This kind of simultaneous valence change implies the variation of the electronic structure of MnO_2, but more information about Ni element in this material still needs to be investigated in the future.

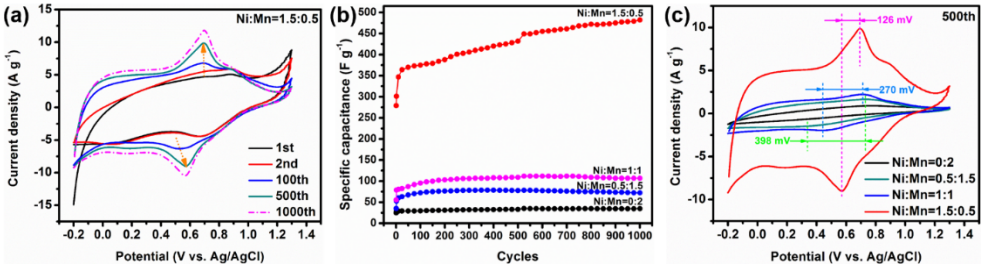

Figure 4.2. (a) CV electrochemical activation processes (10 mV s^{-1}) of electrodes produced from precursors with Ni/Mn molar ratio of 1.5 to 0.5. (b) The corresponding change of specific capacitance during the CV activation processes (hollow circle) and the extra CV tests (solid circle) conducted after the activation processes. (c) The comparison of CV curves (10 mV s^{-1}) of electrodes with different Ni/Mn molar ratios in precursor at 500th activation cycle.

The electrochemical performances of as-prepared sample electrodes were investigated in a three-electrode system with 1M Na_2SO_4 as electrolyte, Ag/AgCl (in 1M KCl) as reference electrode and Pt wire as counter electrode. The prepared electrodes were activated electrochemically through the 1000-cycle CV within a wide potential window of -0.2-1.3 V (vs. Ag/AgCl) at the scan rate of 10 mV s^{-1}. The main purpose of this activation process is to increase the active sites within the electrode materials through insertion/extraction of ions during CV circulations and, thus, the electrode material with higher performance can be obtained.[34, 35] As

shown in figure 4.2a (when the Ni/Mn ratio in the precursor is 1.5:0.5), in the first two cycles, we cannot find obvious reversible redox reaction peaks, since only a fraction of the material is active. Then, after hundreds of CV cycles, a pair of redox peaks around 0.6 V (vs. Ag/AgCl) show up and their intensities increase gradually along with the activation process (The potential differences between those two peaks also became smaller.), indicating the improvement of the pseudocapacitive performance and reversibility of the reactions (which can be ascribed to redox reactions of Mn^{3+}/Mn^{4+} and this will be discussed in later section). This improvement may be contributed by the insertion of Na+ ions into the electrode materials during CV cycling. Besides the stronger redox peaks, the increasing non-faradaic current (or electric double layer current) of the CV plot can also confirm the active sites of the electrode are increased by the activation process. The CV electrochemical activation processes of electrodes produced from precursors with other Ni/Mn molar ratios are displayed in figure S4.4 a-d and the corresponding calculated specific capacitance changes are plotted in figure 4.2b. In detail, when Ni element is not introduced into the product, the CV curves of MnO_2 (Figure S4.4a) are not rectangular but contain a broad and almost irreversible peak, suggesting its weak pseudocapacitive performance. Whereas, with the incorporation of Ni element (as shown in figure 4.2a and figure S4.4b-c), obvious and reversible peaks can be observed, suggesting that the addition of Ni element can help enhance the electrochemical activity of Mn^{3+}/Mn^{4+} reactions. Besides, when the Ni/Mn ratio in the precursor is 1.5:0.5, the specific capacitance of the prepared electrode shows a value of 279 F g^{-1} at the first CV cycle and, then, increases to 482 F g^{-1} at the last activation cycle which is much larger than the results from any other ratios (table S4.1). Moreover, the CV comparison of electrodes with different Ni/Mn molar ratios in precursor at 500^{th} activation cycle is shown in figure 4.2c. It is important to find that, as the content of Ni element increases, one pair of redox

peaks become more and more prominent during CV activation process, especially when Ni/Mn ratio is 1.5:0.5. In detail, the peaks around 0.69 V (anodic scan) and 0.57 V (cathodic scan) can be ascribed to the oxidation and reduction of Mn^{3+}/Mn^{4+} redox reactions, respectively, and this pair of peaks exhibits the best reversibility as demonstrated by the lowest peak separation value comparing to the results from other samples. Likewise, it needs to be mentioned that, the peaks around 0.88 V (anodic scan) and 0.66 V (cathodic scan) are the reflection of insertion/extraction of Na^+ ions.[27] Besides the peaks, the CV curves also have a rectangular shape at lower potential range (-0.2-0.4V) after activation process, suggesting EDLC behavior. These results can be further confirmed by the reported electrochemical mechanism of MnO_2 based materials as shown in equation (6) and (7):

$$MnO_2 + C^+ + e^- \leftrightarrow MnOOC \quad (6)$$

$$(MnO_2)_{surface} + C^+ + e^- \leftrightarrow (MnO_2{}^- C^+)_{surface} \quad (7)$$

where C^+ indicates alkali metal cations (e.g. Na^+ in our case).[36, 37] The first equation describes the ion insertion/extraction process along with Mn^{3+}/Mn^{4+} redox reactions. Obviously, the occurrence of Mn^{3+}/Mn^{4+} redox reactions strongly relies on that of Na^+ ions insertion/extraction process, implying that the whole process may be diffusion-controlled. The second equation is based on the surface ion adsorption/desorption mechanism, which is typically surface-controlled (Detailed discussion about this topic will be shown in the next section). Thus, according to the shape of CV curve and its underlying charge storage mechanism, A-NiMnBMO is a pseudocapacitive electrode material.[38] In summary, the electrodes made of precursors with different Ni/Mn molar ratios exhibit different electrochemical performances and the incorporation of Ni element (which is usually found in battery type material) can change the electronic structure of MnO_2 (which is a typical pseudocapacitance material).[38, 39] As a result, the

electrochemical activity of Mn^{3+}/Mn^{4+} redox couples can be improved (This conclusion can be obtained by comparing the CV curves of electrodes with and without Ni element.) The insertion/desertion process of Na^{+} during activation process can help increase the active sites of the material. Under the synergetic influences of these two phenomena, the pseudocapacitive performance of A-Ni-MnBMO electrode can be dramatically boosted. In addition, the CV curves of the product made from the precursor with Ni/Mn ratio of 2:0 are shown in figure S4.4d. The CV comparison of A-Ni-MnBMO electrode and bare carbon cloth is shown in figure S4.4e. The CV comparison of A-Ni-MnBMO electrode and electrode produced from precursors with Ni/Mn ratio of 2:0 at 500th activation cycle is shown in figure S4.4f.

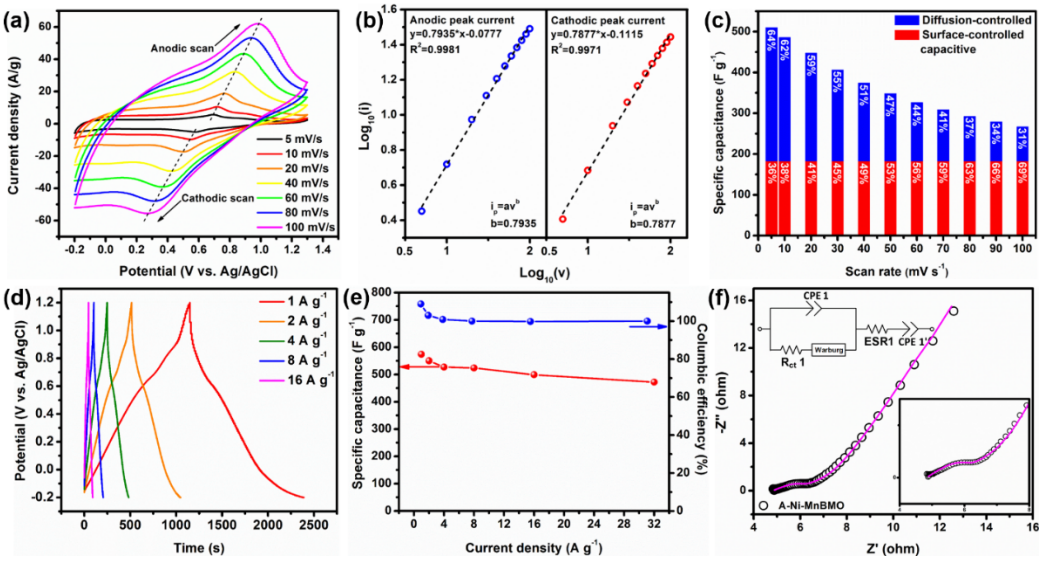

Figure 4.3. (a) CV curves of A-Ni-MnBMO electrode at different scan rates and (b) the corresponding linear fit of log (i) versus log (v) at cathodic and anodic peaks. (c) The calculated specific capacitances from different scan rates of CV and separations of diffusion-controlled and surface-controlled capacitive charge at different scan rates for the A-Ni-MnBMO electrode. (d) GCD curves of A-Ni-MnBMO electrode at different current densities and (e) the corresponding calculated specific capacitances and columbic efficiencies. (f) EIS spectrum and the corresponding fitting model of A-Ni-MnBMO electrode.

The CV curves of A-Ni-MnBMO electrode at different scan rates are shown in figure 4.3a. It can be noticed that, due to the polarization of the electrode at the higher scan rates, the

anodic peaks shift positively and the cathodic peaks shift negatively as the scan rate increases from 5 to 100 mV s^{-1}.[40] Furthermore, the area under CV curves represents the total stored charge which may contribute from both faradaic (charge-transfer process of surface atoms or ion insertion/extraction process) and non-faradaic processes (EDLC). These contributions can be estimated by the equation (8) and (9):

$$i_p = av^b \quad (8)$$

$$\log(i_p) = b \times \log(v) + \log(a) \quad (9)$$

where i_p is the peak current, v is the corresponding scan rate and both a and b are adjustable parameters. The value of b can be determined from the slope of $\log(i_p)$ versus $\log(v)$ and there are two well-defined conditions based on this value. Generally, when b-value is 0.5, the CV describes the process of diffusion-controlled faradaic insertion/extraction reactions. Whereas, if b-value is 1, the performance of electrode only arises from pure surface capacitive process.[41, 42]

In figure 4.3b, the calculated b values for both cathodic and anodic peak currents are close to 0.79, implying that the electrochemical performance of A-Ni-MnBMO electrode are controlled by not only the diffusion-controlled insertion/extraction reaction but also the surface-controlled capacitive process. The pseudocapacitive contributions at different scan rates can be estimated by the equation (10) and (11):

$$i = k_1 v + k_2 v^{1/2} \quad (10)$$

$$i/v^{1/2} = k_1 v^{1/2} + k_2 \quad (11)$$

where $k_1 v$ and $k_2 v^{1/2}$ represent the current contributions from surface-controlled capacitive process and diffusion-controlled insertion/extraction reaction, respectively.[41, 42, 43] The diffusion-controlled and surface-controlled capacitive contributions to the total stored charge of

the A-Ni-MnBMO electrode and the corresponding calculated specific capacitance at different scan rates are shown in figure 4.3c. It can be observed that, at 5 mV s^{-1}, the specific capacitance is 510 F g^{-1} and 64% of the capacitance is from diffusion-controlled insertion/extraction reaction which is larger than the contribution from surface-controlled capacitive process. When the scan rate increases to 100 mVs^{-1}, the specific capacitance still retains 266 F g^{-1} and the diffusion-controlled contribution drops to 31%. It is interesting to find out that, even though the surface-controlled capacitive contribution increases from 36% to 69 % with the increase of scan rate, its corresponding estimated specific capacitance remains a constant value of about 183 F g^{-1}, suggesting the quite stable surface charge storage for the A-Ni-MnBMO electrode. Although the diffusion-controlled Mn^{3+}/Mn^{4+} reactions can help provide high energy density for the supercapacitor through the charge transfer process, its relatively sluggish kinetics, compared with that of fast surface-controlled capacitive process, is not able to obtain high power density which is always be found in batteries.[44] However, the stable surface-controlled capacitive process can help maintain high power density. Based on the above results, the combination of diffusion-controlled and surface-controlled capacitive processes in A-Ni-MnBMO electrode can contribute to make a device which has high energy density and still maintain relatively high power at the same time. Then, the maximum working potential for A-Ni-MnBMO electrode that prevents the occurrence of oxygen evolution reaction is determined to be 1.2 V (V vs. Ag/AgCl) by CV test and the detailed explanation is shown in figure S4.5a-b and figure S4.6. In addition, figure 4.3d presents the GCD curves of A-Ni-MnBMO electrode between -0.2 and 1.2 V (vs. Ag/AgCl) at different current densities from 1 to 32 A g^{-1} and the detailed data is shown in table S4.2. The shape of these curves are neither linear line nor plateaus of nearly constant potential, further suggesting that the prepared A-Ni-MnBMO belongs to the category of pseudocapacitance

material.[38, 39] The calculated results in figure 4.3e indicates that the electrode has a specific capacitance of 574 F g^{-1} at the current density of 1 A g^{-1}, and as the current density increases to 16 A g^{-1}, the specific capacitance slightly drops to 499 F g^{-1}. When the applied current density is 32 A g^{-1}, a high specific capacitance of 472 F g^{-1} can still be achieved from this electrode, further confirming its good rate capability. Moreover, the values of the corresponding coulombic efficiencies at different current densities (also shown in figure 4.3e) are close to 100 %. EIS curve of A-Ni-MnBMO electrode is measured in the three-electode system within a frequency range from 0.1 Hz to 100 kHz (DC=0.334 V and AC=10 mV). The Nyquist plot of A-Ni-MnBMO electrode shown in figure 4.3f can be fitted by the modified Randles circuit shown in the inset. ESR represents the equivalent series resistance (consisting of the resistances from electrolyte and electrode material) and the fitted value of ESR1 is about 4.838 ohm (table S4.3). A parallel connected CPE (constant phase element) and R_{ct} (charge transfer resistance which is about 8.813 ohm from fitting model) are used to model the behavior of real capacitor. A Warburg impedance element is also included in the circuit for modeling the diffusion process. An extra CPE which may be ascribed to interfacial contact capacitance is also added into the circuit in order to obtain better fitting result.

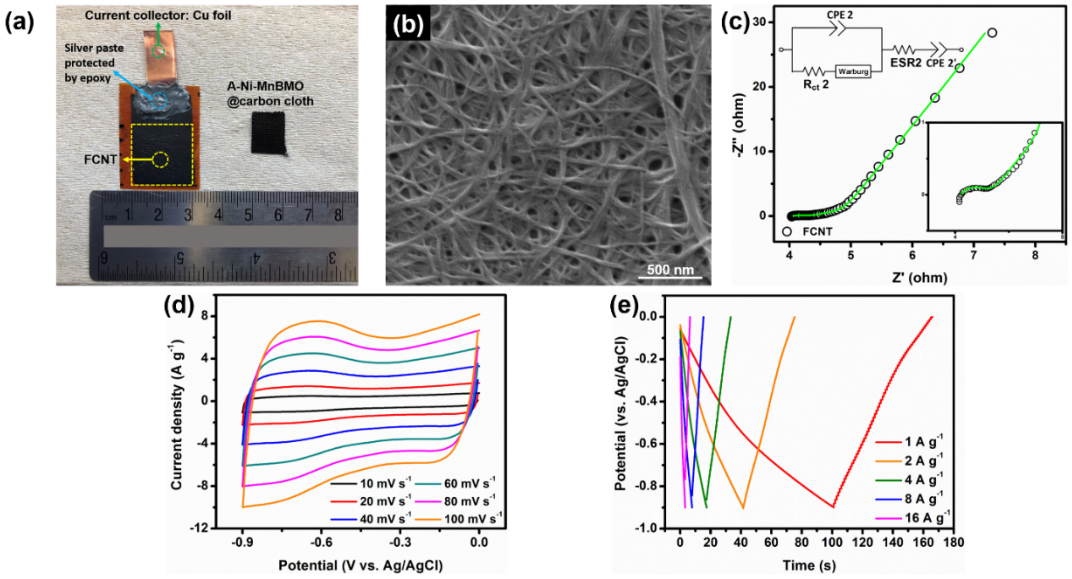

Figure 4.4. (a) Digital images of FCNT and A-Ni-MnBMO electrodes. (b) SEM image of FCNT. (c) EIS spectrums and the corresponding fitting models of FCNT electrode. (d) CV curves of FCNT electrode at different scan rates. (e) GCD curves of FCNT electrode at different current densities.

For negative electrode shown in figure 4.4a, hydrophilic FCNT is drop casted on the surface of kapton film and is connected with a piece of copper foil through silver paste. Copper foil is used as the electrical contact and silver paste is protected by epoxy from the possible corrosion caused by aqueous electrolyte. The digital image of A-Ni-MnBMO grown on carbon cloth is also shown in figure 4.4a. Besides, the morphology of CNT network can be observed from SEM image of FCNT electrode shown in figure 4.4b, which is consistent with our previous work.[29] EIS curve of FCNT electrode within a frequency range from 0.1 Hz to 100 kHz (DC=0.18 V and AC=10 mV) is shown in figure 4.4c and the Nyquist curve can also be fitted by the modified Randles circuit. The fitted value of ESR2 is about 4.059 ohm (table S4.3). The lowest potential value which prevents the occurrence of hydrogen evolution reaction of FCNT electrode is measured to be -0.9 V (vs. Ag/AgCl) and the detailed explanation is displayed in figure S4.5c. In addition, the corresponding CV tests at different scan rates and GCD tests at

different current densities are displayed in figure 4.4d and e, respectively. The almost square shape of CV curves and linear shape of GCD plots suggests the working mechanism of FCNT electrode is mainly EDLC. However, when the scan rate of CV tests increases (especially from 40 to 100 mV s^{-1}), small humps (which may be caused by redox reactions of oxygen contained functional groups or hydrogen adsorption/desorption) can be observed. The detailed analysis can be found in figure S4.7. These possible processes can provide extra pseudocapacitance for FCNT electrode.

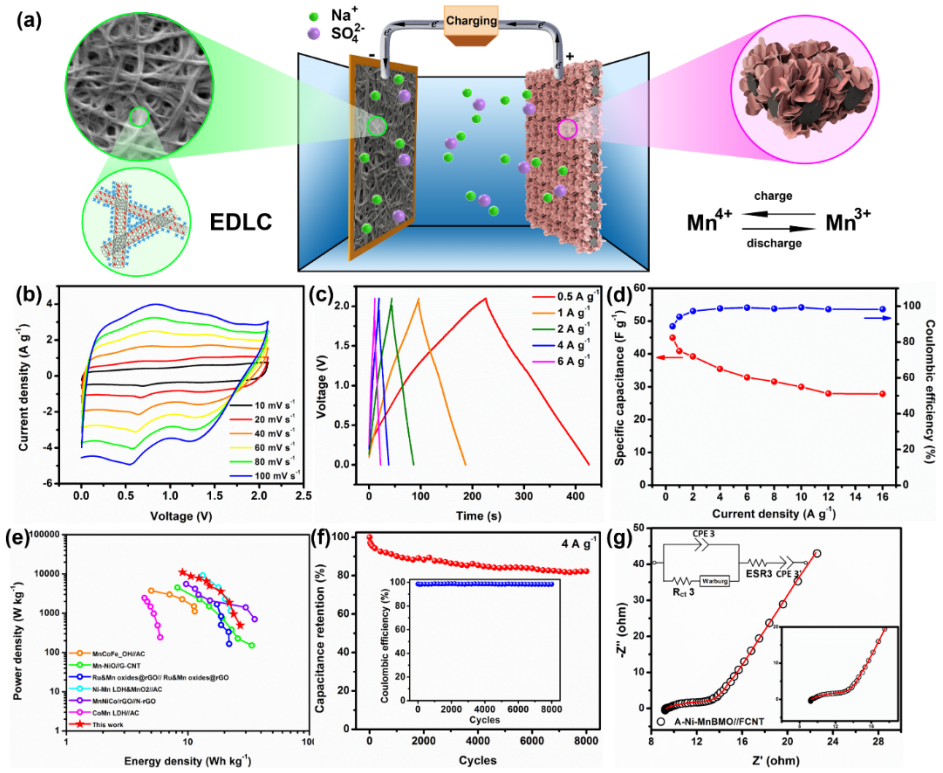

Figure 4.5. (a) Schematic illustration of A-Ni-MnBMO//FCNT supercapacitor. (b) CV curves of A-Ni-MnBMO//FCNT supercapacitor at different scan rates. (c) GCD curves of A-Ni-MnBMO//FCNT supercapacitor at different current densities and (d) the corresponding calculated specific capacitances and columbic efficiencies. (e) Ragone plot of A-Ni-MnBMO//FCNT supercapacitor. (f) Cyclic performance of A-Ni-MnBMO//FCNT supercapacitor at the current density of 4 A g^{-1}. Inset is the corresponding coulombic efficiencies. (g) EIS spectrums and the corresponding fitting models of A-Ni-MnBMO//FCNT supercapacitor.

As the schematic illustration shown in figure 4.5a, A-Ni-MnBMO//FCNT supercapacitor is produced by coupling the pseudocapacitive A-Ni-MnBMO positive electrode and the EDLC FCNT negative electrode in the 1 M Na_2SO_4 electrolyte. Since the maximum working potentials of positive and negative electrodes are 1.2 V and -0.9 V (vs. Ag/AgCl), respectively, a maximum working voltage of 2.1 V can be obtained in the A-Ni-MnBMO//FCNT supercapacitor. The CV curves of A-Ni-MnBMO//FCNT supercapacitor at different scan rates is given in figure 4.5b and the shape of those curves are not square but contain several peaks, reflecting the characteristic behavior of ASC. Besides, the GCD curves of A-Ni-MnBMO//FCNT supercapacitor with a voltage window of 2.1 V at different current densities from 0.5 to 16 A g^{-1} are measured as shown in figure 4.5c and the detailed data is shown in table S4.4. The calculated results (based on the mass of active materials on both electrodes) in figure 4.5d shows that the specific capacitance of the supercapacitor is 45 F g^{-1} (with the coulombic efficiency of 88.8 %) at the current density of 0.5 A g^{-1} and the value is changed to 28 F g^{-1} (with the coulombic efficiency of 98.3 %) when the current density is 16 A g^{-1}. Moreover, according the GCD curves at different current densities, energy density and powder density of A-Ni-MnBMO//FCNT supercapacitor are calculated (by using equation (2) and (3)) and shown in Ragone plot (figure 4.5e). It can be found that A-Ni-MnBMO//FCNT supercapacitor can deliver a maximum energy density of 27 Wh kg^{-1} with the power density of 486.6 W kg^{-1} at the current density is 0.5 A g^{-1} and a maximum power density of 11049.2 W kg^{-1} with the energy density of 9 Wh kg^{-1} whe n the current density is 16 A g^{-1}, which is better than some previously reported MnO_2 based supercapacitors.[45, 46, 47, 48, 49, 50] The cyclic performance of A-Ni-MnBMO//FCNT supercapacitor is investigated in figure 4.5f and 82.3 % of its initial specific capacitance can be retained after 8000 cycles of GCD tests at a current density of 4 A g^{-1}. The corresponding coulombic

efficiencies are stabilized around 98.5 %, reflecting the good stability of the cell. The morphology of A-Ni-MnBMO electrode after 3000-cycle cell level GCD tests are shown in figure S4.8. It can be observed that the nanosheets structure can still be maintained after 3000 cycles, further indicating its good structure stability. EIS curve of A-Ni-MnBMO//FCNT supercapacitor is tested under a two-electrode system within a frequency range from 0.1 Hz to 100 kHz (DC=0.3 V and AC=10 mV) shown in figure 4.5g and the Nyquist curve can also be fitted by an modified Randles circuit. The obtained value of ESR3 is about 9.310 ohm and this value is very close to the summation of ESR1 and ESR2 (table S4.3), which is consistent to the composition structure of A-Ni-MnBMO//FCNT supercapacitor. The self-discharge performance of A-Ni-MnBMO//FCNT supercapacitor is given in figure S4.9. The voltage drops quickly from 2.1V to 1V with 1 hour and, then, slowly drops to 0.545 V during the following 23 hours. The reason for the fast voltage drop in the 1st hour can be found by measuring the potential change of positive and negative electrodes as shown in the inset of figure S4.9. It can be recognized that the potential of positive electrode (red line) drops from 1.2 V to 0.86 V (vs. Ag/AgCl) in the 1st hour and it slowly approaches to 0.55 V (vs. Ag/AgCl) at the 24^{th} hour. This potential change can be explained by the CV curves shown in figure 4.2a. In detail, since there is a strong redox peak located at 0.57 V (vs. Ag/AgCl) during cathodic scan of CV, indicating that the potential of the electrode will have a great chance to be pinned at around this potential after a fast drop from 1.2 V (vs. Ag/AgCl) in the self-discharge process. By contrast, the mechanism of the negative electrode is EDLC, meaning that there are no redox reactions at the negative electrode to sustain its potential. Therefore, the self-discharge current makes the potential of negative electrode (blue line) change linearly from -0.9 V to the value closed to 0 V (vs. Ag/AgCl) within 1 hour and, then, maintain this value for the rest 23 hours. Thus, the voltage drop is mainly caused by fast

potential increase of FCNT negative electrode. In total, it can be concluded that the self-discharge result is consistent with the cell design of A-Ni-MnBMO//FCNT supercapacitor, and the performance of the supercapacitor can be further improved if a suitable redox reaction (with high reaction rate which will not affect power density too much) that happens within the stable window of the neutral Na_2SO_4 electrolyte can be introduced to the negative electrode. This will be the work to be investigated in the future.

4.5 Conclusion

In this work, Ni-Mn bimetallic oxide nanosheets are synthesized on carbon cloth substrate for high performance electrode in supercapacitor through a facile one-step hydrothermal method. It has been discussed that the pseudocapacitive performance of the prepared A-Ni-MnBMO mostly originates from the redox reactions of Mn^{3+}/Mn^{4+} whose reversibility and activity can be boosted by the combination of the increased material active sites caused by Na^+ insertion/desertion after CV activation process and the change of the electronic structure of MnO_2 through the incorporation of Ni. As a result, A-Ni-MnBMO electrode shows a maximum specific capacitance of 510 F g^{-1} (tested by CV within a potential range of -0.2-1.3 V vs. Ag/AgCl at 5 mV s^{-1}). For GCD tests, after excluding the effects of OER, A-Ni-MnBMO can exhibit a maximum specific capacitance of 574 F g^{-1} (tested with a potential range of -0.2-1.2 V vs. Ag/AgCl at 1A g^{-1}). Moreover, in order to confirming the possibility of using A-Ni-MnBMO electrode as the positive electrode in supercapacitor, a 2.1V A-Ni-MnBMO//FCNT supercapacitor, which can deliver a maximum energy density of 27 Wh kg^{-1} (at 0.5 A g^{-1}) and a maximum power density of 11049.2 W kg^{-1} (at 16 A g^{-1}), is produced. The device can maintain 82.3 % of its initial specific capacitance after 8000 cycles of GCD tests at 4 A g^{-1} and its self-discharge performance is also discussed.

4.6 References

(1) Argyrou, M. C.; Christodoulides, P.; Kalogirou, S. A. Energy Storage for Electricity Generation and Related Processes: Technologies Appraisal and Grid Scale Applications. Renew. Sustain. Energy Rev. 2018, 94, 804–821.

(2) Das, H. S.; Tan, C. W.; Yatim, A. H. M. Fuel Cell Hybrid Electric Vehicles: A Review on Power Conditioning Units and Topologies. Renew. Sustain. Energy Rev. 2017, 76, 268–291.

(3) Liu, H.; Li, M.; Kaner, R. B.; Chen, S.; Pei, Q. Monolithically Integrated Self-Charging Power Pack Consisting of a Silicon Nanowire Array/Conductive Polymer Hybrid Solar Cell and a Laser-Scribed Graphene Supercapacitor. ACS Appl. Mater. Interfaces 2018, 10, 15609–15615.

(4) Dong, X.; Jin, H.; Wang, R.; Zhang, J.; Feng, X.; Yan, C.; Chen, S.; Wang, S.; Wang, J.; Lu, J. High Volumetric Capacitance, Ultralong Life Supercapacitors Enabled by Waxberry-Derived Hierarchical Porous Carbon Materials. Adv. Energy Mater. 2018, 8, 1702695.

(5) Wang, F.; Wu, X.; Yuan, X.; Liu, Z.; Zhang, Y.; Fu, L.; Zhu, Y.; Zhou, Q.; Wu, Y.; Huang, W. Latest Advances in Supercapacitors: From New Electrode Materials to Novel Device Designs. Chemical Society Reviews, 2017, 46, 6816–6854.

(6) Lee, T. H.; Pham, D. T.; Sahoo, R.; Seok, J.; Luu, T. H. T.; Lee, Y. H. High Energy Density and Enhanced Stability of Asymmetric Supercapacitors with Mesoporous MnO2@CNT and Nanodot MoO3@CNT Free-Standing Films. Energy Storage Mater. 2018, 12, 223–231.

(7) Lee, J. S. M.; Briggs, M. E.; Hu, C. C.; Cooper, A. I. Controlling Electric Double-Layer Capacitance and Pseudocapacitance in Heteroatom-Doped Carbons Derived from Hypercrosslinked Microporous Polymers. Nano Energy 2018, 46, 277–289.

(8) Long, J. W.; Bélanger, D.; Brousse, T.; Sugimoto, W.; Sassin, M. B.; Crosnier, O. Asymmetric Electrochemical Capacitors-Stretching the Limits of Aqueous Electrolytes. MRS Bull. 2011, 36, 513–522.

(9) Choudhary, N.; Li, C.; Moore, J.; Nagaiah, N.; Zhai, L.; Jung, Y.; Thomas, J. Asymmetric Supercapacitor Electrodes and Devices. Adv. Mater. 2017, 29, 1605336.

(10) Sahoo, R.; Pham, D. T.; Lee, T. H.; Luu, T. H. T.; Seok, J.; Lee, Y. H. Redox-Driven Route for Widening Voltage Window in Asymmetric Supercapacitor. ACS Nano 2018, 12, 8494–8505.

(11) Zhang, L. L.; Zhou, R.; Zhao, X. S. Carbon-Based Materials as Supercapacitor Electrodes. J. Mater. Chem. 2009, 38, 2520–2531.

(12) Dong, X.; Jin, H.; Wang, R.; Zhang, J.; Feng, X.; Yan, C.; Chen, S.; Wang, S.; Wang, J.; Lu, J. High Volumetric Capacitance, Ultralong Life Supercapacitors Enabled by Waxberry-Derived Hierarchical Porous Carbon Materials. Adv. Energy Mater. 2018, 8, 1702695.

(13) Wang, G.; Lei, Z.; Jiujun, Z. A Review of Electrode Materials for Electrochemical Supercapacitors. ChemsucChem 2012, 5, 797.

(14) Li, X.; Elshahawy, A. M.; Guan, C.; Wang, J. Metal Phosphides and Phosphates-Based Electrodes for Electrochemical Supercapacitors. Small, 2017, 13, 1701530.

(15) Huang, M.; Li, F.; Dong, F.; Zhang, Y. X.; Zhang, L. L. MnO2-Based Nanostructures for High-Performance Supercapacitors. Journal of Materials Chemistry A, 2015, 3, 21380–21423.

(16) Wang, J. G.; Kang, F.; Wei, B. Engineering of MnO2-Based Nanocomposites for High-Performance Supercapacitors. Prog. Mater. Sci. 2015, 74, 51–124.

(17) Lee, H. Y.; Goodenough, J. B. Supercapacitor Behavior with KCl Electrolyte. J. Solid State Chem. 1999, 144, 220–223.

(18) Zhu, C.; Yang, L.; Seo, J. K.; Zhang, X.; Wang, S.; Shin, J.; Chao, D.; Zhang, H.; Meng, Y. S.; Fan, H. J. Self-Branched α-MnO 2 /δ-MnO 2 Heterojunction Nanowires with Enhanced Pseudocapacitance. Mater. Horiz. 2017, 4, 415–422.

(19) Vinny, R. T.; Chaitra, K.; Venkatesh, K.; Nagaraju, N.; Kathyayini, N. An Excellent Cycle Performance of Asymmetric Supercapacitor Based on Bristles like α-MnO2nanoparticles Grown on Multiwalled Carbon Nanotubes. J. Power Sources 2016, 309, 212–220.

(20) Wang, Q.; Zhu, Y.; Xue, J.; Zhao, X.; Guo, Z.; Wang, C. General Synthesis of Porous Mixed Metal Oxide Hollow Spheres with Enhanced Supercapacitive Properties. ACS Appl. Mater. Interfaces 2016, 8, 17226–17232.

(21) Tajik, S.; Dubal, D. P.; Gomez-Romero, P.; Yadegari, A.; Rashidi, A.; Nasernejad, B.; Inamuddin; Asiri, A. M. Nanostructured Mixed Transition Metal Oxides for High Performance Asymmetric Supercapacitors: Facile Synthetic Strategy. Int. J. Hydrogen Energy 2017, 42, 12384–12395.

(22) Chen, D.; Wang, Q.; Wang, R.; Shen, G. Ternary Oxide Nanostructured Materials for Supercapacitors: A Review. Journal of Materials Chemistry A, 2015, 3, 10158–10173.

(23) Yuan, C.; Wu, H. Bin; Xie, Y.; Lou, X. W. Mixed Transition-Metal Oxides: Design, Synthesis, and Energy-Related Applications. Angewandte Chemie - International Edition, 2014, 53, 1488–1504.

(24) Zhang, Y.; Li, L.; Su, H.; Huang, W.; Dong, X. Binary Metal Oxide: Advanced Energy Storage Materials in Supercapacitors. Journal of Materials Chemistry A, 2015, 3, 43–59.

(25) Zhang, Y.; Li, L.; Su, H.; Huang, W.; Dong, X. Binary Metal Oxide: Advanced Energy Storage Materials in Supercapacitors. Journal of Materials Chemistry A, 2015, 3, 43–59.

(26) Tang, C. L.; Wei, X.; Jiang, Y. M.; Wu, X. Y.; Han, L. N.; Wang, K. X.; Chen, J. S. Cobalt-Doped MnO2 Hierarchical Yolk-Shell Spheres with Improved Supercapacitive Performance. J. Phys. Chem. C 2015, 119, 8465–8471.

(27) Jabeen, N.; Hussain, A.; Xia, Q.; Sun, S.; Zhu, J.; Xia, H. High-Performance 2.6 V Aqueous Asymmetric Supercapacitors Based on In Situ Formed Na0.5MnO2Nanosheet Assembled Nanowall Arrays. Adv. Mater. 2017, 29, 1–9.

(28) Jabeen, N.; Xia, Q.; Savilov, S. V.; Aldoshin, S. M.; Yu, Y.; Xia, H. Enhanced Pseudocapacitive Performance of α-MnO 2 by Cation Preinsertion. ACS Appl. Mater. Interfaces 2016, 8, 33732–33740.

(29) Tang, X.; Lui, Y. H.; Chen, B.; Hu, S. Functionalized Carbon Nanotube Based Hybrid Electrochemical Capacitors Using Neutral Bromide Redox-Active Electrolyte for Enhancing Energy Density. J. Power Sources 2017, 352, 118–126.

(30) Tang, X.; Lui, Y. H.; Merhi, A. R.; Chen, B.; Ding, S.; Zhang, B.; Hu, S. Redox-Active Hydrogel Polymer Electrolytes with Different PH Values for Enhancing the Energy Density of the Hybrid Solid-State Supercapacitor. ACS Appl. Mater. Interfaces 2017, 9, 44429–44440.

(31) Zuo, W.; Xie, C.; Xu, P.; Li, Y.; Liu, J. A Novel Phase-Transformation Activation Process toward Ni–Mn–O Nanoprism Arrays for 2.4 V Ultrahigh-Voltage Aqueous Supercapacitors. Adv. Mater. 2017, 29, 1–9.

(32) Wang, J. G.; Yang, Y.; Huang, Z. H.; Kang, F. A High-Performance Asymmetric Supercapacitor Based on Carbon and Carbon-MnO2nanofiber Electrodes. Carbon N. Y. 2013, 61, 190–199.

(33) Yu, C.; Wang, Y.; Zhang, J.; Shu, X.; Cui, J.; Qin, Y.; Zheng, H.; Liu, J.; Zhang, Y.; Wu, Y. Integration of Mesoporous Nickel Cobalt Oxide Nanosheets with Ultrathin Layer Carbon Wrapped TiO2nanotube Arrays for High-Performance Supercapacitors. New J. Chem. 2016, 40, 6881–6889.

(34) Hosseini, H.; Shahrokhian, S. Advanced Binder-Free Electrode Based on Core–Shell Nanostructures of Mesoporous Co3V2O8-Ni3V2O8 Thin Layers@porous Carbon Nanofibers for High-Performance and Flexible All-Solid-State Supercapacitors. Chem. Eng. J. 2018, 341, 10–26.

(35) Tamaddoni Saray, M.; Hosseini, H. Mesoporous MnNiCoO4@MnO2 Core-Shell Nanowire/Nanosheet Arrays on Flexible Carbon Cloth for High-Performance Supercapacitors. Electrochim. Acta 2016, 222, 505–517.

(36) Toupin, M.; Brousse, T.; Bélanger, D. Charge Storage Mechanism of MnO 2 Electrode Used in Aqueous Electrochemical Capacitor. 2004.

(37) Tanggarnjanavalukul, C.; Phattharasupakun, N.; Wutthiprom, J.; Kidkhunthod, P.; Sawangphruk, M. Charge Storage Mechanisms of Birnessite-Type MnO2 Nanosheets in Na2SO4 Electrolytes with Different PH Values: In Situ Electrochemical X-Ray Absorption Spectroscopy Investigation. Electrochim. Acta 2018, 273, 17–25.

(38) Hosseini, H.; Shahrokhian, S. Vanadium Dioxide-Anchored Porous Carbon Nanofibers as a Na+ Intercalation Pseudocapacitance Material for Development of Flexible and Super Light Electrochemical Energy Storage Systems. Appl. Mater. Today 2018, 10, 72–85.

(39) Energy Storage in Nanomaterials-Capacitive, Pseudocapacitive, or Battery-Like? 2018.

(40) Liu, W.; Lu, C.; Wang, X.; Liang, K.; Tay, B. K. In Situ Fabrication of Three-Dimensional, Ultrathin Graphite/Carbon Nanotube/NiO Composite as Binder-Free Electrode for High-Performance Energy Storage. J. Mater. Chem. A 2015, 3, 624–633.

(41) Dong, Y.; Li, D.; Gao, C.; Liu, Y.; Zhang, J. A Self-Assembled 3D Urchin-like Ti0.8Sn0.2O2-RGO Hybrid Nanostructure as an Anode Material for High-Rate and Long Cycle Life Li-Ion Batteries. J. Mater. Chem. A 2017, 5, 8087–8094.

(42) Tang, B.; Fang, G.; Zhou, J.; Wang, L.; Lei, Y.; Wang, C.; Lin, T.; Tang, Y.; Liang, S. Potassium Vanadates with Stable Structure and Fast Ion Diffusion Channel as Cathode for Rechargeable Aqueous Zinc-Ion Batteries. Nano Energy 2018, 51, 579–587.

(43) Ding, C.; Huang, T.; Tao, Y.; Tan, D.; Zhang, Y.; Wang, F.; Yu, F.; Xie, Q. Identifying the Origin and Contribution of Pseudocapacitive Sodium Ion Storage in Tungsten Disulphide Nanosheets for Application in Sodium-Ion Capacitors. J. Mater. Chem. A 2018, 6, 21010–21017.

(44) Wang, F.; Liu, Z.; Zhang, P.; Li, H.; Sheng, W.; Zhang, T.; Jordan, R.; Wu, Y.; Zhuang, X.; Feng, X. Dual-Graphene Rechargeable Sodium Battery. Small 2017, 13, 1702449.

(45) Elkholy, A. E.; El-Taib Heakal, F.; Allam, N. K. A Facile Electrosynthesis Approach of Amorphous Mn-Co-Fe Ternary Hydroxides as Binder-Free Active Electrode Materials for High-Performance Supercapacitors. Electrochim. Acta 2019, 296, 59–68.

(46) Han, X.; Wang, B.; Yang, C.; Meng, G.; Zhao, R.; Hu, Q.; Triana, O.; Iqbal, M.; Li, Y.; Han, A.; et al. Inductive Effect in Mn-Doped NiO Nanosheet Arrays for Enhanced Capacitive and Highly Stable Hybrid Supercapacitor. ACS Appl. Energy Mater. 2019, acsaem.8b02129.

(47) Annamalai, K. P.; Zheng, X.; Gao, J.; Chen, T.; Tao, Y. Nanoporous Ruthenium and Manganese Oxide Nanoparticles/Reduced Graphene Oxide for High-Energy Symmetric Supercapacitors. Carbon N. Y. 2019, 144, 185–192.

(48) Quan, W.; Jiang, C.; Wang, S.; Li, Y.; Zhang, Z.; Tang, Z.; Favier, F. New Nanocomposite Material as Supercapacitor Electrode Prepared via Restacking of Ni-Mn LDH and MnO2 Nanosheets. Electrochim. Acta 2017, 247, 1072–1079.

(49) Wu, C.; Cai, J.; Zhu, Y.; Zhang, K. Hybrid Reduced Graphene Oxide Nanosheet Supported Mn–Ni–Co Ternary Oxides for Aqueous Asymmetric Supercapacitors. ACS Appl. Mater. Interfaces 2017, 9, 19114–19123.

(50) Jagadale, A. D.; Guan, G.; Li, X.; Du, X.; Ma, X.; Hao, X.; Abudula, A. Ultrathin Nanoflakes of Cobalt–Manganese Layered Double Hydroxide with High Reversibility for Asymmetric Supercapacitor. J. Power Sources 2016, 306, 526–534.

CHAPTER 5. VENUS FLYTRAP-LIKE HIERARCHICAL NICOMN-O@NIMOO$_4$@C NANOSHEET ARRAYS AS FREE-STANDING CORE-SHELL ELECTRODE MATERIAL FOR HYBRID SUPERCAPACITOR WITH HIGH ELECTROCHEMICAL PERFORMANCE

Xiaohui Tang, Yui Hui Lui, Bowei Zhang and Shan Hu*

Department of Mechanical Engineering, Iowa State University, Ames, Iowa, 50010, USA
*Corresponding author Email: shanhu@iastate.edu

Modified from a manuscript to be submitted to "J. Mater. Chem. A".

Note: The supporting information is shown in APPENDIX D.

5.1 Abstract

In order to improve the sluggish kinetics of the redox reactions occurring at the battery-type electrodes of hybrid supercapacitors, a Venus flytrap-like hierarchical NiCoMn-O@NiMoO$_4$@C nanosheet arrays electrode material are developed based on three aspects of considerations: 1. The developed NiCoMn-based trimetallic (NiCoMn-O) oxide has better electrical conductivity than any of its bimetallic or monometallic counterparts and the self-decorated nanoneedles on its surface can create more electroactive surface area for electrolyte to access. 2 NiMoO$_4$ layer is the most important redox active material in this composite since its high electrochemical activity in alkaline solution. 3. Carbon protection shell cannot only increase the electric conductivity of the composite but also improve its cycling stability via buffering the volume change during the charge/discharge processes. As a result, the obtained NiCoMn-O@NiMoO$_4$@C electrode can provide a maximum specific capacitance of 2189.5 F/g (at 0.25 A/g) and 81.6 % of its initial specific capacitance can be maintained after 1500 cycles GCD tests (at 6 A/g). The prepared NiCoMn-O@NiMoO$_4$@C//AC hybrid supercapacitor exhibits the maximum energy density of 59.9 Wh/kg (at 0.25 A/g) and its specific capacitance can maintain 88.3 % of its initial value after 3000 cycles GCD tests (at 6 A/g).

5.2 Introduction

Comparing with fossil fuels, renewable energies (such as wind energy, water energy and solar energy, etc.) have currently fetched much limelight by virtue of their characteristics of almost zero-carbon-emission.[1, 2] However, the electricity generated from renewable energies is usually intermittent so that it is necessary to develop efficient energy storage devices (such as fuel cells, batteries, conventional capacitors and supercapacitors) in order to collect this unstable energy source and, then, dispatch it to the electric power system upon demand. Owing to their relatively higher energy density (than conventional capacitors) along with longer cycle life and higher power density (than batteries), supercapacitors, including electric double-layer capacitors (EDLC), asymmetric supercapacitors and hybrid supercapacitors, are well suited for applications requiring short term energy storage and rapid charge/discharge power supply.[3] Particularly, hybrid supercapacitors, typically constructed by a battery-type electrode with faradaic redox reactions for obtaining elevated energy density and a EDLC-type electrode which stores energy via fast accumulation/dissipation of charge on the surface of carbon based material (with high surface area) to assure high power density, have the potential of providing better performance than the other two types of supercapacitors.[4]

However, the commercialization of hybrid supercapacitors has still been hindered, since the sluggish redox reactions, low electrical conductivity and poor cycling stability of battery-type electrodes (which are usually made of metal oxides, for example NiO, Bi_2O_3 and Fe_3O_4), to a large extent, limit the power performance.[5] Fortunately, it has been confirmed by many works that nanostructured materials with moderately reduced dimensions via certain synthesis strategies can effectively shorten the ion diffusion pathway and improve the penetration of electrolyte so that the kinetics of the redox reactions can be boosted.[6, 7, 8] For instance, Duraisamy et al. has

demonstrated that the synthesized nanostructured NiO with the particle size of 6 nm exhibited the specific capacitance of 449 F/g which is much higher than that of NiO with larger particle size of 21 nm (323 F/g) and 41 nm (63 F/g). Their explanation mentioned that the stack of smaller particles can narrow the ion diffusion channel which can enhance the faradaic redox reaction process.[9] Lin et al. managed to synthesize large amount of tiny nanoneedles on the surface of $NiCo_2S_4$ nanosheet arrays via a two-step hydrothermal method and the generated hierarchical structured material can produce higher specific capacitance than the pure nanosheet material which is because the additional nanoneedles exposed more electroactive surface area for the electrolyte to access (i.e. The ion diffusion path is shortened).[10]

Besides, it has been testified that the mixed-metallic oxides/hydroxides (such as bimetallic oxides/hydroxides and trimetallic oxides/hydroxides), compared to their monometallic counterparts, are able to provide better electrochemical activity and higher electrical conductivity.[11, 12, 13] The possible reasons for these improvements are attributed to the synergistic effect of the multiple metal species existing in the mixed-metallic oxides/hydroxides which have different valence states interchange so that diverse redox reactions can happen; and the relatively low activation energy for electron transfer between cations so that higher electrical conductivity can be obtained.[14, 15, 16] For example, Cai et al. reported that their prepared $NiMoO_4$ has higher specific capacitance and better electrical conductivity than these of NiO.[17] Chen et al. has compared the electrochemical performance of their developed amorphous NiCoMn-OH electrode material (for hybrid supercapacitor) to the corresponding amorphous hydroxides with different transitional metal combinations (including NiCo-OH, NiMn-OH, CoMn-OH, Ni-OH, Co-OH and Mn-OH) via galvanostatic charge and discharge (GCD) tests. The electrodes of the obtained specific capacities arranged from high to low are NiCoMn-OH, NiCo-OH, Ni-OH,

NiMn-OH, Mn-OH, Co-OH, CoMn-OH (at the current density of 10 A/g).[12] In the meanwhile, Zhu et al. did the similar tests and the sequences of the electrodes with performance from higher to lower values are NiCoMn-OH, NiMn-OH, Ni-OH, NiCo-OH, Co-OH and CoMn-OH.[14] From these reports, two conclusions can be made: 1. Not all mixed-metallic oxides/hydroxides have better performances than their corresponding monometallic counterparts. It depends on the synthesis methods along with the structure and morphology of the final product. 2. NiCoMn-based oxides/hydroxides have the potential of achieving better electrochemical performance than that of any corresponding monometallic and bimetallic counterparts.

Moreover, the ability of enhancing the electrical conductivity of electrode material through producing mixed-metallic oxides/hydroxides is still limited. Thus, it is crucial to utilize other methods to do some further improvement. Notably, it is found that the addition of carbon materials (such as carbon nanotube, graphene and amorphous carbon, etc.) into metal oxides/hydroxides to form a composite can create channels for charge transport and, in some cases, serve as physical support of metal oxides.[18, 19] As a result, the overall performance of the electrode material can be boosted. For instance, Nagaraju et al. developed forest-like nickel oxide nanosheet grafted carbon nanotube coupled copper oxide nanowire arrays on the surface of old cable copper wires (NiO NSs@CNTs@CuO NWAs/Cu fibers) and it has been demonstrated that the incorporation of carbon nanotube into this composite can improve its electron transfer kinetics and electrochemical conductivities.[20] Li et al. successfully coated carbon shell with the thickness of 5 nm (which is derived from glucose) on the surface of Fe_3O_4 nanorods. Based on the report, the carbon shell cannot only increase the electrical conductivity of Fe_3O_4 nanorods, but also buffer their volume change during the charge/discharge processes (which usually

happens in electrodes made of nanostructured metal oxides) so that its cycling stability can greatly be enhanced.[21, 22, 23, 24, 25]

Based on the above consideration, we herein propose a method to synthesize Venus flytrap-like hierarchical NiCoMn-based trimetallic oxides nanosheet arrays grafted by $NiMoO_4$ nanolayer coated by carbon protection shell (NiCoMn-O@$NiMoO_4$@C) on the surface of carbon cloth fiber as free-standing core-shell electrode material for hybrid supercapacitor. Briefly, hierarchical NiCoMn-O nanosheet arrays with self-decorated nanoneedles serves as conductive backbone for growing redox active $NiMoO_4$ layer with high electrochemical activity on its surface. The coating of carbon protection shell can not only increase the overall electric conductivity of the composite but also improve its cycling stability via buffering the volume change during the charge/discharge processes. The obtained NiCoMn-O@$NiMoO_4$@C electrode can provide a maximum specific capacitance of 2189.5 F/g (at 0.25 A/g) and 81.6 % of its initial specific capacitance can be maintained after 1500 cycles GCD tests (at 6 A/g). To further verify its potential as electrode material in hybrid supercapacitors, a testing cell with NiCoMn-O@$NiMoO_4$@C as positive battery-type electrode and activated carbon (AC) as negative EDLC-type electrode and 3M KOH aqueous solution as electrolyte is made. The prepared NiCoMn-O@$NiMoO_4$@C//AC hybrid supercapacitor exhibits the maximum energy density of 59.9 Wh/kg (at 0.25 A/g) and its specific capacitance can maintain 88.3 % of its initial value after 3000 cycles GCD tests (at 6 A/g).

5.3 Methods

5.3.1 Materials

Carbon cloth (ELAT® hydrophilic plain-cloth, FuelCellsEtc, area density: 13 mg/cm^2), cobalt chloride hexahydrate ($CoCl_2 \cdot 6H_2O$, Sigma-Aldrich Corporation, formula weight: 237.93

g/mol), nickel nitrate hexahydrate ($Ni(NO_3)_2 \cdot 6H_2O$, Fisher Chemical, formula weight: 290.79 g/mol), manganese acetate tetrahydrate ($((CH_3CO_2)_2Mn \cdot 4H_2O$, Sigma-Aldrich Corporation, formula weight: 245.09 g/mol), ammonium fluoride (NH_4F, Sigma-Aldrich Corporation, formula weight: 37.04 g/mol), urea (CH_4N_2O, 60.06 g/mol, 0.601 g), sodium molybdate dihydrate ($Na_2MoO_4 \cdot 2H_2O$, Fisher Chemical, formula weight: 241.95 g/mol), D-(+)-glucose ($C_6H_{12}O_6$, Sigma-Aldrich Corporation, formula weight: 180.16 g/mol), deionized water, nickel foam (Surface density: 34.6 mg/cm^2, MTI Corporation), activated carbon (BET surface area: 1666 ($\pm$100) m^2/g, MTI Corporation), carbon black(MTI Corporation) and polytetrafluoroethylene (PTFE, 60 wt % dispersion in H_2O, Sigma-Aldrich Corporation). All chemical reagents are in analytical grade and used as received.

5.3.2 Synthesis of Venus flytrap-like hierarchical NiCoMn-O@$NiMoO_4$@C core shell nanosheet arrays

5.3.2.1 Synthesis of NiCoMn-O

Hierarchical NiCoMn-O nanosheet arrays with self-decorated nanoneedles on carbon cloth substrate is synthesized through a one-step hydrothermal method. Firstly, a piece of carbon cloth (4 cm × 4 cm), which used as the conductive substrate, is cleaned with ethanol and deionized water with the assistance of ultrasonication for 10 mins, respectively. Next, it is vertically placed in a 100 mL Teflon-lined stainless steel autoclave which contains a pink homogeneous solution made of 1 mmol $CoCl_2 \cdot 6H_2O$, 1 mmol $Ni(NO_3)_2 \cdot 6H_2O$, 1 mmol $(CH_3CO_2)_2Mn \cdot 4H_2O$, 5 mmol NH_4F and 10 mmol urea dissolved in 70 mL deionized water. Then, the autoclave is heated up to 120 ^oC (at a heating rate of 3 ^oC/min) in a box oven and its temperature is maintained for 6 h. After cooling to the room temperature, the obtained sample is sonicated in deionized water for 10 s and rinsed with ethanol for several times in order to remove the residue and loosely attached products. Afterwards, the sample is dried in a vacuum oven at

60 ºC for 1h to obtained NiCoMn-precursor. Then, it is annealed at 300ºC (2 ºC/min) for 2h in a tube furnace under Argon atmosphere. Finally, NiCoMn-based trimetallic oxides (NiCoMn-O) nanosheet arrays with self-decorated nanoneedles (which have similar shape of Venus flytrap) on carbon cloth substrate is obtained (as shown in figure 5.1a, b and e). For comparison purpose, the single-metal oxides and bi-metallic oxides based on Ni, Co and Mn elements (i.e. Ni-O, Co-O, Mn-O, NiCo-O, NiMn-O and CoMn-O) are also prepared at the sample conditions and, based on figure S5.1, NiCoMn-O can exhibit the best electrochemical performance. More detailed descriptions can be found in supplementary material.

5.3.2.2 Synthesis of $NiMoO_4$ layer

$NiMoO_4$ layer is synthesized by following the reported method with some modifications in order to achieve the best electrochemical performance.[26] In detail, the obtained NiCoMn-O sample is immersed in a 50 mL Teflon-lined stainless steel autoclave which has 40 mL solution made of 1 mmol $Na_2MoO_4 \cdot 2H_2O$ and 1 mmol $Ni(NO_3)_2 \cdot 6H_2O$ dissolved in deionized water. Then, the autoclave is heated up to 80ºC (2 ºC/min) and kept warm for 4h. After cooling to room temperature, the sample is rinsed with deionized water and dried at 60 ºC for 1h. After annealing at 400 ºC (2 ºC/min) for 2h under Argon atmosphere, the sample named as NiCoMn-O@$NiMoO_4$ is obtained. For comparison purpose, NiCoMn-O@$NiMoO_4$ samples synthesized from different experimental conditions with different morphologies are also prepared. More detailed information can be found in figure S5.2 and S5.3 in supplementary material.

5.3.2.3 Synthesis of carbon protection shell

For preparing the carbon protection shell on NiCoMn-O@$NiMoO_4$, the sample is immersed in the 0.15 M glucose aqueous solution for 12h; it is then annealed at 400 ºC (2 ºC/min) for 2h under Argon atmosphere. Eventually, the sample named as NiCoMn-

O@NiMoO$_4$@C is obtained and the measured mass loading of NiCoMn-O@NiMoO$_4$@C on carbon cloth substrate is about 1.6 mg/cm^2.

5.3.3 Fabrication of NiCoMn-O@NiMoO$_4$@C//AC hybrid supercapacitor

A hybrid supercapacitor is assembled by using NiCoMn-O@NiMoO$_4$@C on carbon cloth substrate as positive electrode and AC (which mixed with carbon black and PTFE with a weight ratio of 85 : 10 : 5) coated on nickel foam substrate as negative electrode. To achieve the maximum voltage window and energy density, the mass ratio between the positive and negative electrodes can be decided by the charge balance theory.[27, 28, 29] As shown in equation (1), the charge (Q) stored in each electrode replies on the mass of active material (m), specific capacitance (C_{sp}) and potential window (ΔV).

$$Q = m \times C_{sp} \times \Delta V \qquad (1)$$

In order to achieve the charge balance between positive and negative electrodes (which is $Q^+ = Q^-$), the mass ratio follows the rules of equation (2).

$$\frac{m^+}{m^-} = \frac{C_{sp}^- \times \Delta V^-}{C_{sp}^+ \times \Delta V^+} \qquad (2)$$

As a result, the optimum mass ratio between the positive electrode (NiCoMn-O@NiMoO$_4$@C) and negative electrode (AC) is calculated to be $m^+/m^- = 1/4.6$ (based on the discharge specific capacitances of both electrodes measured at the current density of 0.25 A/g).

5.3.4 Calculation equations

The specific capacitance ($C_{sp,CV}$, F/g) calculated from cyclic voltammetry (CV), energy density (E, Wh/kg), discharge specific capacitance ($C_{sp,GCD}$, F/g), power density (P, W/kg) and coulombic efficiency (η) of the hybrid supercapacitor can be calculated by equation (3), (4), (5), (6) and (7), respectively.[16]

$$C_{sp,CV} = [\int_{V_1}^{V_2} IdV\ /2vm(V_2 - V_1)] \times 10^6 \quad (3)$$

$$E = I \int V\ dt \times 1000/3600 \quad (4)$$

$$C_{sp,GCD} = 2E/(V_{discharge}^2 \times 3.6) \quad (5)$$

$$P = E/t_{discharge} \quad (6)$$

$$\eta = t_{discharge}/t_{charge} \times 100\% \quad (7)$$

Where I (A/g) is current density, V (V) is the potential or voltage from the discharge curves of the galvanostatic charge and discharge (GCD) tests, t (s) is time, $V_{discharge}$ (V) is the discharge potential or voltage excluding IR drop, $t_{discharge}$ (s) is the time of discharge process and t_{charge} (s) is the time of charge process.

The kinetics of the electrode reactions can be determined by investigating the relations between peak current (from CV curves) and the corresponding scan rates as shown in equation (8). Equation (9) is obtained by a log-transformation from equation (8).

$$i_p = av^b \quad (8)$$

$$\log(i_p) = b \times \log(v) + \log(a) \quad (9)$$

Where i_p is the peak current (A) , v is the scan rate (mV/s), and both a and b are the adjustable parameters that can be determined by linear fit calculation of $\log(i_p)$ versus $\log(v)$. Based on the calculated b value, it has two well-defined conditions. If b equals to 0.5, the electrode reaction is a diffusion-controlled process (battery-type electrode material). Whereas, if b equals to 1, the electrode reaction is a surface-controlled process (capacitive electrode material).[30, 31]

5.3.5 Characterization

Scanning electron microscopy (SEM) images were obtained via a FEI Quanta 250 FEG scanning electron microscope (FEI). High-resolution transmission electron microscopy (HRTEM) images and the corresponding energy dispersive spectroscopy (EDS) elemental mapping images were recorded from a FEI Titan Themis (AC-TEM) system. X-ray diffraction (XRD) spectrums were measured by a Rigaku XRD SmartLab. X-ray photoelectron spectroscopies (XPS) were detected in a Kratos Amicus X-ray Photoelectron Spectrometer (Kratos, Japan). Cyclic voltammetry (CV), galvanostatic charge and discharge (GCD) profiles were measured by a Gamry Reference 3000 Electrochemical Station. The reference electrode used in the electrochemical tests is a saturated calomel electrode (SCE, immersed in 1 M KOH).

5.4 Results and discussion

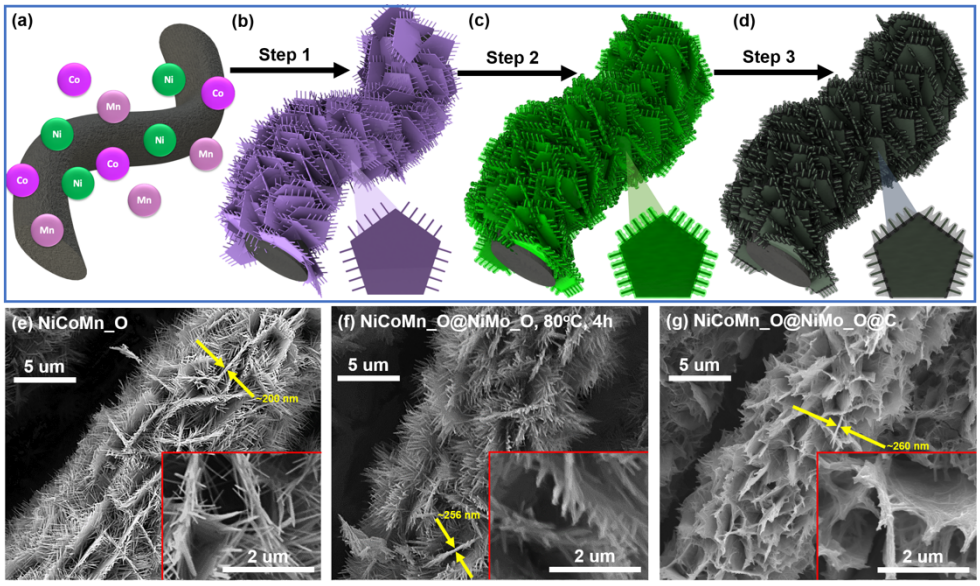

Figure 5.1. (a-d) Schematics of carbon cloth fiber, NiCoMn-O, NiCoMn-O@$NiMoO_4$ and NiCoMn-O@ $NiMoO_4$@C. (e) SEM image of NiCoMn-O with the magnification of 5000 x (scale bar: 5 um). The inset gives corresponding SEM image with higher magnification (15000 x, scale bar: 2um). (f) SEM image of NiCoMn-O@$NiMoO_4$ with the magnification of 5000 x (scale bar: 5 um). The inset gives corresponding SEM image with higher magnification (15000 x, scale bar: 2um). (g) SEM image of NiCoMn-O@$NiMoO_4$@C with the magnification of 5000 x (scale bar: 5 um). The inset gives corresponding SEM image with higher magnification (15000 x, scale bar: 2um).

The schematic illustrations of the material synthesis process is displayed in figure 5.1a-d and the corresponding SEM images of the two mid-products (NiCoMn-O and NiCoMn-O@$NiMoO_4$) and the final product (NiCoMn-O@$NiMoO_4$@C) are shown in figure 5.1e-g in order to investigate the morphology changes during the synthesis processes. According to figure 5.1a and b (step 1), it can be observed that the morphology of the NiCoMn-O (as the first mid-product) is the Venus flytrap-like nanosheet arrays with self-decorated nanoneedles. The nanoneedles can help achieve extra electroactive surface area which makes it more accessible to the electrolyte.[10] The thickness of the nanosheets is about 200 nm. At the step 2, a thin layer of NiMo-O is synthesized on the surface of NiCoMn-O (at the hydrothermal temperature of 80 ^oC for 4 h) which can be reflected by the increased surface roughness on the nanosheet and nanoneedles shown in the enlarged image of figure 5.1f. Besides, the SEM images of NiMo-O layer synthesized at other hydrothermal conditions are displayed in figure S5.2 (The images with higher magnification is also shown in figure S3). Theoretically, the higher hydrothermal temperature and longer holding time are able to help achieve thicker $NiMoO_4$ layer, but it will be perfect if its thickness can be controlled in a suitable value which can not only provide enough electroactive material but also ensure the unobstructed ion/electron transport in such core-shell structural material.[32, 33] In detail, when the hydrothermal temperature is 80 ^oC, although the thickness change cannot be obviously distinguished from the SEM images of NiCoMn-O@$NiMoO_4$ samples obtained from different holding time (i.e. 2 h, 4 h and 6 h) shown in figure S5.2c-e and figure S5.3c-e, the increment of mass loading (which is from 1.56 to 1.88 mg/cm^2) and the rise of surface roughness can prove the generation of new $NiMoO_4$ material layers. Based on the CV curves and discharge specific capacitances shown in figure S5.4a and b, NiCoMn-O@$NiMoO_4$ sample synthesized via hydrothermal method at 80 ^oC for 4h presents the

largest CV area (at 10 mV/s) and the highest specific capacitances (at all current densities), respectively. Moreover, when the holding time is 4 h and the temperature is varied (i.e. 80 °C, 100 °C, 120 °C), the rise of the thickness of $NiMoO_4$ layer can be easily observed from figure S5.2d, f, g and figure S5.3d, f, g. Furthermore, the corresponding CV curves and discharge specific capacitances are plotted in figure S5.4c and d. Again, NiCoMn-O@NiMo-O sample synthesized via hydrothermal method at 80 °C for 4h exhibits the largest CV area (at 10 mV/s) and the best rate capability comparing with the results from other samples. The thickness of the nanosheets is about 256 nm (which demonstrating the thickness of $NiMoO_4$ layer on the nanosheet is about 56 nm). After step 3, the final product named as NiCoMn-O@$NiMoO_4$@C is displayed in figure 5.1d. It can be found that the Venus flytrap-like hierarchical NiCoMn-O@$NiMoO_4$ nanosheets with self-decorated nanoneedles are fully covered by the carbon protection shell which even helps connect the interspace among nanoneedles; and the thickness of the nanosheets is about 260 nm (so that the thickness of the carbon protection shell is about 4 nm). As a result, the integration and electric conductivity of the material can be improved.

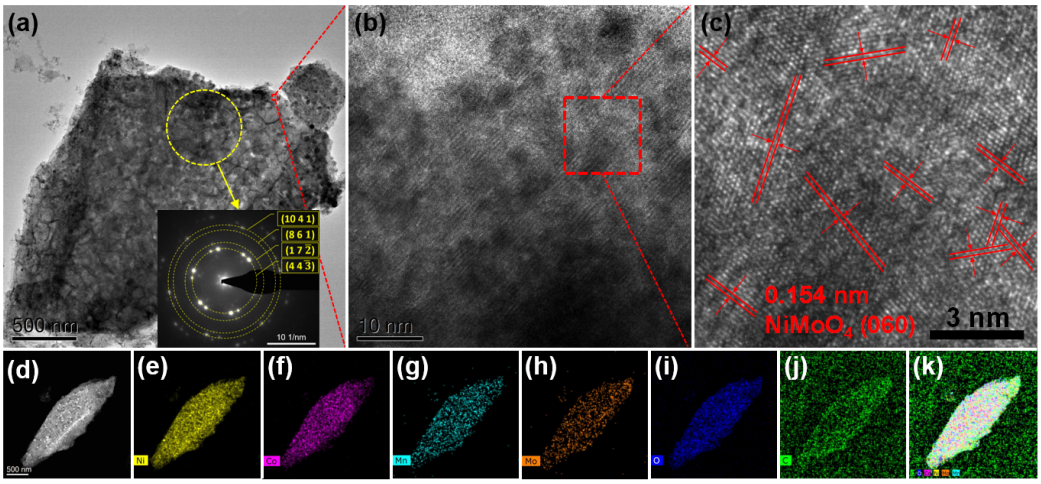

Figure 5.2. NiCoMn-O@$NiMoO_4$@C sample: (a) STEM image with the inset showing the SAED pattern of the selected area and (b-c) the corresponding HRTEM image. (c) Dark-field TEM image, (d-i) EDS elemental mapping of Ni, Co, Mn, Mo, O and C elements and (j) the superimposed image of all elements.

Figure 5.2a shows the STEM image of the nanosheet from NiCoMn-O@$NiMoO_4$@C sample (It can be noticed that the nanosheet is not as complete as the one shown in SEM images because of the ultrasonication step during the sample preparation processes for TEM test). The selected area electron diffraction (SAED) pattern shown in the inset gives a series of diffraction rings representing the planes of (4 4 $\bar{3}$), (1 7 $\bar{2}$), (8 6 1) and (10 4 1) for $NiMoO_4$. The high-resolution TEM image (HRTEM) in figure 5.2b and c gives the enlarged images of the selected area. As displayed in figure 5.2c, the HRTEM of the sample reveals that the interplanar spacing is 0.154 nm, which corresponds to the (060) crystal plane of $NiMoO_4$ (JCPDS#45-0142), suggesting the generation of $NiMoO_4$ layer. Even though the crystal structure of NiCoMn-O, which is hidden underneath the $NiMoO_4$ layer, cannot be observed, its crystal information will be measured via XRD in the later section. Moreover, the EDS elemental mapping from the sampling area which is indicated in the dark-field TEM image (figure 5.2d) was used to investigate the distribution of elements in the nanosheet from NiCoMn-O@$NiMoO_4$@C sample. According to figure 5.2e-i, it can be found that Ni, Co, Mn, Mo and O elements are uniformly distributed over the sampling area. In figure 5.2j, although the C signal can be detected from not only the sampling area but also the dark-field background part, the profile of the sampling area can be clearly discerned by the C signal (originated from the sampling area), suggesting the existence of carbon protection shell (which is derived from the glucose). In addition, figure 5.2k shows the superimposition of all detected elements on top of the dark-field TEM image, indicating the overall distribution of all related elements. The EDS spectrum shown in figure S5.5 also confirms the existence of Ni, Co, Mn, Mo, O and C elements.

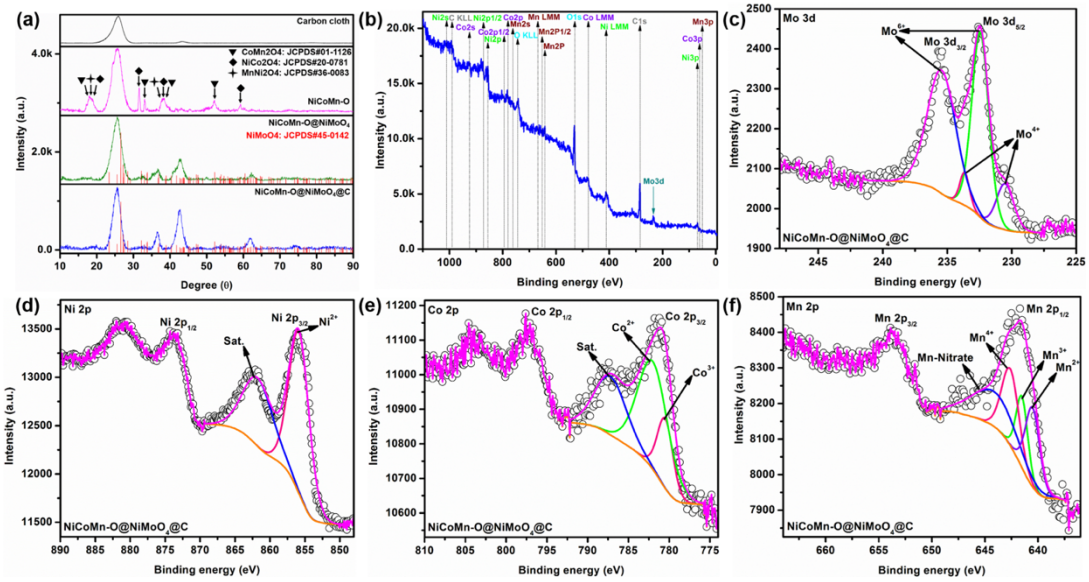

Figure 5.3. (a) XRD patterns of NiCoMn-O, NiCoMn-O@$NiMoO_4$ and NiCoMn-O@$NiMoO_4$@C samples. (b) XPS spectrum of NiCoMn-O@$NiMoO_4$@C sample. (c) Mo 3d core-level XPS spectrum of NiCoMn-O@$NiMoO_4$@C at the pristine state. (d) Ni 2p core-level XPS spectrum of NiCoMn-O@$NiMoO_4$@C. (e) Co 2p core-level XPS spectrum of NiCoMn-O@$NiMoO_4$@C. (f) Mn 2p core-level XPS spectrum of NiCoMn-O@$NiMoO_4$@C.

The structural change during the synthesis of hierarchical NiCoMn-O@$NiMoO_4$@C is detected by XRD as shown in figure 5.3a. It can be observed that the XRD of carbon cloth (in black color) is able to exhibit two peaks located at 26 ° and 43.5 ° which can be attributed to (0 0 2) and (1 0 1) planes of carbon material, respectively.[34] Then, the XRD of NiCoMn-O (in pink color) gives a complex pattern which can be ascribed to the combination of patterns from $CoMn_2O_4$ (JCPDS#01-1126), $NiCo_2O_4$ (JCPDS#20-0781) and $MnNi_2O_4$ (JCPDS#36-0083). In detail, the peak at around 18 ° can be devolved into three peaks which are the peak at 18.277 ° from $CoMn_2O_4$, the peak at 18.906 ° from (1 1 1) plane of $NiCo_2O_4$ and the peak at 18.430 ° from (1 1 1) plane of $MnNi_2O_4$, respectively. Similarly, the peak at around 38 ° can also be treated as a mixture of three peaks (i.e. 38.957 ° from $CoMn_2O_4$, 38.404 ° from (2 2 2) plane of $NiCo_2O_4$ and 37.376 ° from (2 2 2) plane of $MnNi_2O_4$). Moreover, the peaks located at 33 ° and 52 ° are the signals from $CoMn_2O_4$ and the peaks at 31 ° and 59 ° can be indexed to (2 2 0) and (5

1 1) planes of $NiCo_2O_4$. However, it is necessary to clarify that the obtained XRD pattern of NiCoMn-O cannot be perfectly matched by any of the above mentioned XRD characteristic peaks of bimetallic oxides (i.e. $CoMn_2O_4$, $NiCo_2O_4$ and $MnNi_2O_4$) or those single metal oxides (such as NiO, MnO_2 and Co_3O_4 etc.), indicating NiCoMn-O is highly possibly consisted of the combination of $CoMn_2O_4$, $NiCo_2O_4$ and $MnNi_2O_4$. In terms of NiCoMn-O@$NiMoO_4$ (in green color) and NiCoMn-O@$NiMoO_4$@C (in brown color), the measured XRD patterns are similar to each other since the only difference between these two samples is whether the carbon protection shell is coated or not which cannot be easily differentiated by XRD testing. Comparing with the XRD pattern of NiCoMn-O, the XRD patterns of NiCoMn-O@$NiMoO_4$ or NiCoMn-O@$NiMoO_4$@C are totally different, suggesting a new phase has grown on the surface of NiCoMn-O, and these diffraction peaks can be attributed to $NiMoO_4$ (JCPDS#45-1042). For example, the peak at 32.2 ° and 32.9 ° (from the pattern) can be indexed to (1 1 2) and (0 2 -2) planes of $NiMoO_4$. The big peak at 36.6 ° (from the pattern) can be devolved into two standard diffraction peaks of $NiMoO_4$ (JCPDS#45-1042), which are located at 36.707 ° for (2 0 2) plane and 36.905 ° for (4 0 0) plane. Similarly, the big peaks at 42.6 ° and 61.9 ° along with a small hump centered at 74.1° can also be ascribed to the combination of a series of standard diffraction peaks of $NiMoO_4$ (JCPDS#45-1042).

The surface chemical compositions and valence states of Mo, Ni, Co and Mn elements are detected by the XPS. In figure 5.3b, the XPS full scan spectrums of NiCoMn-O@$NiMoO_4$@C are displayed. Generally, this XPS spectrum can also help confirm the presence of Ni, Co, Mn, Mo, C and O elements in the obtained NiCoMn-O@$NiMoO_4$@C sample; and it is obvious that the peak, representing C signal, comes from the carbon fiber and the carbon protection shell. In terms of the core-level XPS spectrums, as shown in figure 5.3c, Mo 3d core-

level XPS spectrum reveals the presence of large amount of Mo^{6+} (located at 232.43 eV and 235.43 eV), suggesting the existence of $NiMoO_4$ layer, and a little bit of Mo^{4+} (located at 230.51 eV and 233.65 eV).[35] Besides, the Ni 2p core-level XPS spectrum displayed in figure 5.3d can be fitted by one spin-orbit doublet (at 855.83 eV) and one shakeup satellite peak (861.73 eV), suggesting the majority of Ni element has the valence state of Ni^{2+} which corresponds to the Ni^{2+} in $NiMoO_4$, $NiCo_2O_4$ and $MnNi_2O_4$.[36, 37] Moreover, the Co 2p core-level XPS spectrum shown in figure 5.3e indicates the co-existence of Co^{3+} (at 780.49 eV), which is related to the Co^{3+} in $NiCo_2O_4$, and Co^{2+} (781.99 eV), which may be originated from the Co^{2+} in $CoMn_2O_4$; and a satellite peak can be found at 787.19 eV.[38] Furthermore, in figure 5.3f, the Mn 2p core-level XPS spectrum reveals the fact that Mn element has different valences states in the material, including Mn^{2+} (at 640.51 eV), Mn^{3+} (at 641.51 eV) which may be from $CoMn_2O_4$, Mn^{4+} (at 642.61 eV) which may be from $MnNi_2O_4$ and Mn-nitrate (at 644.11 eV).[39, 40]

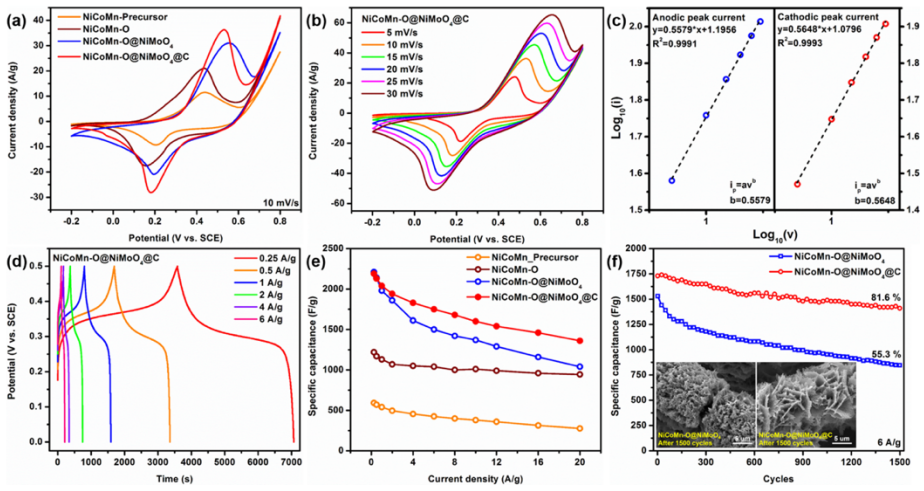

Figure 5.4. (a) CV curves of NiCoMn-precursor, NiCoM-O, NiCoMn-O@$NiMoO_4$ and NiCoMn-O@$NiMoO_4$@C at the scan rate of 10 mV/s. (b) CV curves of NiCoMn-O@$NiMoO_4$@C at different scan rates and (c) the corresponding linear fit of $\log(i_p)$ versus $\log(v)$ at cathodic and anodic peaks. (d) GCD curves of NiCoMnO@NiMnO4@C at different current densities and (e) the corresponding specific capacitances and coulombic efficiencies of NiCoMn-precursor, NiCoMn-O, NiCoMn-O@ $NiMoO_4$ and NiCoMnO@$NiMoO_4$@C calculated from the discharge GCD curves. (f) Capacitance retention of NiCoMnO@$NiMoO_4$ and NiCoMnO@ $NiMoO_4$@C

after 1500 GCD cycles. The inset gives the corresponding morphology change after the cycling test.

In figure 5.4a, for comparison purposes, the cyclic voltammetry (CV) curves of NiCoMn-precursor, NiCoM-O, NiCoMn-O@$NiMoO_4$ and NiCoMn-O@$NiMoO_4$@C (at the scan rate of 10 mV/s) are plotted together. It can be noticed that, from NiCoMn-precursor to NiCoMn-O@$NiMoO_4$@C, the peak currents of these samples increase gradually; and NiCoMn-O@$NiMoO_4$@C has the highest peak currents, revealing that NiCoMn-O@$NiMoO_4$@C has the best electrical conductivity and electrochemical activity among the products listed above. The reason of this phenomenon will be released in the later part of this paragraph. Besides, the specific capacitances calculated from these CV curves (displayed in the figure S5.6) shows that NiCoMn-O@$NiMoO_4$@C provides a value of 706.4 F/g which is higher than that of other samples (i.e. 671.5 F/g for NiCoMn-O@$NiMoO_4$, 503.2 F/g for NiCoMn-O and 266.4 F/g for NiCoMn-precursor). Based on these results, three conclusions can be addressed: 1. The incorpoartion of $NiMoO_4$ layer on top of NiCoMn-O can dramatically improve the electrochemical performance. 2. The addition of carbon protection shell on the surface of NiCoMn-O@$NiMoO_4$ can slightly boost the value of specific capacitance. 3. The annealing process that transfers NiCoMn-precursor to NiCoMn-O can actually help enhance the electrochemical performance. Figure 5.4b gives the CV curves of NiCoMn-O@$NiMoO_4$@C at different scan rates. As the increase of scan rates from 5 to 30 mV/s, the anodic peak shifts towards the positive side and the cathodic peak shifts towards the negative side, respectively, due to the polarization of the electrode. The obvious peak separation suggests that NiCoMn-O@$NiMoO_4$@C can be classified as one kind of battery-type electrode materials. To investigate the kinetics of the reactions, the linear fit of $\log(i_p)$ versus $\log(v)$ is also provided in figure 5.4c. According to equation (9), the b values from both anodic (b = 0.5579) and cathodic peak

currents (b = 0.5648) are close to 0.5, further confirming that the obtained NiCoMn-O@$NiMoO_4$@C is one kind of diffusion-controlled battery-type electrode materials. The involved redox reactions can be described as follows:[41]

$$NiMoO_4 \leftrightarrow Ni^{2+} + MoO_4^{2-} \quad (10)$$

$$Ni^{2+} + 2OH^- \leftrightarrow Ni(OH)_2 \quad (11)$$

$$Ni(OH)_2 + OH^- \leftrightarrow NiOOH + H_2O + e^- \quad (12)$$

Moreover, the GCD curves of NiCoMn-O@$NiMoO_4$@C at different current densities is displayed in figure 5.4d and the obvious plateaus, which represent the redox reactions of electrode material, can be observed from both charge and discharge curves. The corresponding calculated results shown in figure 5.4e indicates that NiCoMn-O@$NiMoO_4$@C electrode material has the maximum specific capacitance of 2189.5 F/g at the current density of 0.25 A/g; and, when the applied current density increases to 20 A/g, a high specific capacitance of 1361.1 F/g (which is about 62.2% of the maximum value) can still be obtained, suggesting its high rate capability. In addition, the specific capacitances of NiCoMn-precursor ,NiCoMn-O and NiCoMn-O@$NiMoO_4$ are also measured and plotted in figure 5.4e. It can be observed that the specific capacitances of NiCoMn-O@$NiMoO_4$@C are overall larger than those of other electrode materials and, comparing with NiCoMn-O@$NiMoO_4$, NiCoMn-O@$NiMoO_4$@C has higher rate capability which is most likely benefited by the increased electric conductivity owing to the incorporation of carbon protection shell on the material surface.[42, 43] Furthermore, after 1500-cycle GCD tests (figure 5.4f), NiCoMn-O@$NiMoO_4$@C and NiCoMn-O@$NiMoO_4$ can maintain 81.6 % and 55.3 % of their initial specific capacitances, respectively. This difference in electrochemical durability can be explained by the SEM images of NiCoMn-O@$NiMoO_4$@C and NiCoMn-O@$NiMoO_4$ after 1500-cycle GCD tests as illustrated in the inset. It can be

observed that the surface structure of NiCoMn-O@$NiMoO_4$ are fragile because of the volume change caused by the structural deformation during the redox reactions, resulting in rapid structural destruction. The coating of carbon protection shell (on NiCoMn-O@$NiMoO_4$ to generate NiCoMn-O@$NiMoO_4$@C) can help maintain the integration of surface structure through buffering the volume change during the redox reactions and, thus, the electrochemical durability of electrode material can be enhanced.[44, 45] In sum, comparing with other products, NiCoMn-O@$NiMoO_4$@C exhibits the best electrical conductivity and electrochemical activity owing to the synergistic effect of novel nanostructure (which is the self-decorated nanoneedles on the surface of nanosheet arrays for exposing more electroactive surface area and shorten the ion transfer path), combination of mixed-metallic oxides (which is growing $NiMoO_4$ layer with high electrochemical activity on the surface of NiCoMn-O with better electrical conductivity) and incorporation of conductive carbon material (which is carbon protection shell for boosting the electrical conductivity and cycling stability of the composite).

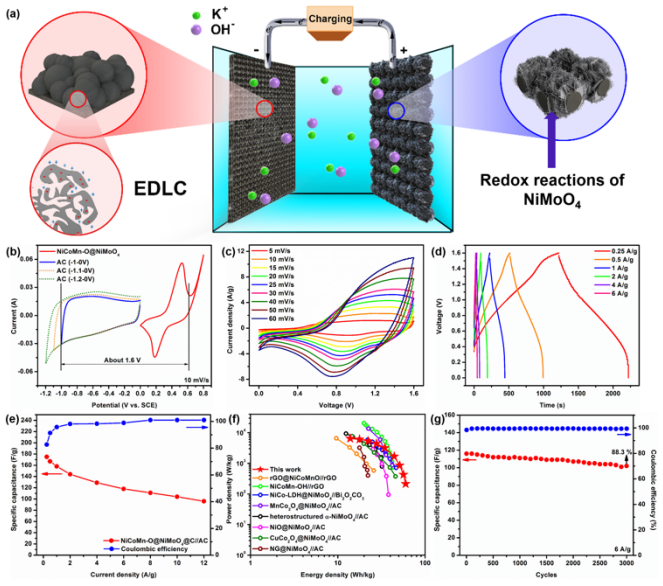

Figure 5.5. (a) (b) CV curves of positive and negative electrodes at the scan rate of 10 mV/s. (c) CV curves of NiCoMn-O@$NiMoO_4$@C//AC at different scan rates. (d) GCD curves of NiCoMn-O@$NiMoO_4$@C//AC at different current densities and (e) the corresponding specific capacitances

and coulombic efficiencies calculated from the discharge GCD curves. (f) Ragone plot of NiCoMn-O@$NiMoO_4$@C//AC (and other reported works). [12, 13, 26, 46, 47, 48, 49, 50] (g) GCD cyclic performance of NiCoMn-O@$NiMoO_4$@C//AC at the current density of 6 A/g.

To evaluate the performance of NiCoMn-O@$NiMoO_4$@C electrode material in a complete capacitor cell, a hybrid supercapacitor (named as NiCoMn-O@$NiMoO_4$@C//AC) is assembled by using NiCoMn-O@$NiMoO_4$@C as positive electrode and AC as negative electrode (figure 5.5a and figure S5.7). The electrolyte is 3 M KOH aqueous solution. According to figure 5.5b, the maximum working voltage of NiCoMn-O@$NiMoO_4$@C//AC hybrid supercapacitor can be estimated by measuring CV curves of positive and negative electrodes in the three-electrode setup at the same scan rate (for example, 10 mV/s), respectively. In terms of NiCoMn-O@$NiMoO_4$@C positive electrode, the oxygen evolution reaction occurs when the potential moves beyond 0.6 V (vs. SCE). With regard to AC negative electrode, hydrogen evolution happens when the potential drops lower than -1 V (vs. SCE). Therefore, the estimated maximum voltage of the cell is about 1.6 V. Besides, the CV curves of NiCoMn-O@$NiMoO_4$@C//AC hybrid supercapacitor at different scan rates are illustrated in figure 5.5c and the shape of these curves are not square but exhibit peaks caused by the redox reactions of the positive electrode, representing the characteristic behavior of hybrid supercapacitor. Moreover, the GCD curves of NiCoMn-O@$NiMoO_4$@C//AC hybrid supercapacitor with a voltage window of 1.6 V at different current densities are displayed in figure 5.5d. It is necessary to mention that there are about 5 steps in a typical GCD curve (of NiCoMn-O@$NiMoO_4$@C//AC hybrid supercapacitor) and each step can be interpreted by a comprehensive analysis of CV and GCD curves shown in figure S5.8. During the charge process of GCD curve in figure S5.8a, the voltage of the cell jumps from 0 to 0.35V instantly within 1 second (step 1) which is because that , according to the CV in the figure S5.8b, there is no redox reaction in the voltage range of 0 to

0.4 V and, thus, a very fast charge speed can be achieved. In step 2, the voltage of the cell gradually increases to about 1.5 V (figure S5.8a), which corresponds to the large hump of the CV (as shown in figure 5.4b) originated by the redox reactions of the positive electrode. When the voltage exceeds 1.5 V (step 3), it can be observed that the charging rate further slows down because of the slight occurrence of water decomposition. This explanation can be confirmed by the step 3 (where a tiny increase of current density around 1.6 V indicating water decomposition can be observed) marked in the CV curve as displayed in figure S5.8b. The discharge process (including step 4 and step 5) is just the reversal action of charge process excluding the water decomposition phenomenon. The profile of GCD curves at other current densities basically follow the similar pattern. Furthermore, the corresponding calculated specific capacitances and coulombic efficiencies are displayed in figure 5.5e. In detail, the specific capacitance of the supercapacitor is 175 F/g (with the coulombic efficiency of 82.7 %) at the current density of 0.25 A/g and the value is changed to 96.1 F/g (with the coulombic efficiency of 100 %) when the current density is 12 A/g. In addition, the energy densities and power densities calculated from the GCD curves of NiCoMn-O@$NiMoO_4$@C//AC hybrid supercapacitor are illustrated in the Ragone plot shown in figure 5.5f. It can be found that the prepared NiCoMn-O@$NiMoO_4$@C//AC hybrid supercapacitor can deliver a maximum energy density of 59.9 Wh/kg (with a power density of 214.1 W/kg) at the current density of 0.25 A/g and a maximum power density of 6467.9 W/kg (with an energy density of 13.9 Wh/kg) at 12 A/g. Comparing with the recent published works (about NiCoMn-based trimetallic oxides or $NiMoO_4$ based supercapacitors), the prepared NiCoMn-O@$NiMoO_4$@C//AC hybrid supercapacitor has the slight advantage in energy densities and their power densities are at the same level. [13, 12, 46, 26, 47, 48, 49, 50] The cyclic performance of NiCoMn-O@$NiMoO_4$@C//AC hybrid supercapacitor is

investigated in figure 5.5g and 88.3 % of its initial specific capacitance can be retained after 3000 cycles of GCD tests at a current density of 6 A/g. The corresponding coulombic efficiencies are stabilized around 99.4%, reflecting the good stability of the cell.

5.5 Conclusion

In this work, a Venus fly-trap like hierarchical NiCoMn-O@$NiMoO_4$@C nanosheet arrays electrode is designed and successfully synthesized via a multi-step hydrothermal method. The prepared NiCoMn-O nanosheet is used as conductive backbone (since its electrical conductivity is better than any of its bimetallic or monometallic counterparts) for growing $NiMoO_4$ and carbon protection shell and the self-decorated nanoneedles on its surface can create more electroactive surface area for electrolyte to access (i.e. The ion transport path is shortened). $NiMoO_4$ layer is the most important redox active material in this composite since its high electrochemical activity in alkaline solution. The incorporation of carbon protection shell (which is derived from glucose) cannot only increase the overall electric conductivity of the composite but also improve its cycling stability via buffering the volume change during the charge/discharge processes. As a result, with the synergistic effect of these components, NiCoMn-O@$NiMoO_4$@C can provide the highest specific capacitance of 2189.5 F/g at 0.25 A/g and a high specific capacitance value of 1361.1 F/g can still be obtained at 20 A/g, suggesting its good rate capability. Besides, during 1500 cycles GCD tests, , about 81.6 % of NiCoMn-O@$NiMoO_4$@C's initial specific capacitance can be remained, while the specific capacitance of NiCoMn-O@$NiMoO_4$ exhibits a fast drop down to 55.3% of its initial value, revealing the good cycle stability of NiCoMn-O@$NiMoO_4$@C owing to the addition of carbon protection shell. Furthermore, our prepared NiCoMn-O@$NiMoO_4$@C//AC hybrid supercapacitor (with a voltage window of 1.6 V) can provide a maximum energy density of 59.9 Wh/kg (with a power density

of 214.1 W/kg) at 0.25 A/g and a maximum power density of 6467.9 W/kg (with an energy density of 13.9 Wh/kg) at 12 A/g. In addition, the cycling stability of NiCoMn-O@$NiMoO_4$@C//AC hybrid supercapacitor is tested and 88.3 % of its initial specific capacitance can be maintained after 3000 cycles GCD tests.

5.6 References

(1) Ellabban, O.; Abu-Rub, H.; Blaabjerg, F. Renewable Energy Resources: Current Status, Future Prospects and Their Enabling Technology. Renewable and Sustainable Energy Reviews, 2014, 39, 748–764.

(2) Abas, N.; Kalair, A.; Khan, N. Review of Fossil Fuels and Future Energy Technologies. Futures 2015, 69, 31–49.

(3) Zhao, B.; Chen, D.; Xiong, X.; Song, B.; Hu, R.; Zhang, Q.; Rainwater, B. H.; Waller, G. H.; Zhen, D.; Ding, Y.; et al. A High-Energy, Long Cycle-Life Hybrid Supercapacitor Based on Graphene Composite Electrodes. Energy Storage Mater. 2017, 7, 32–39.

(4) Muzaffar, A.; Ahamed, M. B.; Deshmukh, K.; Thirumalai, J. A Review on Recent Advances in Hybrid Supercapacitors: Design, Fabrication and Applications. Renewable and Sustainable Energy Reviews, 2019, 101, 123–145.

(5) Zuo, W.; Li, R.; Zhou, C.; Li, Y.; Xia, J.; Liu, J. Battery-Supercapacitor Hybrid Devices: Recent Progress and Future Prospects. Adv. Sci. 2017, 4, 1–21.

(6) He, D.; Xing, S.; Sun, B.; Cai, H.; Suo, H.; Zhao, C. Design and Construction of Three-Dimensional Flower-like CuO Hierarchical Nanostructures on Copper Foam for High Performance Supercapacitor. Electrochim. Acta 2016, 210, 639–645.

(7) He, D.; Liu, G.; Pang, A.; Jiang, Y.; Suo, H.; Zhao, C. A High-Performance Supercapacitor Electrode Based on Tremella-like NiC2O4@NiO Core/Shell Hierarchical Nanostructures on Nickel Foam. Dalt. Trans. 2017, 46, 1857–1863.

(8) Yan, J.; Li, S.; Lan, B.; Wu, Y.; Lee, P. S. Rational Design of Nanostructured Electrode Materials toward Multifunctional Supercapacitors. Advanced Functional Materials, 2020, 30, 1902564.

(9) Duraisamy, N.; Numan, A.; Fatin, S. O.; Ramesh, K.; Ramesh, S. Facile Sonochemical Synthesis of Nanostructured NiO with Different Particle Sizes and Its Electrochemical Properties for Supercapacitor Application. J. Colloid Interface Sci. 2016, 471, 136–144.

(10) Lin, L.; Liu, J.; Liu, T.; Hao, J.; Ji, K.; Sun, R.; Zeng, W.; Wang, Z. Growth-Controlled NiCo2S4 Nanosheet Arrays with Self-Decorated Nanoneedles for High-Performance Pseudocapacitors. J. Mater. Chem. A 2015, 3, 17652–17658.

(11) Hu, W.; Wei, H.; She, Y.; Tang, X.; Zhou, M.; Zang, Z.; Du, J.; Gao, C.; Guo, Y.; Bao, D. Flower-like Nickel-Zinc-Cobalt Mixed Metal Oxide Nanowire Arrays for Electrochemical Capacitor Applications. J. Alloys Compd. 2017, 708, 146–153.

(12) Chen, H. C.; Qin, Y.; Cao, H.; Song, X.; Huang, C.; Feng, H.; Zhao, X. S. Synthesis of Amorphous Nickel–Cobalt–Manganese Hydroxides for Supercapacitor-Battery Hybrid Energy Storage System. Energy Storage Mater. 2019, 17, 194–203.

(13) Sanchez, J. S.; Pendashteh, A.; Palma, J.; Anderson, M.; Marcilla, R. Porous NiCoMn Ternary Metal Oxide/Graphene Nanocomposites for High Performance Hybrid Energy Storage Devices. Electrochim. Acta 2018, 279, 44–56.

(14) Zhu, Y.; Huang, C.; Li, C.; Fan, M.; Shu, K.; Chen, H. C. Strong Synergetic Electrochemistry between Transition Metals of A Phase Ni−Co−Mn Hydroxide Contributed Superior Performance for Hybrid Supercapacitors. J. Power Sources 2019, 412, 559–567.

(15) Zhao, Y.; Li, X.; Yan, B.; Xiong, D.; Li, D.; Lawes, S.; Sun, X. L. Recent Developments and Understanding of Novel Mixed Transition-Metal Oxides as Anodes in Lithium Ion Batteries. Advanced Energy Materials, 2016, 6, 1502175.

(16) Tang, X.; Zhang, B.; Lui, Y. H.; Hu, S. Ni-Mn Bimetallic Oxide Nanosheets as High-Performance Electrode Materials for Asymmetric Supercapacitors. J. Energy Storage 2019, 25, 100897.

(17) Cai, D.; Liu, B.; Wang, D.; Liu, Y.; Wang, L.; Li, H.; Wang, Y.; Wang, C.; Li, Q.; Wang, T. Facile Hydrothermal Synthesis of Hierarchical Ultrathin Mesoporous NiMoO4 Nanosheets for High Performance Supercapacitors. Electrochim. Acta 2014, 115, 358–363.

(18) Zhi, M.; Xiang, C.; Li, J.; Li, M.; Wu, N. Nanostructured Carbon-Metal Oxide Composite Electrodes for Supercapacitors: A Review. Nanoscale 2013, 5, 72–88.

(19) Zhang, X.; Luo, J.; Tang, P.; Ye, X.; Peng, X.; Tang, H.; Sun, S. G.; Fransaer, J. A Universal Strategy for Metal Oxide Anchored and Binder-Free Carbon Matrix Electrode: A Supercapacitor Case with Superior Rate Performance and High Mass Loading. Nano Energy 2017, 31, 311–321.

(20) Nagaraju, G.; Sekhar, S. C.; Yu, J. S. Utilizing Waste Cable Wires for High-Performance Fiber-Based Hybrid Supercapacitors: An Effective Approach to Electronic-Waste Management. Adv. Energy Mater. 2018, 8, 1702201.

(21) Li, R.; Wang, Y.; Zhou, C.; Wang, C.; Ba, X.; Li, Y.; Huang, X.; Liu, J. Carbon-Stabilized High-Capacity Ferroferric Oxide Nanorod Array for Flexible Solid-State Alkaline Battery-Supercapacitor Hybrid Device with High Environmental Suitability. Adv. Funct. Mater. 2015, 25, 5384–5394.

(22) Ji, W.; Ji, J.; Cui, X.; Chen, J.; Liu, D.; Deng, H.; Fu, Q. Polypyrrole Encapsulation on Flower-like Porous NiO for Advanced High-Performance Supercapacitors. Chem. Commun. 2015, 51, 7669–7672.

(23) Huang, H.; Wang, X.; Tervoort, E.; Zeng, G.; Liu, T.; Chen, X.; Sologubenko, A.; Niederberger, M. Nano-Sized Structurally Disordered Metal Oxide Composite Aerogels as High-Power Anodes in Hybrid Supercapacitors. ACS Nano 2018, 12, 2753–2763.

(24) Fu, L.; Qu, Q.; Holze, R.; Kondratiev, V. V.; Wu, Y. Composites of Metal Oxides and Intrinsically Conducting Polymers as Supercapacitor Electrode Materials: The Best of Both Worlds? Journal of Materials Chemistry A, 2019, 7, 14937–14970.

(25) Qin, J.; Sari, H. M. K.; Wang, X.; Yang, H.; Zhang, J.; Li, X. Controlled Design of Metal Oxide-Based (Mn2+/Nb5+) Anodes for Superior Sodium-Ion Hybrid Supercapacitors: Synergistic Mechanisms of Hybrid Ion Storage. Nano Energy 2020, 71, 104594.

(26) Mehrez, J. A. A.; Owusu, K. A.; Chen, Q.; Li, L.; Hamwi, K.; Luo, W.; Mai, L. Hierarchical MnCo2O4@NiMoO4 as Free-Standing Core-Shell Nanowire Arrays with Synergistic Effect for Enhanced Supercapacitor Performance. Inorg. Chem. Front. 2019, 6, 857–865.

(27) Gu, J.; Sun, L.; Zhang, Y.; Zhang, Q.; Li, X.; Si, H.; Shi, Y.; Sun, C.; Gong, Y.; Zhang, Y. MOF-Derived Ni-Doped CoP@C Grown on CNTs for High-Performance Supercapacitors. Chem. Eng. J. 2020, 385, 123454.

(28) Liu, C.; Gao, A.; Yi, F.; Shu, D.; Yi, H.; Zhou, X.; Hao, J.; He, C.; Zhu, Z. Anchoring Ultrafine Co3O4 Grains on Reduced Oxide Graphene by Dual-Template Nanocasting Strategy for High-Energy Solid State Supercapacitor. Electrochim. Acta 2019, 326, 134965.

(29) Chen, S.; Zhang, M.; Ma, X.; Li, L.; Zhou, X.; Zhang, Z. Asymmetric Supercapacitors by Integrating High Content Na+/K+-Inserted MnO2 Nanosheets and Layered Ti3C2Tx Paper. Electrochim. Acta 2020, 332, 135497.

(30) Dong, X.; Chen, L.; Liu, J.; Haller, S.; Wang, Y.; Xia, Y. Environmentally-Friendly Aqueous Li (or Na)-Ion Battery with Fast Electrode Kinetics and Super-Long Life. Sci. Adv. 2016, 2, 1–9.

(31) Zhang, J.; Chen, H.; Sun, X.; Kang, X.; Zhang, Y.; Xu, C.; Zhang, Y. High Intercalation Pseudocapacitance of Free-Standing T-Nb 2 O 5 Nanowires@carbon Cloth Hybrid Supercapacitor Electrodes . J. Electrochem. Soc. 2017, 164, A820–A825.

(32) Zhang, H.; Lu, C.; Hou, H.; Ma, Y.; Yuan, S. Tuning the Electrochemical Performance of NiCo2O4@NiMoO4 Core-Shell Heterostructure by Controlling the Thickness of the NiMoO4 Shell. Chem. Eng. J. 2019, 370, 400–408.

(33) Jiang, H.; Zhao, T.; Li, C.; Ma, J. Hierarchical Self-Assembly of Ultrathin Nickel Hydroxide Nanoflakes for High-Performance Supercapacitors. J. Mater. Chem. 2011, 21, 3818–3823.

(34) Meng, S.; Hong, Y.; Dai, Z.; Huang, W.; Dong, X. Simultaneous Detection of Dihydroxybenzene Isomers with ZnO Nanorod/Carbon Cloth Electrodes. ACS Appl. Mater. Interfaces 2017, 9, 12453–12460.

(35) Castillo, C.; Buono-Core, G.; Manzur, C.; Yutronic, N.; Sierpe, R.; Cabello, G.; Chornik, B. Molybdenum Trioxide Thin Films Doped with Gold Nanoparticles Grown by a Sequential Methodology: Photochemical Metal-Organic Deposition (PMOD) and DC-Magnetron Sputtering. J. Chil. Chem. Soc. 2016, 61, 2816–2820.

(36) Biesinger, M. C.; Payne, B. P.; Grosvenor, A. P.; Lau, L. W. M.; Gerson, A. R.; Smart, R. S. C. Resolving Surface Chemical States in XPS Analysis of First Row Transition Metals, Oxides and Hydroxides: Cr, Mn, Fe, Co and Ni. Appl. Surf. Sci. 2011, 257, 2717–2730.

(37) Biesinger, M. C.; Payne, B. P.; Lau, L. W. M.; Gerson, A.; Smart, R. S. C. X-Ray Photoelectron Spectroscopic Chemical State Quantification of Mixed Nickel Metal, Oxide and Hydroxide Systems. Surf. Interface Anal. 2009, 41, 324–332.

(38) Cao, Z.; Liu, C.; Huang, Y.; Gao, Y.; Wang, Y.; Li, Z.; Yan, Y.; Zhang, M. Oxygen-Vacancy-Rich NiCo2O4 Nanoneedles Electrode with Poor Crystallinity for High Energy Density All-Solid-State Symmetric Supercapacitors. J. Power Sources 2020, 449, 227571.

(39) Guo, J.; Zhang, X.; Du, X.; Zhang, F. A Mn3O4 Nano-Wall Array Based Binder-Free Cathode for High Performance Lithium-Sulfur Batteries. J. Mater. Chem. A 2017, 5, 6447–6454.

(40) Wang, X.; Wu, W.; Chen, Z.; Wang, R. Bauxite-Supported Transition Metal Oxides: Promising Low-Temperature and SO2 -Tolerant Catalysts for Selective Catalytic Reduction of NOx. Sci. Rep. 2015, 5, 1–6.

(41) Feng, Y.; Liu, L.; Liang, J.; Yao, W.; Tian, B.; Jiang, C.; Wu, W. Ni(OH)2/NiMoO4 Nanoplates for Large-Scale Fully-Printed Flexible Solid-State Supercapacitors. J. Power Sources 2019, 433, 126676.

(42) Wolfenstine, J.; Lee, U.; Allen, J. L. Electrical Conductivity and Rate-Capability of Li4Ti 5O12 as a Function of Heat-Treatment Atmosphere. Journal of Power Sources, 2006, 154, 287–289.

(43) Mou, J.; Deng, Y.; Song, Z.; Zheng, Q.; Lam, K. H.; Lin, D. Excellent Rate Capability and Cycling Stability in Li+-Conductive Li2SnO3-Coated LiNi0.5Mn1.5O4 Cathode Materials for Lithium-Ion Batteries. Dalt. Trans. 2018, 47, 7020–7028.

(44) Li, R.; Wang, Y.; Zhou, C.; Wang, C.; Ba, X.; Li, Y. Carbon-Stabilized High-Capacity Ferroferric Oxide Nanorod Array for Flexible Solid-State Alkaline Battery – Supercapacitor Hybrid Device with High Environmental Suitability. 2015, 5384–5394.

(45) Bae, S. H.; Kim, J. E.; Randriamahazaka, H.; Moon, S. Y.; Park, J. Y.; Oh, I. K. Seamlessly Conductive 3D Nanoarchitecture of Core–Shell Ni-Co Nanowire Network for Highly Efficient Oxygen Evolution. Adv. Energy Mater. 2017, 7, 1601492.

(46) Kang, W.; Sun, Y.; Xu, B.; Li, J.; Kong, X.; Huang, D.; Zhang, X.; Yang, H.; Lin, B. Novel Aqueous Nickel-Bismuth Batteries Using NiMoO4@NiCo-Layered Double Hydroxide Heterostructure Nanoarrays and Bi2O2CO3 Microspheres as Advanced Electrode Materials. Electrochim. Acta 2019, 323, 134819.

(47) Rama Raju, G. S.; Pavitra, E.; Nagaraju, G.; Chodankar, N. R.; Vishwanath, S. K.; Park, J. Y.; Huh, Y. S.; Han, Y. K. Engineering: Rhynchostylis Retusa -like Heterostructured α-Nickel Molybdate with Enhanced Redox Properties for High-Performance Rechargeable Asymmetric Supercapacitors. J. Mater. Chem. A 2019, 7, 26893–26904.

(48) Xu, R.; Lin, J.; Wu, J.; Huang, M.; Fan, L.; Xu, Z.; Song, Z. A High-Performance Pseudocapacitive Electrode Material for Supercapacitors Based on the Unique NiMoO 4 /NiO Nanoflowers. Appl. Surf. Sci. 2019, 463, 721–731.

(49) Li, G.; Song, B.; Cui, X.; Ouyang, H.; Wang, K.; Sun, Y.; Wang, Y. Multidimensional and Binary Micro CuCo2O4/Nano NiMoO4 for High-Performance Supercapacitors. ACS Sustain. Chem. Eng. 2020, 8, 1687–1694.

(50) Feng, X.; Ning, J.; Wang, D.; Zhang, J.; Xia, M.; Wang, Y.; Hao, Y. Heterostructure Arrays of NiMoO4 Nanoflakes on N-Doping of Graphene for High-Performance Asymmetric Supercapacitors. J. Alloys Compd. 2020, 816, 152625.

CHAPTER 6. GENERAL CONCLUSION

In this dissertation, the energy storage mechanisms of different types of electrode materials from supercapacitors are introduced and their kinetic analysis is discussed. In order to achieve supercapacitors with higher energy density without sacrificing power density, four projects have been done. Firstly, a FCNT based hybrid electrochemical capacitors (with a voltage window of 1.5 V) using neutral bromide redox-active electrolyte is fabricated. It is proved that the addition of redox active species near positive electrode can dramatically enhance the overall energy density of the device and the high power density can be maintained due to the pure EDLC behavior of the negative electrode. Besides, in order to solve the problems of liquid electrolyte leakage, a hybrid supercapacitor with solid-state redox-active hydrogel polymer electrolytes is built. The special pH value difference between positive electrolyte and negative electrolyte cannot only ensure the occurrence of reversible Br^-/Br^{3-} redox reaction but also extend the voltage window of the whole cell to 1.6 V and, thus, the energy density of this solid-state cell can be improved. Then, a asymmetric supercapacitor with a voltage window of 2.1 V made of Ni-Mn bimetallic oxide nanosheets as positive electrode and FCNT as negative electrode is made. It has been discussed that the pseudocapacitive performance of the prepared A-Ni-MnBMO mostly originates from the redox reactions of Mn^{3+}/Mn^{4+} whose reversibility and activity can be boosted by the combination of the increased material active sites caused by Na^+ insertion/desertion after CV activation process and the change of the electronic structure of MnO_2 through the incorporation of Ni. As a result, A-Ni-MnBMO electrode shows a maximum specific capacitance of 510 F g^{-1} and the A-Ni-MnBMO//FCNT hybrid supercapacitor can deliver a maximum energy density of 27 Wh kg^{-1} (at 0.5 A g^{-1}) and a maximum power density of 11049.2 W kg^{-1} (at 16 A g^{-1}). Moreover, a Venus fly-trap like hierarchical NiCoMn-

O@$NiMoO_4$@C nanosheet arrays electrode is designed and successfully synthesized via a multi-step hydrothermal method. The prepared NiCoMn-O nanosheet is used as conductive backbone (since its electrical conductivity is better than any of its bimetallic or monometallic counterparts) for growing $NiMoO_4$ and carbon protection shell and the self-decorated nanoneedles on its surface can create more electroactive surface area for electrolyte to access (i.e. The ion transport path is shortened). $NiMoO_4$ layer is the most important redox active material in this composite since its high electrochemical activity in alkaline solution. The incorporation of carbon protection shell (which is derived from glucose) cannot only increase the overall electric conductivity of the composite but also improve its cycling stability via buffering the volume change during the charge/discharge processes. As a result, with the synergistic effect of these components, NiCoMn-O@$NiMoO_4$@C can provide the highest specific capacitance of 2189.5 F/g at 0.25 A/g and the prepared NiCoMn-O@$NiMoO_4$@C//AC hybrid supercapacitor (with a voltage window of 1.6 V) can provide a maximum energy density of 59.9 Wh/kg (with a power density of 214.1 W/kg) at 0.25 A/g and a maximum power density of 6467.9 W/kg (with an energy density of 13.9 Wh/kg) at 12 A/g.

APPENDIX A. SUPPORTING INFORMATION I

Functionalized carbon nanotube based hybrid electrochemical capacitors using neutral bromide redox-active electrolyte for enhancing energy density

Xiaohui Tang, Yu Hui Lui, Bolin Chen, Shan Hu*

Department of Mechanical Engineering, Iowa State University, Ames, Iowa, 50010, USA

*Correspondence author E-mail: shanhu@iastate.edu

Methylene blue (MB) adsorption method

MB adsorption is one of the standard methods for evaluating SSA of carbon materials.[1, 2, 3, 4] UV-vis spectroscopy is used to determine the SSA through a MB concentration working curve. The method used in this paper is the method from Guo et al.'s work after minor modification.[1] To construct the working curve, MB solution of known concentration C^0_{MB} = 2 mg mL^{-1} is diluted at 600, 700, 800, 900, 1000, and 1100 times and the corresponding concentrations were plotted against the intensity of light absorbance at 664nm. FCNT and raw CNT electrodes with known active material mass (m_{FCNT} and $m_{raw\ CNT}$) are dipped into 2 mL of 2 mg mL^{-1} solution in two separate vials and left for 24 hours in order to reach adsorption equilibrium. The resulting solutions are diluted for 1100 times and measured under UV-vis spectroscopy to obtain the intensity of absorbance at 664 nm. The resulting solution concentration ($C_{MB,\ FCNT}$ and $C_{MB,\ raw\ CNT}$) are calculated through the previous constructed working curve. The mass of the absorbed MB is calculated through

$$m_{MB} = (2ml \times 2mg\ mL^{-1}) - C_{MB,i} \times (2.0mL), \quad i = \text{FCNT or raw CNT}$$

The SSA of FCNT and CNT can be calculated using following equation

$$SSA(m^2\ g^{-1}) = 2.54 \times m_{MB}/m_i \quad i = \text{FCNT or raw CNT}$$

The value 2.54 is a standard value for the area (m^2) covered by 1 mg of MB.[1, 4] The calculated SSA for FCNT is 1463.077 m^2 g^{-1} and for CNT is 914.353 m^2 g^{-1}.

Electrochemical active surface area

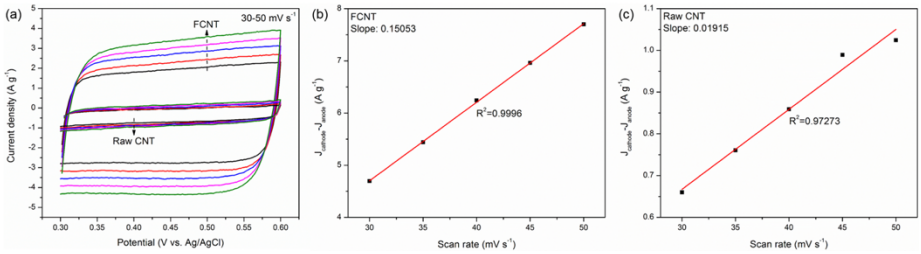

Figure S2.1. (a) CV curves of raw CNT and FCNT electrodes measured in the 1M Na_2SO_4 electrolyte with the potential range of 0.3-0.6 V (vs. Ag/AgCl). The specific capacitance and electrochemical active surface area estimation of (b) FCNT and (c) raw CNT electrodes by plotting the differences in current density at 0.45 V (vs. Ag/AgCl) as a function of scan rate fitted to a linear regression. The value of specific capacitance (F g^{-1}) is 500 times of the slope.

The specific capacitance and electrochemical active surface area of raw CNT and FCNT electrodes can be achieved by using a simple CV test reported by Liang et al. with some minor modifications.[5] As shown in figure S2.1a narrow potential window (0.3-0.6 V vs. Ag/AgCl) with no faradic process is utilized for measuring the current. In this non-faradic range, it is believed that all capacitance is contributed by electrical double layer and its value is linearly proportional to the electrochemical active surface area. The difference of cathodic current density and anodic current density at 0.45 V (vs. Ag/AgCl) is plotted with the corresponding scan rates. After the linear fit, the specific electrical double layer capacitance (C_{dl}) can be calculated by using the obtained slope in the following formula.

$$C_{dl} = \frac{\text{Slope}\times 1000}{2} = 500\times\text{Slope} \ (\text{F g}^{-1})$$

From figure S2.1b and c, the C_{dl} of FCNT and raw CNT electrodes are 75.265 and 9.575 F g^{-1}, respectively. Therefore, it can be concluded that the electrochemical active surface area of

FCNT electrode is much larger than that of raw CNT electrode, indicating its better electrochemical performance in aqueous electrolyte.

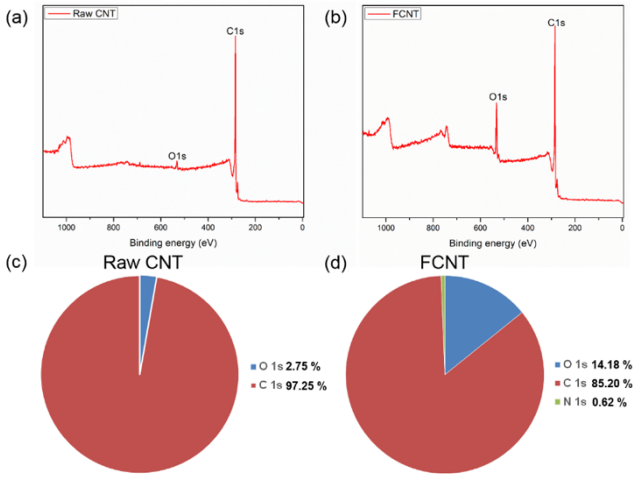

Figure S2.2. XPS full spectrum of (a) raw CNT and (b)FCNT. The atomic concentration of different elements calculated from (c) raw CNT and (d) FCNT via XPS full spectrums.

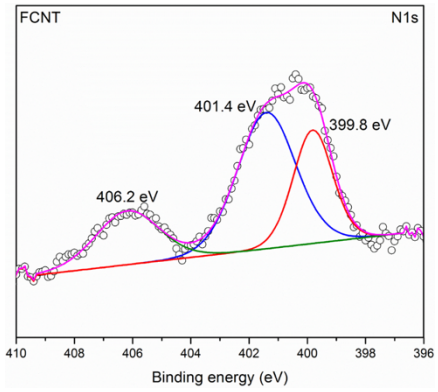

Figure S2.3. XPS N1s spectrum of FCNT.

As shown in figure S2.3, the N1s narrow-scan spectrum can be resolved into three components which is located at 399.8 eV (pyrrolic N), 401.4 eV (graphitic N) and 406.2 eV (adsorbed N species).[6, 7, 8]

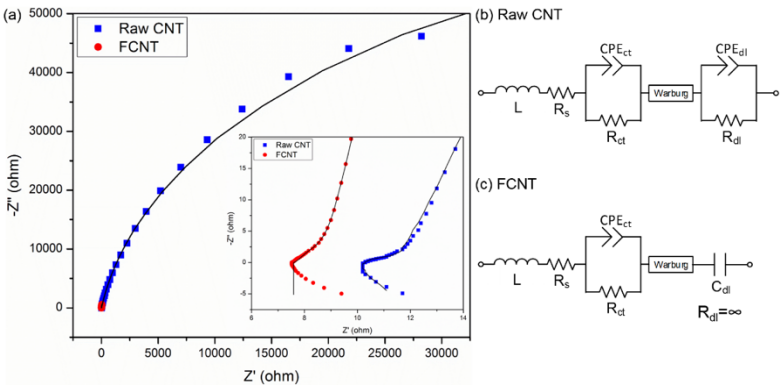

Figure S2.4. (a) Nyquist plot of electrodes made of raw CNT (Blue) and FCNT (Red) in 1M Na_2SO_4 electrolyte. Equivalent circuit model of the EIS tests in (b) raw CNT (c) FCNT.

Table S2.1. Results of fitting equivalent circuit model to the EIS data

	Raw CNT	FCNT	Unit
R_s	10.26	7.584	ohm
R_{dl}	134.8e3	∞	ohm
C_{dl}	0.22	32.91	mF
Goodness of Fit	1.086e-3	754.9-6	

EIS (with the frequency range from 0.01 Hz to 1MHz) is measured in a three-electrode system, where FCNT is used as working electrode, Ag/AgCl (1M KCl) as reference electrode, and Pt mesh as counter electrode. The electrolyte is 1M Na_2SO_4. The DC voltage is 0.5V and the AC amplitude is 50mV. The same EIS measurement is performed with raw CNT as working electrode for comparison. Nyquist plots of both FCNT and raw CNT electrodes are shown in figure S2.4a. The insert in figure S2.4a shows the enlargement of the high frequency part of the Nyquist plot. Equivalent circuit models shown in figure S2.4b and c are used to fit the Nyquist spectras of raw CNT and FCNT electrodes, respectively. Table S2.1 summarize the fitting results using the circuit models in figure S2.4b and c. In the circuit model, R_s represents the high frequency series resistance consisting of the electrolyte's ionic resistance and the electrode materials' electrical resistance. It can be observed that the value of R_s from FCNT electrode is 7.584 ohm, which is lower than that from raw CNT electrode (10.26 ohm). The lower Rs value

of FCNT electrode may be caused by the introduction of carboxyl groups to FCNT surface by acid treatment. The carboxyl surface groups can increase the ionic conductivity of electrolyte inside the porous electrode, and thus reduce the ionic resistance for FCNT electrode. As a result, the R_s of FCNT electrode is effectively reduced compared with that of raw CNT. Next, a parallel constant phase element (CPE_{rt}) and resistor (R_{ct}) are used to model the depressed semicircles showing up in the middle to high frequency range, indicating the capacitance and the charge transfer resistance (R_{ct}) between the current collector and active material, which, in our case, is the inner and outer surface parts of FCNT electrode, respectively.[9, 10] Constant phase elements (CPE) are usually used to substitute the capacitances in electrical capacitors because of the surface inhomogeneous and porous conditions.[11, 12] The semicircle ends at the knee frequency and the Nyquist plots develop into a straight-line at low frequency range. This part of the Nyquist spectra is related to the diffusion of electrolyte ions into the bulk of electrode materials, which is represented as a Warburg diffusion element in the circuit model. It is noticed that an inductance, whose performance is the tail at high frequency region, are taken into account as well. Finally, the Nyquist spectra becomes a straight-line with steeper slope in the ultra-low frequency range, which are modeled as a parallel constant phase element (CPE_{dl}) and resistor (R_{dl}) in raw CNT electrode and a capacitor (C_{dl}) in FCNT electrode. In detail, CPE_{dl} represents the electrical double layer capacitor and R_{dl} is the corresponding leakage resistance. The circuit model of FCNT electrodes shown in figure S2.3c are almost similar to that of raw CNT (figure S2.3b) except the missing R_{dl} and the replace of CPE_{dl} by C_{dl}. The physical meaning of disappearance of R_{dl} in the FCNT circuit model is that the leakage resistance of electrical double layer capacitor becomes infinity, revealing low self-discharge performance. C_{dl} used here indicates FCNT electrode behaves like an ideal capacitor and it has higher EDL capacitance

value (32.91 mF) than that in raw CNT electrode (0.22 mF). The higher C_{dl} value of the FCNT electrode is likely due to the effects of carboxyl groups, which not only improve the electrolyte wettability and consequently makes FCNT electrode surface more accessible to electrolyte ions, but also introduce pseudo-capacitance due to the redox reaction of the carboxyl groups.[13, 14]

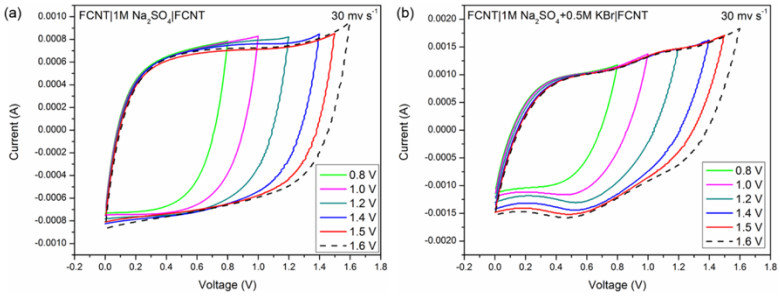

Figure S2.5. CV curves of (a) FCNT|1M Na_2SO_4|FCNT and (b) FCNT|1M Na_2SO_4+0.5M KBr|FCNT cells measured at different potential window at a scan rate of 30 mV/s.

The potential window of the assembled FCNT|1M Na_2SO_4|FCNT cell was detected by CV at the scan rate of 30 mV/s (figure S2.5a). From 0.8 V to 1.5 V, the rectangular-shaped CV curves can be observed indicating their typical electrical double-layer behavior.[15] Besides, the intensities of the maximum current of these curves have almost same values revealing that no electrochemical reactions occurred during these processes. However, when the voltage window reached up to 1.6 V (dash line), a trend of increase of current is able to be noted at both high potential range and low potential range, suggesting the occurrence of water electrolysis. As we all know, electrolysis of aqueous electrolyte can not only destroy the structure of the energy storage devices but also lower their working life. Thus, comparing with 1.6V, 1.5 V is more suitable for using as the voltage window for the FCNT|1M Na_2SO_4|FCNT cell due to its higher stability. For FCNT|1M Na_2SO_4+0.5M KBr|FCNT cell, as the increase of voltage window, the CV curves in figure S2.5b do not show the ideal rectangular shape because of the occurrence of redox electrochemical reactions caused by the redox additives (KBr) and the intensities of the

maximum current increase. Therefore, the potential window of this cell cannot be determined through CV tests. However, the two electrolytes have the similar pH value which close to neutral, the maximum voltage of these two cells should be comparable. Thus, 1.5 V can be a good option. Further proof of determining voltage window can be find in GCD test shown in figure 2.5.

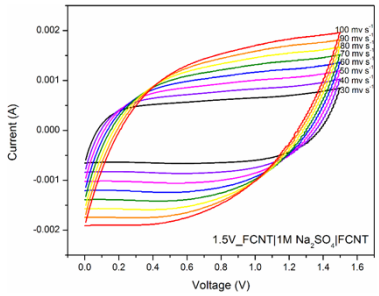

Figure S2.6. CV curves of FCNT|1M Na_2SO_4|FCNT cell at different scan rates at the voltage window of 1.5 V.

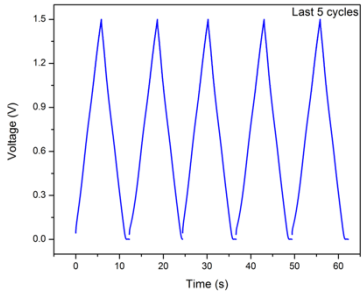

Figure S2.7. Last 5 cycles of 10000 cycles GCD test.

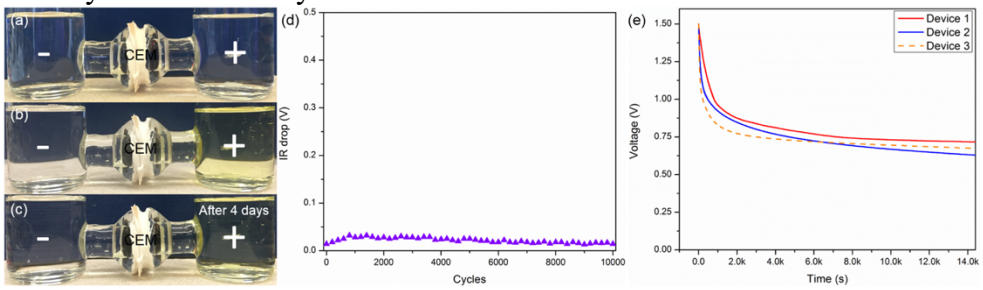

Figure S2.8. Functionality and durability of cation exchange membrane. Images of the color of 1M Na_2SO_4+0.5M KBr electrolyte: (a) before and (b) after charging to 1.5 V and floating for 2 hours. (c) Image of the corresponding electrolyte after 4 days. (d) IR drop during the 10000 cycles GCD tests. (e) SDC curves of device 1 (FCNT|1M Na_2SO_4+0.5M KBr|FCNT supercapacitor with cation exchange membrane), device 2 (FCNT|1M Na_2SO_4|FCNT supercapacitors with cation exchange

membrane) and device 3 (FCNT|1M Na_2SO_4+0.5M KBr|FCNT supercapacitor without cation exchange membrane). The data was recorded after the devices were pre-charged to 1.5 V at a constant current of 1 mA.

The main functionality of the cation exchange membrane (CEM) for the hybrid supercapacitor is to block the migration of Br^{3-} ions from the positive electrode to the negative electrode. On the other hand, the CEM still allows the migration of cations (K^+ and Na^+) across the membrane to maintain low electrolyte resistance and internal resistance of supercapacitor. The migration of redox species between electrodes is known to be a major contributor of self-discharge in supercapacitors with redox active electrolyte.[16] As discussed before, Br^{3-} ions are generated during the charge process at the anode. Without the CEM, the Br^{3-} ions will diffuse to the surface of the cathode. Since the potential of the cathode drops to -0.75 V vs Ag/AgCl via charging the EDL (figure 2.5d), a potential much lower than the equilibrium potential of Br^-/Br^{3-} (0.834 V vs. Ag/AgCl), Br^{3-} will be easily reduced by the cathode. This internal shuttling of Br^{3-} between two electrodes can cause significant self-discharge of the FCNT|1M Na_2SO_4+0.5M KBr|FCNT supercapacitor and CEM has been suggested as an effective strategy for blocking the shuttling.[16] In this study, the following experiments were performed to validate the functionality and durability of the CEM.

As shown in figure S2.8. CEM is sandwiched between two electrolyte compartments (i.e. anolyte and catholyte) and sealed by epoxy. As shown in figure S2.8a, at the initial state both compartments are filled with transparent 1M Na_2SO_4+0.5M KBr electrolyte. The color of the electrolyte at positive electrode (i.e. anolyte) turns into yellowish color after charging the cell to 1.5V and floating for 2 hours (figure S2.8b). The yellow appearance is characteristic color of Br^{3-}, demonstrating that Br^{3-} was generated at the positive electrode during charging. Whereas the color of the electrolyte at negative electrode (i.e. catholyte) is still transparent, revealing pure

EDLC behavior and most importantly proving that the CEM successfully blocked the diffusion of Br^{3-} into the catholyte. The durability of CEM is confirmed by observing the color change of the electrolyte as time passes. In figure S2.8c, it is noticed that, after 4 days, the electrolytes at positive electrode and negative electrode are still yellow and transparent, respectively, suggesting the durability of the Br^{3-}-blocking function of CEM. To test the durability of the cation exchange function of CEM, the discharge voltages profile during the 10000 cycles GCD tests with high current density of 10 A g^{-1} was examined. The IR drop of these discharge voltages are consistently small for the 10000 cycles (figure S2.8d), indicates that the internal resistance of the cell, which includes the electrolyte resistance, did not change after 10000 cycles. In other words, the cation transport tunnel in the CEM was not blocked, further proving the good durability of the CEM.

To further prove that CEM could block the migration of Br^{3-} between two electrodes and reduce the self-discharge of FCNT|1M Na_2SO_4+0.5M KBr|FCNT supercapacitor, self-discharge tests were performed with two FCNT|1M Na_2SO_4+0.5M KBr|FCNT supercapacitors, one with CEM and the other without. In the self-discharge tests, all supercapacitors were charged to 1.5V with constant current of 1 mA followed by four-hour self-discharge. In figure S2.8e, red solid curve is the self discharge profile of the redox-active supercapacitor with CEM (Device 1) and orange dash curve is that of the same supercapacitor but without CEM (Device 3). The self discharge of Device 1 (with CEM) is better that that of Device 3 (without CEM), further proving that CEM is important for reducing the self-discharge caused by shuttling of Br^{3-}. The self-discharge profiles of redox-active supercapacitors with and without CEM (Device 1 and 3) are both tested to be better than that of the EDLC (Device 2), because the positive electrode of the redox-active supercapacitors is a battery-type electrode whose potential is thermodynamically

stabilized at the equilibrium potential for the Br^-/ Br^{3-} redox pair. Whereas in the EDLC the potentials at both electrodes are electrostatically determined and have no mechanism thermodynamically stabilizing them.[16] It should be noted that the self-discharge tests were only performed to prove the functionality of the membrane and the self-discharge performances of all devices are not optimized yet. Minimizing self-discharge through optimizing each component of a supercapacitor is the authors' ongoing effort and is beyond the scope of this paper.

Table S2.2. The selected performance of FCNT|1M Na_2SO_4|FCNT cell tested at different voltage windows (0.5 A/g).

Voltage (V)	Specific capacitance (F/g)	Working voltage (V)	IR drop (V)	Energy densiy (Wh/kg)	power density (W/kg)	Columbic efficiency (%)
0.8	19.99	0.78	0.02	1.76801555	199.5252658	99.6628456
1	20.2	0.9978	0.0022	2.79322469	251.7048532	98.957413
1.2	20.89	1.195	0.005	4.143255868	301.5104331	97.7035785
1.4	21.79	1.395	0.005	5.889428438	351.7243261	92.1465969
1.5	23.65	1.491	0.009	7.302203563	376.2944865	90.712963
1.6	23.45	1.595	0.005	8.28574809	401.7332407	82.7229299

Table S2.3. The selected performance of FCNT|1M Na_2SO_4+0.5M KBr|FCNT cell tested at different voltage windows (0.5 A/g).

Voltage (V)	Specific capacitance (F/g)	Working voltage (V)	IR drop (V)	Energy densiy (Wh/kg)	power density (W/kg)	Columbic efficiency (%)
0.8	59.89	0.7967	0.0033	5.279726806	399.5588922	105.0177096
1	62.85	0.9976	0.0024	8.687316947	251.8062883	101.7523364
1.2	62.74	1.196	0.004	12.46448609	301.9660156	99.285374
1.4	76.52	1.393	0.007	20.62266076	349.7012659	94.3294043
1.5	92.12	1.487	0.013	28.29067893	372.1097703	88.9044616
1.6	169.5	1.555	0.045	56.92433854	389.3001876	63.4199134

Table S2.4. The selected performance of FCNT|1M Na_2SO_4|FCNT cell tested at different current densities (1.5 V).

Current density (A/g)	Specific capacitance (F/g)	Working voltage (V)	IR drop (V)	Energy densiy (Wh/kg)	power density (W/kg)	Columbic efficiency (%)
0.5	23.65	1.491	0.009	7.302203563	376.2944865	90.712963
1	22.74	1.491	0.009	7.021230825	747.8234015	94.2388478
2	21.96	1.494	0.006	6.8077098	1497.113945	96.6105285
4	21.28	1.493	0.007	6.588078156	3001.402349	98.4077497
6	20.86	1.491	0.009	6.440759675	4484.861669	98.8918085
8	20.53	1.489	0.011	6.321874185	5960.908084	99.0462898
10	20.27	1.485	0.015	6.208320938	7408.006422	99.2088794
15	19.75	1.486	0.014	6.057204306	11097.16819	99.3581981
20	19.39	1.48	0.02	5.898868889	14696.14394	99.3331687
40	18.5	1.475	0.025	5.590147569	29238.02303	99.4829369
50	18.06	1.474	0.026	5.449795633	36217.95141	99.69673

Table S2.5. The selected performance of FCNT|1M Na_2SO_4+0.5M KBr|FCNT cell tested at different current densities (1.5 V).

Current density (A/g)	Specific capacitance (F/g)	Working voltage (V)	IR drop (V)	Energy densiy (Wh/kg)	power density (W/kg)	Columbic efficiency (%)
0.5	92.12	1.487	0.013	28.29067893	372.1097703	88.9044616
1	75.04	1.487	0.013	23.04529469	746.7422221	96.5721409
2	71.62	1.482	0.018	21.8473229	1482.570451	97.4884336
4	63.53	1.487	0.013	19.51049536	2990.114231	98.7956342
6	59.32	1.481	0.019	18.07085757	4458.881923	99.3490643
8	55.44	1.478	0.022	16.8205268	5925.038795	99.4325622
10	51.56	1.481	0.019	15.70690183	7412.801072	99.4384651
15	45.97	1.471	0.029	13.81552372	11020.58174	99.1057338
20	44.07	1.466	0.034	13.15462568	14638.84156	98.956044
40	41.43	1.45	0.05	12.09813542	28881.49038	99.2352941
50	40.38	1.443	0.057	11.67794648	35779.24026	99.5752427

References:

(1) Guo, H.-L.; Su, P.; Kang, X.; Ning, S.-K. Synthesis and Characterization of Nitrogen-Doped Graphene Hydrogels by Hydrothermal Route with Urea as Reducing-Doping Agents. J. Mater. Chem. A 2013, 1, 2248–2255.

(2) Chen, J.; Sheng, K.; Luo, P.; Li, C.; Shi, G. Graphene Hydrogels Deposited in Nickel Foams for High-Rate Electrochemical Capacitors. 2012, 4569–4573.

(3) Cho, E. J.; Senecal, T. D.; Kinzel, T.; Zhang, Y.; Watson, D. A.; Buchwald, S. L. Laser Scribing of High-Performance and Flexible Graphene-Based Electrochemical Capacitors. 2009, 9139, 23–25.

(4) Yang, C.; Shen, J.; Wang, C.; Fei, H.; Bao, H.; Wang, G. All-Solid-State Asymmetric Supercapacitor Based on Reduced Graphene Oxide/Carbon Nanotube and Carbon Fiber Paper/Polypyrrole Electrodes. J. Mater. Chem. A 2014, 2, 1458–1464.

(5) Liang, H.; Gandi, A. N.; Anjum, D. H.; Wang, X.; Schwingenschlögl, U.; Alshareef, H. N. Plasma-Assisted Synthesis of NiCoP for Efficient Overall Water Splitting. Nano Lett. 2016, acs.nanolett.6b03803.

(6) Podila, R.; Chacón-Torres, J.; Spear, J. T.; Pichler, T.; Ayala, P.; Rao, a. M. Spectroscopic Investigation of Nitrogen Doped Graphene. Appl. Phys. Lett. 2012, 101, 123108.

(7) Hu, T.; Sun, X.; Sun, H.; Xin, G.; Shao, D.; Liu, C.; Lian, J. Rapid Synthesis of Nitrogen-Doped Graphene for a Lithium Ion Battery Anode with Excellent Rate Performance and Super-Long Cyclic Stability. Phys. Chem. Chem. Phys. 2014, 16, 1060–1066.

(8) Niu, J.; Gao, H.; Wang, L.; Xin, S.; Zhang, G.; Wang, Q.; Guo, L.; Liu, W.; Gao, X.; Wang, Y. Facile Synthesis and Optical Properties of Nitrogen-Doped Carbon Dots. New J. Chem. 2014, 38, 1522–1527.

(9) Kuriyama, N.; Sakai, T.; Miyamura, H.; Uehara, I.; Ishikawa, H.; Iwasaki, T. Electrochemical Impedance and Deterioration Behavior of Metal Hydride Electrodes. J. Alloys Compd. 1993, 202, 183–197.

(10) Karthikeyan, K.; Aravindan, V.; Lee, S. B.; Jang, I. C.; Lim, H. H.; Park, G. J.; Yoshio, M.; Lee, Y. S. A Novel Asymmetric Hybrid Supercapacitor Based on Li2FeSiO 4 and Activated Carbon Electrodes. J. Alloys Compd. 2010, 504, 224–227.

(11) Tokutake, K.; Nishi, H.; Ito, D.; Okazaki, S.; Serizawa, Y. Relationship between Degradation Characteristics of Organic Coating on Internal Bottom Plate of Oil Storage Tank and Constant-Phase Element Parameter Values. Prog. Org. Coatings 2015, 87, 69–74.

(12) He, Z.; Mansfeld, F. Exploring the Use of Electrochemical Impedance Spectroscopy (EIS) in Microbial Fuel Cell Studies. Energy Environ. Sci. 2009, 2, 215–219.

(13) Shen, J.; Liu, A.; Tu, Y.; Foo, G.; Yeo, C.; Chan-Park, M. B.; Jiang, R.; Chen, Y. How Carboxylic Groups Improve the Performance of Single-Walled Carbon Nanotube Electrochemical Capacitors? Energy Environ. Sci. 2011, 4, 4220.

(14) Oh, Y. J.; Yoo, J. J.; Kim, Y. Il; Yoon, J. K.; Yoon, H. N.; Kim, J. H.; Park, S. Bin. Oxygen Functional Groups and Electrochemical Capacitive Behavior of Incompletely Reduced Graphene Oxides as a Thin-Film Electrode of Supercapacitor. Electrochim. Acta 2014, 116, 118–128.

(15) Chen, J. H.; Li, W. Z.; Wang, D. Z.; Yang, S. X.; Wen, J. G.; Ren, Z. F. Electrochemical Characterization of Carbon Nanotubes as Electrode in Electrochemical Double-Layer Capacitors. Carbon N. Y. 2002, 40, 1193–1197.

(16) Conway, B. E. Electrochemical Supercapacitors: Scientific Fundamentals and Technological Applications.; 2013.

APPENDIX B. SUPPORTING INFORMATION II

Redox-Active Hydrogel Polymer Electrolytes with Different pH Values for Enhancing the Energy Density of the Asymmetric Solid-State Supercapacitor

*Xiaohui Tang, Yu Hui Lui, Abdul Rahman Merhi, Bolin Chen, Shaowei Ding, Bowei Zhang, and Shan Hu**

Department of Mechanical Engineering, Iowa State University, Ames, IA, 50010, USA

* Corresponding author Email: shanhu@iastate.edu

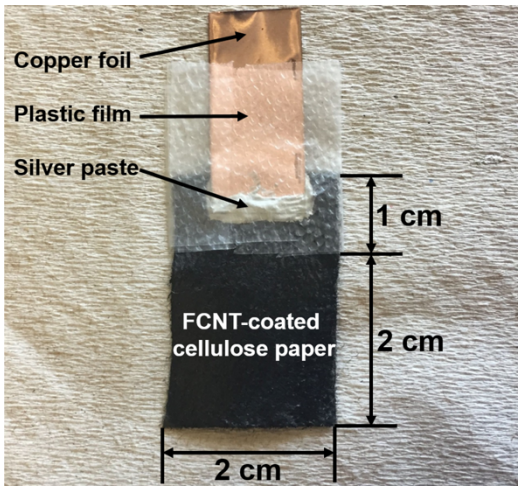

Figure S3.1. The detailed information of a single FCP electrode.

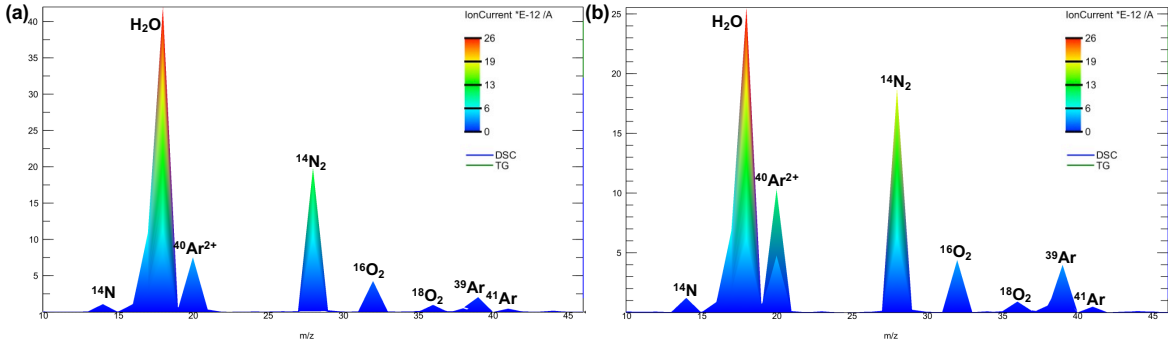

Figure S3.2. (a) Mass spectrum of the acidic PVA-BH-LiBr hydrogel and (b) mass spectrum of the neutral PVA-BNa-LiBr hydrogel.

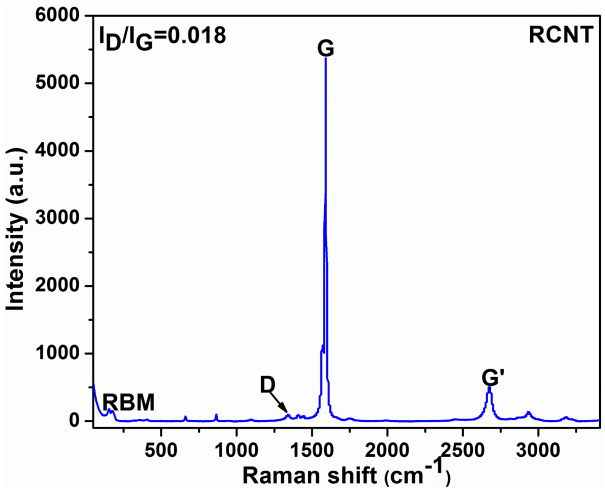

Figure S3.3. Raman spectroscopy of raw CNT.

Figure S3.3 shows the Raman spectroscopy of raw CNT at 532 nm. The radical breathing mode (at 163 cm^{-1}) and G mode (at 1590 cm^{-1}) indicate the material is single-wall carbon nanotube and the vibration at 1347 cm^{-1} can be attributed to D mode which reflects the degree of structural detects.

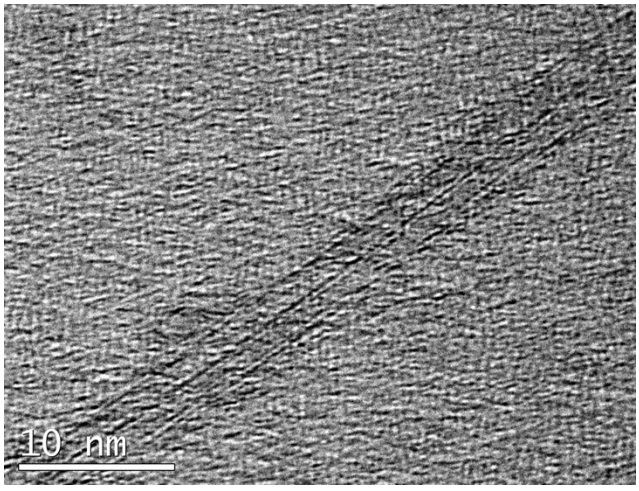

Figure S3.4. TEM image of single-wall FCNT.

The carbon nanotube (CNT) used in this paper is purchased from Timesnano and the product name is TNSAR. According to the information provided in the website of Timesnano (http://www.timesnano.com/en/view.php?prt=3,29,48,183), this type of CNT has the single wall

structure. Furthermore, figure S3.4 gives the TEM image of FCNT. It can be observed that two nanotubes are bound together and each of them has a diameter of less than 2 nm and shows only single wall, which agree with the specification of TNSAR provided by the Timesnano shown in the website.

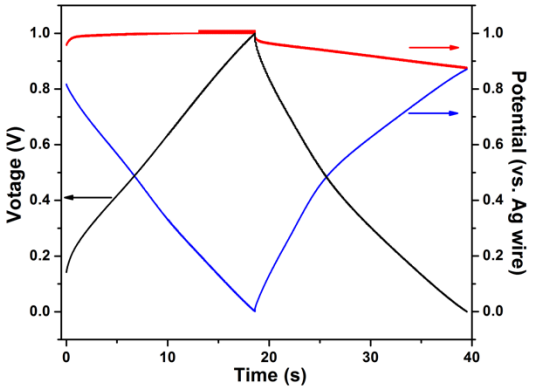

Figure S3.5. GCD profile of LA-SA asymmetric SC at the current density of 2A/g with a voltage window of 1V (black curve) and potential variation profiles (vs. Ag wire) of positive and negative electrodes (red and blue curves).

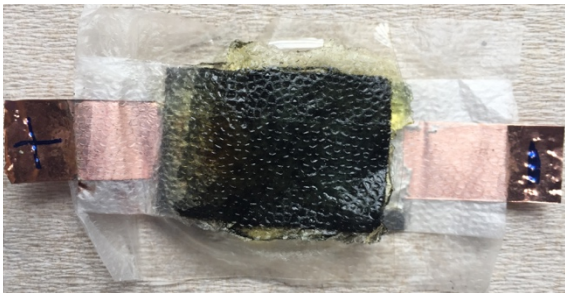

Figure S3.6. Digital image of LA-SA hybrid supercapacitor after cycling test.

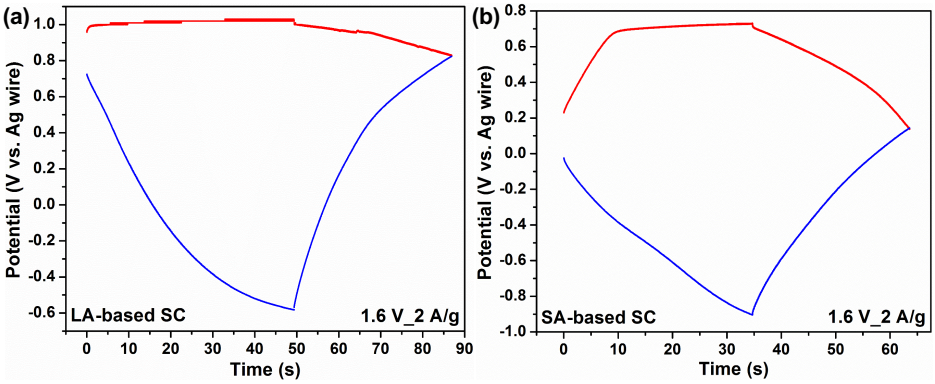

Figure S3.7. Potential variation profiles (vs. Ag wire) of positive and negative electrodes of (a) LA hybrid SC and (b) SA hybrid SC.

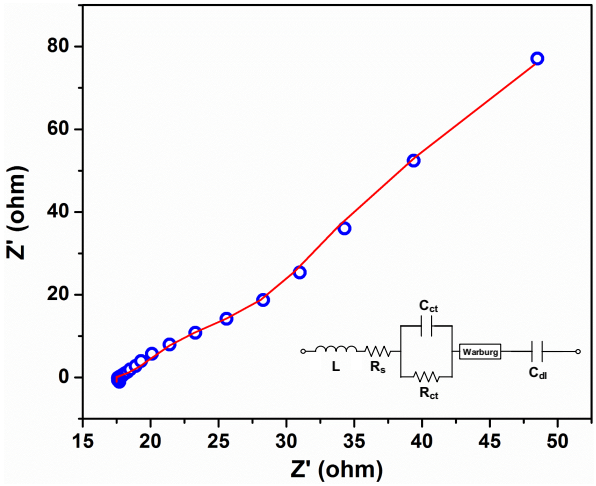

Figure S3.8. Electrochemical impedance spectroscopy of LA-SA hybrid SC: Nyquist plot (blue circle) representing the real and imaginary components of the impedance and the simulation curve fitted from the equivalent circuit model (inset).

The EIS of LA-SA hybrid SC is measured with the frequency range from 0.1 to 100 KHz. The DC voltage is 1.6 V and the AC amplitude is 50 mV. As shown in figure S3.8, the Nyquist plot is provided and the equivalent circuit model (shown in the inset) is used to fit the plot. According to the equivalent circuit model, Rs (from the high frequency range), which represents the resistance of the electrolyte and the Nafion 117 separator, is about 17.4 ohm. This value is a little bit higher than those water-based supercapacitors, but it is reasonable considering the use of solid state electrolytes and the Nafion 117 separator. In the middle frequency range, a parallel

capacitor (C_{ct}) and resistance (R_{ct}) are used to model the capacitance and the charge transfer resistance between the electrode and the electrolyte of the positive electrode.[1] The value of Rct, which can be found in table S3.1, is 44.1 ohm. This value can be strongly affected by the contact of PVA based electrolyte with FCNT. Besides, another capacitor (C_{dl}) is used to model the electric double layer behavior in the negative electrode. In addition, a Warburg impedance element, which exhibits as a straight line in the low frequency range, is added in order to model the ions diffusion from the electrolytes into bulk of electrode materials.[2] It can be noticed that an inductance is also put into the model for simulating the tail shown at the high frequency range.

Table S3.1. Results of fitting equivalent circuit model to the EIS data

	Raw CNT	Unit
R_s	17.43	ohm
R_{ct}	44.16	ohm
Goodness of Fit	159.7e-6	

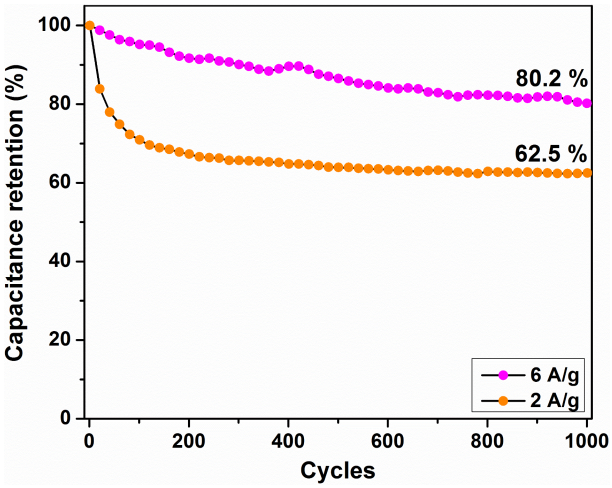

Figure S3.9. The capacitance retention after 1000 cycles of GCD tests at the current density of 6 and 2 A/g.

Table S3.2. The selected performance of LA-SA hybrid SC tested at different voltage windows (2 A/g).

Voltage (V)	Specific capacitance (F/g)	IR drop (V)	Energy densiy (Wh/kg)	power density (W/kg)	Coulombic efficiency (%)
1	33	0.0205	4.4	764.3	112.7
1.2	36	0.025	6.9	878.1	104.9
1.4	42	0.016	11.2	888.4	99.9
1.5	44	0.017	13.5	895.2	97.7
1.6	47	0.017	16.3	932.6	97.6
1.7	48	0.022	18.9	985.5	93.2
1.8	48	0.021	21.1	1017.3	90.6

Table S3.3. The selected performance of LA hybrid SC tested at different voltage windows (2 A/g).

Voltage (V)	Specific capacitance (F/g)	IR drop (V)	Energy densiy (Wh/kg)	power density (W/kg)	Coulombic efficiency (%)
1	27	0.0074	3.7	800.1	97.3
1.2	28	0.009	5.4	947.4	96.5
1.4	29	0.01	7.7	1079.8	94.1
1.5	30	0.013	9.2	1129.8	91.6
1.6	31	0.015	10.8	1175.6	89.8
1.7	33	0.031	12.8	1211.3	84.5

Table S3.4. The selected performance of SA hybrid SC tested at different voltage windows (2 A/g).

Voltage (V)	Specific capacitance (F/g)	IR drop (V)	Energy densiy (Wh/kg)	power density (W/kg)	Coulombic efficiency (%)
1	18	0.0137	2.4	842.4	93.8
1.2	20	0.013	3.8	1006.5	92.9
1.4	21	0.015	5.6	1165	89.9
1.5	22	0.014	6.7	1249.2	87.2
1.6	22	0.016	7.8	1331.3	83.4
1.7	23	0.015	9.1	1414.5	78.6

Table S3.5. The selected performance of LA-SA hybrid SC tested at different current densities (1.6 V).

Current density (A/g)	Specific capacitance (F/g)	IR drop (V)	Energy densiy (Wh/kg)	power density (W/kg)	Coulombic efficiency (%)
2	47	0.017	16.3	932.6	97.6
4	35	0.021	12.0	1991	98.3
6	29	0.025	9.9	3107.4	98.8
8	26	0.029	9.0	4271.7	98.8
10	25	0.032	8.4	5440.4	99.0
12	23	0.032	8.0	6598.3	99.4
15	22	0.039	7.6	8342.6	98.8

Table S3.6. The selected performance of LA hybrid SC tested at different current densities (1.6 V).

Current density (A/g)	Specific capacitance (F/g)	IR drop (V)	Energy densiy (Wh/kg)	power density (W/kg)	Coulombic efficiency (%)
2	31	0.015	10.8	1175.6	89.8
4	25	0.025	8.6	2416.7	96.7
6	23	0.025	8.0	3643.1	97.8
8	22	0.029	7.5	4863.9	98.2
10	21	0.024	7.3	6101.4	98.3
12	20	0.033	7.0	7303.5	98.4
15	20	0.035	6.6	9145.9	98.7

Table S3.7. The selected performance of SA hybrid SC tested at different current densities (1.6 V).

Current density (A/g)	Specific capacitance (F/g)	IR drop (V)	Energy densiy (Wh/kg)	power density (W/kg)	Coulombic efficiency (%)
2	22	0.016	7.8	1331.3	83.4
4	19	0.019	6.7	2798.5	90.0
6	19	0.034	6.4	4220.4	92.6
8	18	0.032	6.1	5652.0	94.5
10	17	0.037	5.9	7062.4	95.3
12	17	0.034	5.8	8497.0	95.9
15	17	0.039	5.6	10593.9	96.8

Table S3.8. Comparisons of energy density and power density with different reported values.

No.	Cell type	Electrode material	Electrolyte	Current density (A/g)	Voltage window (V)	Energy density (Wh/Kg)	Power density (W/Kg)	Year	Ref.
1	EDLC	Activated carbon	PVA-Na_2SO_4	0.2	1.8	13	106	2017	3
2	EDLC	N-doped porous carbon	PVA-KOH	0.1	0.9	17	44	2016	4
3	EDLC	Activated carbon	PVA-BMIMCl-Li_2SO_4	0.15	1.5	10.6	3400	2015	5
4	EDLC	Graphene hydrogel	PVA-H_2SO_4	1	1	6.5	287.4	2013	6
5	Redox	Activated carbon	PVA-H_2SO_4-HQ & PVA-H_2SO_4-MB	0.5	1	18.7	245	2015	7
6	Redox	Activated carbon	PVA-H_2SO_4-IC	0.3	1	13.26	150	2015	1
7	Redox	Activated carbon	PVA-PB	0.2	2	12.47	-	2016	8
8	Redox	PVA-PANI hydrogel on carbon cloth	PVA-H_2SO_4	0.25	0.8	18.7	107	2017	9
9	Redox	Activated carbon	PVA-H_2SO_4-KI-$VOSO_4$	0.5	0.8	25.4	190	2014	10
10	Redox	Functionalized CNT	PVA-BC-LA-LiBr & PVA-BC-SA-LiBr	2	1.6	16.3	932.6	This work	
					1.7	18.9	985.5		
					1.8	21.1	1017.3		

References:

(1) Ma, G.; Dong, M.; Sun, K.; Feng, E.; Lei, Z. A Redox Mediator Doped Gel Polymer as an Electrolyte and Separator for a High Performance Solid State Supercapacitor. J. Mater. Chem. A 2015, 3, 4035–4041.

(2) Sun, K.; Dong, M.; Feng, E.; Peng, H.; Ma, G.; Zhao, G.; Lei, Z. High Performance Solid State Supercapacitor Based on a 2-Mercaptopyridine Redox-Mediated Gel Polymer. RSC Adv. 2015, 5, 22419–22425.

(3) Batisse, N.; Raymundo-Piñero, E. A Self-Standing Hydrogel Neutral Electrolyte for High Voltage and Safe Flexible Supercapacitors. J. Power Sources 2017, 348, 168–174.

(4) Wang, K.; Xu, M.; Gu, Y.; Gu, Z.; Hua, Q. Symmetric Supercapacitors Using Urea-Modified Lignin Derived N-Doped Porous Carbon as Electrode Materials in Liquid and Solid Electrolytes. J. Power Sources 2016, 332, 180–186.

(5) Zhang, X.; Wang, L.; Peng, J.; Cao, P.; Cai, X.; Li, J.; Zhai, M. A Flexible Ionic Liquid Gelled PVA-Li2SO4 Polymer Electrolyte for Semi-Solid-State Supercapacitors. Adv. Mater. Interfaces 2015, 2, 1500267.

(6) Xu, Y.; Lin, Z.; Huang, X.; Liu, Y.; Huang, Y.; Duan, X. Flexible Solid-State Supercapacitors Based on Three-Dimensional Graphene Hydrogel Films. ACS Nano 2013, 7, 4042–4049.

(7) Zhong, J.; Fan, L.-Q.; Wu, X.; Wu, J.-H.; Liu, G.-J.; Lin, J.-M.; Huang, M.-L.; Wei, Y.-L. Improved Energy Density of Quasi-Solid-State Supercapacitors Using Sandwich-Type Redox-Active Gel Polymer Electrolytes. Electrochim. Acta 2015, 166, 150–156.

(8) Jiang, M.; Zhu, J.; Chen, C.; Lu, Y.; Pampal, E. S.; Luo, L.; Zhu, P.; Zhang, X. Superior High-Voltage Aqueous Carbon/Carbon Supercapacitors Operating with in Situ Electrodeposited Polyvinyl Alcohol Borate Gel Polymer Electrolytes. J. Mater. Chem. A 2016, 4, 16588–16596.

(9) Li, W.; Lu, H.; Zhang, N.; Ma, M. Enhancing the Properties of Conductive Polymer Hydrogels by Freeze-Thaw Cycles for High-Performance Flexible Supercapacitors. ACS Appl. Mater. Interfaces 2017, 9, 20142–20149.

(10) Fan, L.; Zhong, J.; Wu, J.; Lin, J.; Huang, Y. Improving the Energy Density of Quasi-Solid-State Electric Double-Layer Capacitors by Introducing Redox Additives into Gel Polymer Electrolytes. J. Mater. Chem. A 2014, 2, 9011.

APPENDIX C. SUPPORTING INFORMATION III

Ni-Mn Bimetallic Oxide Nanosheets as High-Performance Electrode Materials for Asymmetric Supercapacitors

*Xiaohui Tang, Bowei Zhang, Yui Hui Lui and Shan Hu**

Department of Mechanical Engineering, Iowa State University, Ames, IA, 50010, USA

* Corresponding author Email: shanhu@iastate.edu

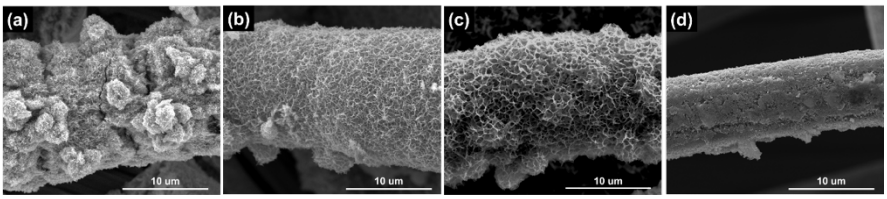

Figure S4.1. SEM images of electrodes produced from precursors with different molar ratio between Ni and Mn elements: (a) Ni:Mn=0:2; (b) Ni:Mn=0.5:1.5; (c) Ni:Mn=1:1; (d) Ni:Mn=2:0.

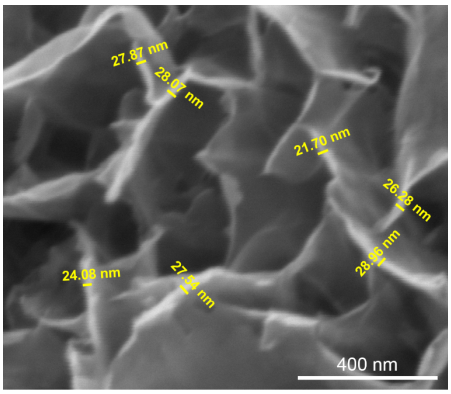

Figure S4.2. The thickness measurement of nanosheets.

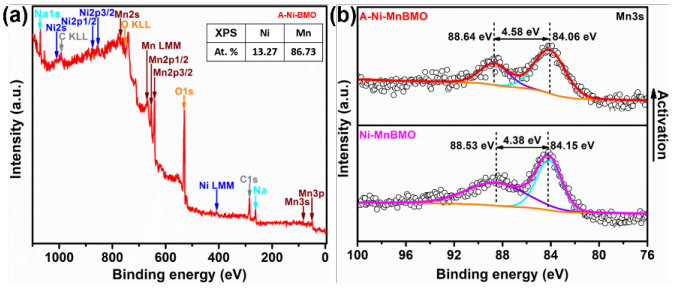

Figure S4.3. (a) Survey XPS spectrum of A-Ni-MnO activation electrode. (b) Mn3s core-level XPS spectrum of Ni-MnBMO and A-Ni-MnBMO activation electrodes.

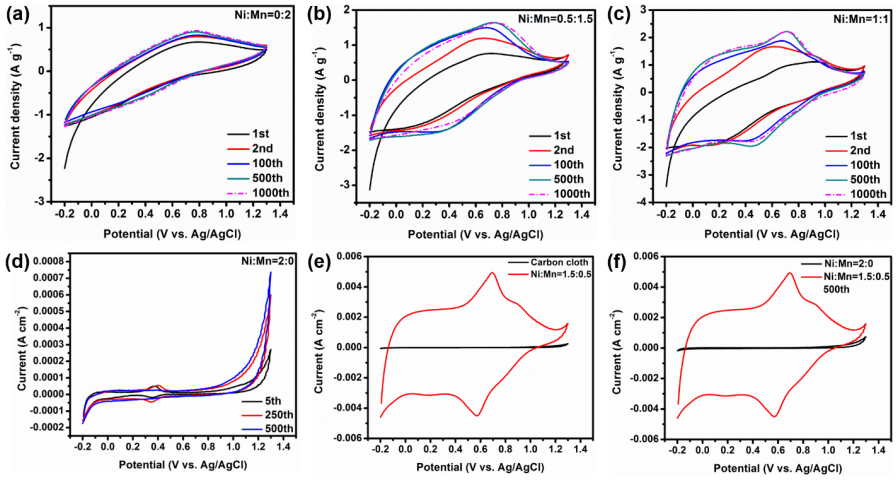

Figure S4.4. CV electrochemical activation processes (10 mV s^{-1}) of electrodes produced from precursors with different Ni/Mn molar ratios: (a) Ni:Mn=0:2; (b) Ni:Mn=0.5:1.5; (c) Ni:Mn=1:1; (d) Ni:Mn=2:0. (e) CV comparison of A-Ni-MnBMO electrode and bare carbon cloth in 1M Na_2SO_4 electrolyte at the scan rate of 10 mV s^{-1}. (f) CV comparison of A-Ni-MnBMO electrode and electrodes produced from precursors with Ni/Mn ratio of 2:0 at 500th activation cycle.

Table S4.1. Mass loading of samples synthesized from precursors with different Ni/Mn molar ratios.

Number	Molar ratio between $Ni(NO_3)_2$ and $KMnO_4$		Specific capacitance (F g^{-1}) after activation
1	0	2	35
2	0.5	1.5	72
3	1	1	107
4	1.5	0.5	482
5	2	0	Very small

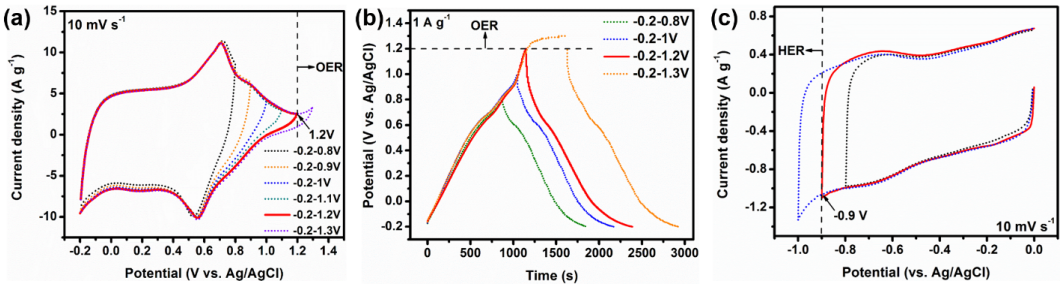

Figure S4.5. (a) CV curves of A-Ni-MnBMO electrode at different potential ranges. (b) GCD curves of A-Ni-MnBMO electrode at different potential ranges. (c) CV curves of FCNT electrode at different potential ranges.

The maximum working potential for A-Ni-MnBMO electrode that can be used in real device is investigated by a three-electrode CV test at a scan rate of 10 mV s^{-1} in different potential windows of -0.2-0.8 V, -0.2-0.9 V, -0.2-1 V, -0.2-1.1 V, -0.2-1.2 V and -0.2-1.3 V (vs. Ag/AgCl) shown in figure S4.5a. It can be observed that, as the potential increases beyond 1.2 V (vs. Ag/AgCl), there is an obvious increase of current during anodic scan, which is attributed to the occurrence of oxygen evolution reaction (OER).[1] Besides, the GCD curves of A-Ni-MnBMO electrode tested in different potential windows (shown in figure S4.5b) also confirm that, when the maximum potential is 1.3 V (vs. Ag/AgCl), a plateau representing OER in the charge curve and a large IR drop in the discharge curve can be observed. However, when the maximum potential is 1.2 V (vs. Ag/AgCl), a symmetric GCD curve with low IR drop and high coulombic efficiency (figure S4.6 a-b) can be found. Therefore, in order to maximize the potential window of positive electrode and minimize the decomposition of aqueous electrolyte, 1.2 V (vs. Ag/AgCl) is the most suitable maximum potential that can be utilized. In figure S4.5c, the maximum working potential range of FCNT electrode is investigate by a three-electrode CV test at a scan rate of 10 mV/s in different potential windows of -0.8-0 V, -0.9-0 V and -1-0 V (vs. Ag/AgCl). It can be observed that, when the potential is more negative than -0.9 V (vs. Ag/AgCl), an increase of current during the cathodic scan, which is ascribed to the occurrence of hydrogen evolution reaction (HER), can be observed.[2, 3] Therefore, the most suitable working potential range of FCNT electrode should be -0.9-0 V (vs. Ag/AgCl).

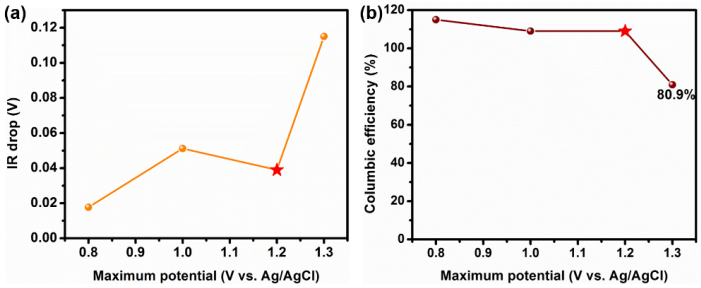

Figure S4.6. (a) IR drops and (b) Coulombic efficiencies of A-Ni-MnBMO electrode at different maximum potentials.

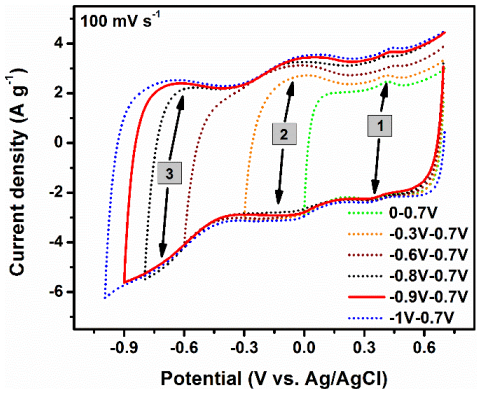

Figure S4.7. CV curves of FCNT at different potential ranges.

To the best of our knowledge, there are at least two possible processes happening on FCNT electrode during CV measurements. In order to fully investigate the possible pseudocapacitive behavior in our FCNT electrode, CV curves of FCNT at different potential ranges are measured in figure S4.7. It can be found that there are three pairs of peaks that can supply extra pseudocapacitance for EDLC FCNT electrode.

It has been discussed by many reported works that the functional groups, such as carboxyl group (-COOH), were introduced onto surface of single wall carbon nanotube (SWCNT) through acid functionalization treatment in order to increase its wettability in aqueous electrolyte. Besides, these introduced oxygen contained functional groups may also have reactions under different electrolyte conditions.[4, 5, 6, 7] For example,

$$-COOH + OH^- \leftrightarrow -COOH^- + H_2O$$

The exact redox potential of the oxygen contained functional groups are not listed in the reported papers. However, according to their CV curves, a pair of redox peaks that can often be observed at the potential range of about -0.3-0.1 V (vs. Ag/AgCl) at neutral condition may be ascribed to the reactions of carboxyl groups.[6] Therefore, peak pair 2 may be caused by the reaction of carboxyl groups. Peak pair 1 and 3 may come from the reactions of other the oxygen-contained functional groups. More work should be done in order to fully understand these processes.

Another possible process is the hydrogen adsorption/desorption process.[8, 9] Its mechanism is shown as:

$$C + xH_3O^+ + xe^- \leftrightarrow \langle CH_X \rangle + xH_2O$$

where $\langle C \rangle$ represents the carbon material and $\langle CH_X \rangle$ represents the hydrogen adsorbed carbon material. The reported nascent hydrogen started to be produced and adsorbed when the potential is more negative than -0.605 V (vs. Ag/AgCl) and the hydrogen desorption happens when the potential increases over -0.422 V (vs. Ag/AgCl).[9] Peak pair 3 is found to be roughly located within this range.

According to the green and yellow curves in figure S4.6, peak pair 1 and 2 can be observed when the hydrogen generation does not occur. It is because that the theoretical potential of hydrogen generation at neutral condition is about -0.413 V (vs. NHE which is about -0.649 V vs. Ag/AgCl). Even if we do not consider about the possible overpotential of hydrogen generation reaction, the potential of these peaks are more positive than this value, meaning that reaction 1 and 2 are totally not related to hydrogen but are very likely caused by the redox reactions of oxygen contained functional groups. However, since the reaction of peak pair 3 is

under the range of possible hydrogen generation, it may be caused by the hydrogen adsorption/desorption process.

It needs to mention that the above discussed mechanisms are only the assumptions based on our observation and the information collected from other reported papers. In order to fully figure out these processes, more work should be done.

Table S4.2. Detailed GCD data of A-Ni-MnBMO electrode.

Current density ($A\ g^{-1}$)	Specific capacitance ($F\ g^{-1}$)	Energy density ($Wh\ kg^{-1}$)	Power density ($W\ kg^{-1}$)	Output potential (V vs. Ag/AgCl)	IR drop (V vs. Ag/AgCl)	Coulombic efficiency (%)
1	573.7	147.4	429.9	1.161	0.039	108.6
2	549.7	141.2	958.4	1.162	0.038	103.4
4	527.2	131.5	2045.6	1.141	0.059	100.9
8	524.2	117.4	4152.8	1.072	0.128	100.4
16	499.0	103.2	8247.3	1.023	0.177	99.8
32	471.6	79.5	15436.6	0.902	0.298	100.0

Table S4.3. Fitted values of equivalent series resistance and charge transfer resistance from equivalent circuit model.

	ESR (ohm)	R_{ct} (ohm)
A-Ni-MnBMO	4.838	8.813
FCNT	4.059	0.235
A-Ni-MnBMO//FCNT	9.310	3.927

Table S4.4. Detailed GCD data of A-Ni-MnBMO//FCNT supercapcitor.

Current density ($A\ g^{-1}$)	Specific capacitance ($F\ g^{-1}$)	Energy density ($Wh\ kg^{-1}$)	Power density ($W\ kg^{-1}$)	Output potential (V)	IR drop (V)	Coulombic efficiency (%)
0.5	44.9	27.0	486.6	2.078	0.022	88.8
1	40.9	23.9	950.0	2.045	0.055	94.1
2	39.2	22.0	1880.2	2.011	0.089	97.3
4	35.4	18.7	3585.5	1.950	0.150	98.8
6	32.8	15.1	4987.5	1.819	0.281	99.2
8	31.6	14.2	6549.3	1.798	0.302	98.6
10	30.0	12.3	7772.3	1.724	0.376	99.3
12	27.9	10.6	8748.3	1.650	0.450	98.3
16	27.8	9.0	11049.2	1.531	0.569	98.3

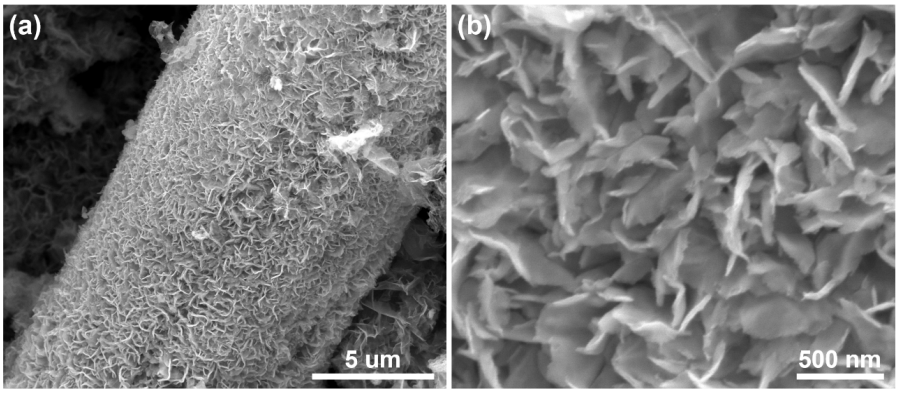

Figure S4.8. SEM images of A-NiMnBMO electrode after 3000-cycle cell level GCD test.

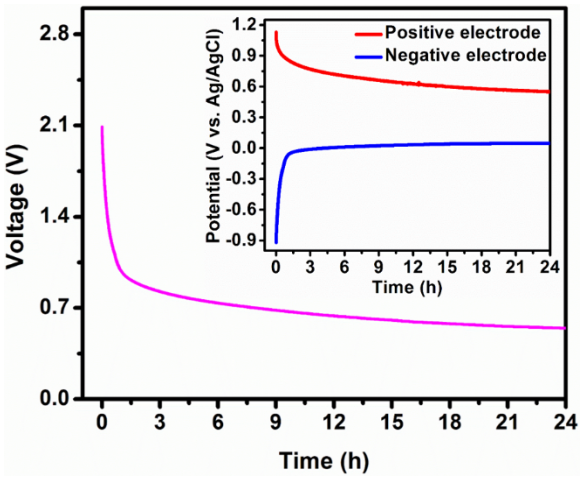

Figure S4.9. Self-discharge performance of A-Ni-MnBMO//FCNT supercapacitor. Inset is the potential variation during the self-discharge process.

References:

(1) Tang, X.; Lui, Y. H.; Merhi, A. R.; Chen, B.; Ding, S.; Zhang, B.; Hu, S. Redox-Active Hydrogel Polymer Electrolytes with Different PH Values for Enhancing the Energy Density of the Hybrid Solid-State Supercapacitor. ACS Appl. Mater. Interfaces 2017, 9, 44429–44440.

(2) Fic, K.; Lota, G.; Meller, M.; Frackowiak, E. Novel Insight into Neutral Medium as Electrolyte for High-Voltage Supercapacitors. Energy Environ. Sci. 2012, 5, 5842–5850.

(3) Abbas, Q.; Ratajczak, P.; Béguin, F. Sodium Molybdate - an Additive of Choice for Enhancing the Performance of AC/AC Electrochemical Capacitors in a Salt Aqueous Electrolyte. Faraday Discuss. 2014, 172, 199–214.

(4) LI, L.; LI, F. The Effect of Carbonyl, Carboxyl and Hydroxyl Groups on the Capacitance of Carbon Nanotubes. New Carbon Mater. 2011, 26, 224–228.

(5) Pan, H.; Li, J.; Feng, Y. P. Carbon Nanotubes for Supercapacitor. Nanoscale Research Letters, 2010, 5, 654–668.

(6) Cã Nete-Rosales, P.; Álvarez-Lueje, A.; Bollo, S. Ethylendiamine-Functionalized Multi-Walled Carbon Nanotubes Prevent Cationic Dispersant Use in the Electrochemical Detection of DsDNA. Sensors Actuators B. Chem. 2014, 191, 688–694.

(7) Huang, Z.-D.; Zhang, B.; Oh, S.-W.; Zheng, Q.-B.; Lin, X.-Y.; Yousefi, N.; Kim, J.-K. Self-Assembled Reduced Graphene Oxide/Carbon Nanotube Thin Films as Electrodes for Supercapacitors. J. Mater. Chem. 2012, 22, 3591.

(8) Béguin, F.; Presser, V.; Balducci, A.; Frackowiak, E. Carbons and Electrolytes for Advanced Supercapacitors. Adv. Mater. 2014, 26, 2219–2251.

(9) Abbas, Q.; Ratajczak, P.; Béguin, F. Sodium Molybdate - An Additive of Choice for Enhancing the Performance of AC/AC Electrochemical Capacitors in a Salt Aqueous Electrolyte. Faraday Discuss. 2014, 172, 199–214.

APPENDIX D. SUPPORTING INFORMATION IV

Venus flytrap-like hierarchical NiCoMn-O@NiMoO4@C nanosheet arrays as free-standing core-shell electrode material for hybrid supercapacitor with high electrochemical performance

Xiaohui Tang, Yu Hui Lui, Bowei Zhang, Shan Hu*

Department of Mechanical Engineering, Iowa State University, Ames, IA, 50010, USA

* Corresponding author Email: shanhu@iastate.edu

Synthesis process of Ni-O, Co-O, Mn-O, NiCo-O, NiMn-O and CoMn-O

For the monometallic oxides (including Ni-O, Co-O and Mn-O), the precursor solution is made by dissolving 3 mmol of $Ni(NO_3)_2 \cdot 6H_2O$ or 3 mmol of $CoCl_2 \cdot 6H_2O$ or 3 mmol of $(CH_3CO_2)_2Mn \cdot 4H_2O$ into 70 mL deionized water, respectively. The prepared solution is poured into 100 mL Teflon-lined stainless steel autoclave where a cleaned carbon cloth substrate is vertically placed. Then, the autoclave is heated up to 120 ^oC (at a heating rate of 3 ^oC/min) in a box oven and its temperature is maintained for 6 h. The obtained sample is cleaned by ultrasonication in deionized water for 10s. Afterwards, the sample is dried in a vacuum oven at 60 ^oC for 1h and, then, it is annealed at 300^oC (2 ^oC/min) for 2h in a tube furnace under Argon atmosphere.

For the bimetallic oxides (including NiCo-O, NiMn-O and CoMn-O), the precursor solution is made by mixing the two out of three precursor salts with the molar mass of 1.5 mmol, respectively, in 70 ml deionized water. In other words, the total molar mass is 3 mmol and molar ratio between the precursor salts are 1:1. The rest processes (including hydrothermal and annealing processes) are the same.

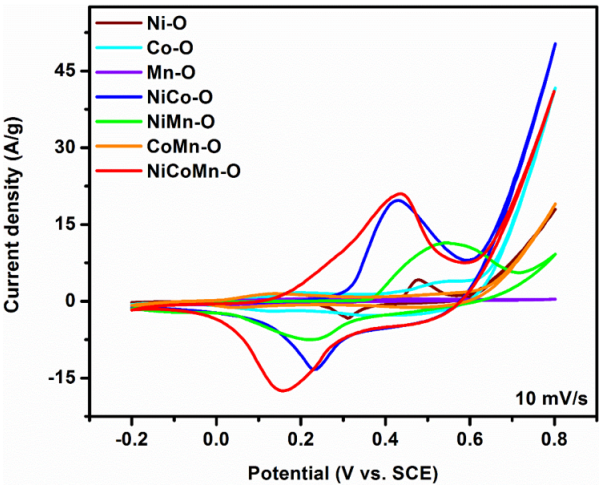

Figure S5.1. CV curves of metal oxides with different chemical compositions at the scan rate of 10 mV/s.

It can be found that, at the same scan rates, NiCoMn-O has the largest peak current and CV area, indicating it has the best electrical conductivity and electrochemical performance among these materials.

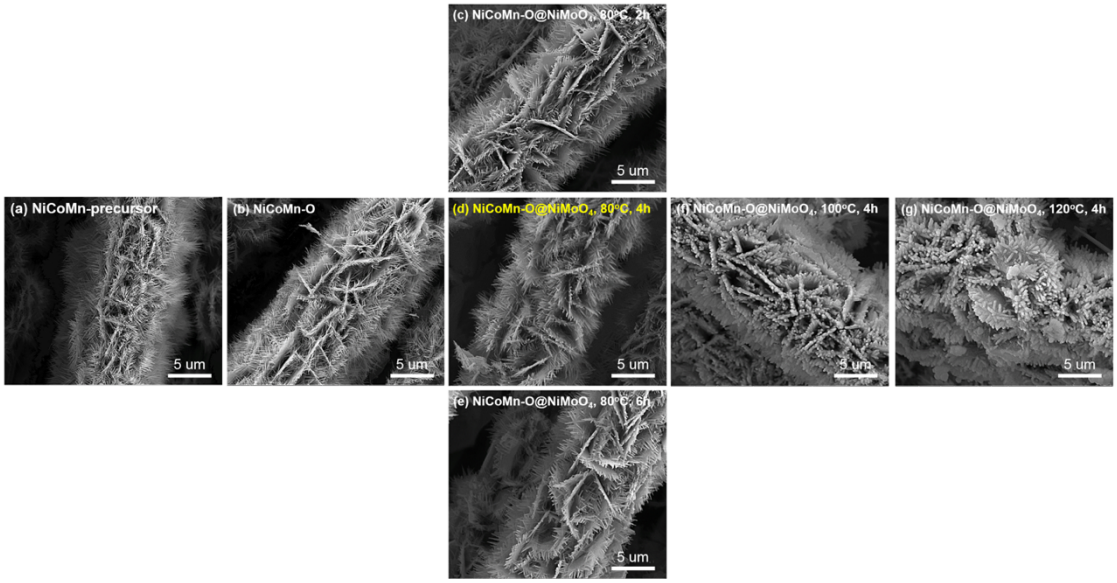

Figure S5.2. SEM images of (a) NiCoMn-precursor, (b) NiCoMn-O, (c) NiCoMn-O@$NiMoO_4$ whose $NiMoO_4$ layer is synthesized at 80 °C for 2 h, (d) NiCoMn-O@$NiMoO_4$ whose $NiMoO_4$ layer is synthesized at 80 °C for 4 h ,(e) NiCoMn-O@$NiMoO_4$ whose $NiMoO_4$ layer is synthesized at 80 °C for 6 h, (f) NiCoMn-O@$NiMoO_4$ whose $NiMoO_4$ layer is synthesized at 100 °C for 4 h, (g) NiCoMn-O@$NiMoO_4$ whose $NiMoO_4$ layer is synthesized at 120 °C for 4 h.

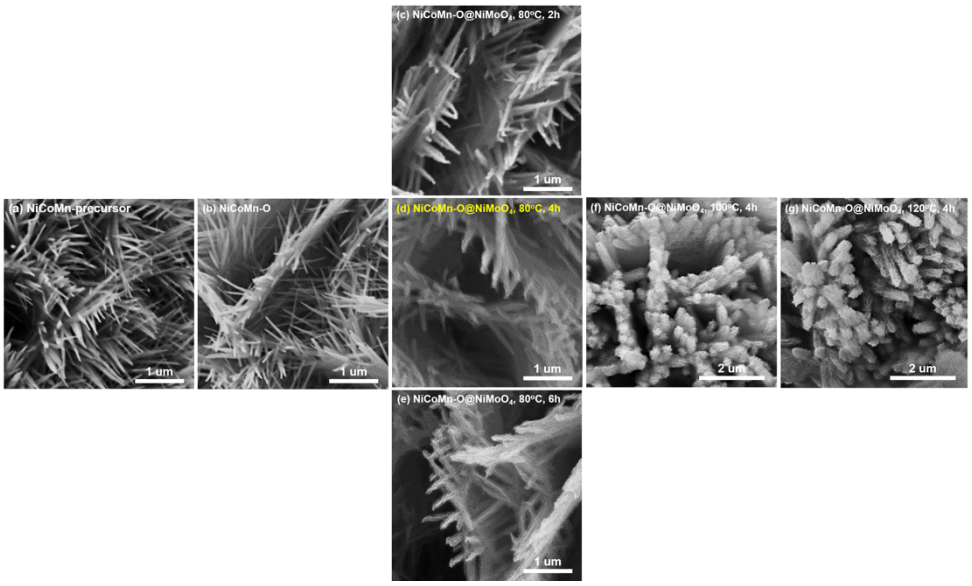

Figure S5.3. SEM images (with higher magnification) of (a) NiCoMn-precursor, (b) NiCoMn-O, (c) NiCoMn-O@$NiMoO_4$ whose $NiMoO_4$ layer is synthesized at 80 ºC for 2 h, (d) NiCoMn-O@$NiMoO_4$ whose $NiMoO_4$ layer is synthesized at 80 ºC for 4 h ,(e) NiCoMn-O@$NiMoO_4$ whose $NiMoO_4$ layer is synthesized at 80 ºC for 6 h, (f) NiCoMn-O@$NiMoO_4$ whose $NiMoO_4$ layer is synthesized at 100 ºC for 4 h, (g) NiCoMn-O@$NiMoO_4$ whose $NiMoO_4$ layer is synthesized at 120 ºC for 4 h.

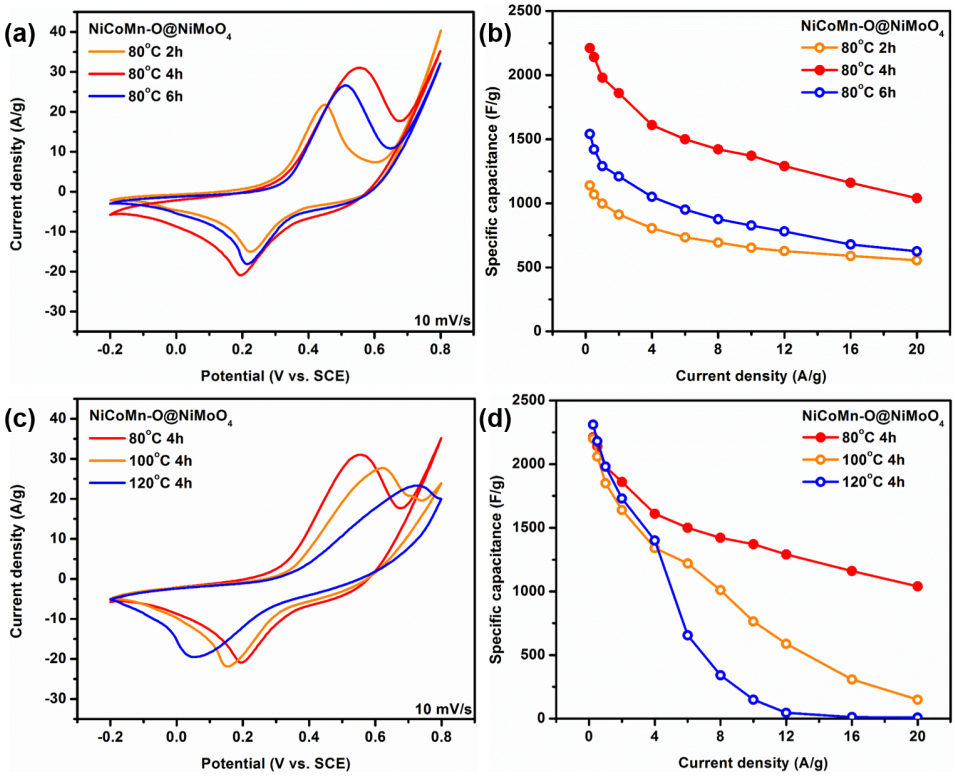

Figure S5.4. (a) CV curves and (b) calculated discharge specific capacitances of NiCoMn-O@$NiMoO_4$ samples synthesized by hydrothermal methods at 80 ºC , but their holding time is

different (i.e. 2h , 4h and 6h). (c) CV curves and and (d) calculated discharge specific capacitances of NiCoMn-O@$NiMoO_4$ samples synthesized by hydrothermal methods at different temperatures (i.e. 80 ºC, 100 ºC and 120 ºC), but their holding time is 4h.

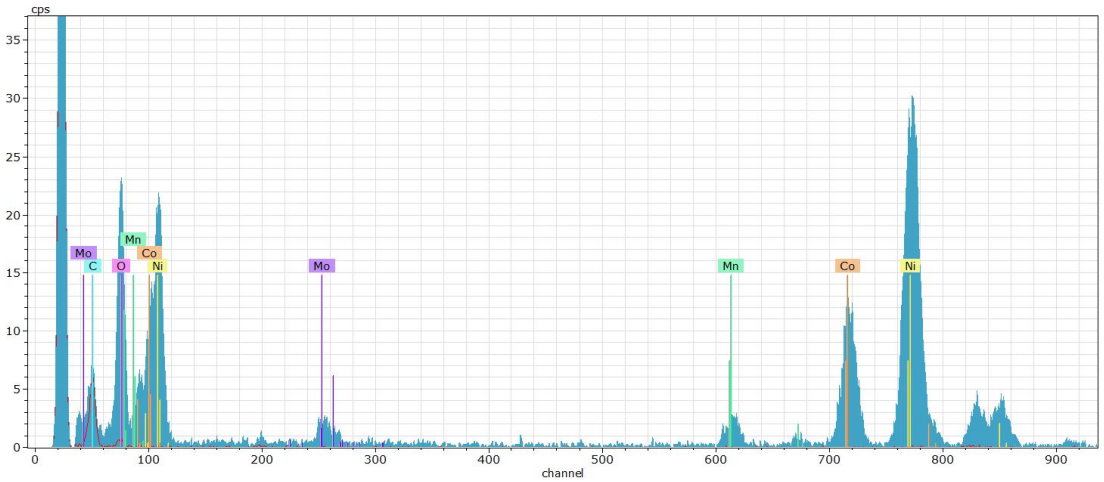

Figure S5.5. EDS spectrum of NiCoMn-O@$NiMoO_4$@C.

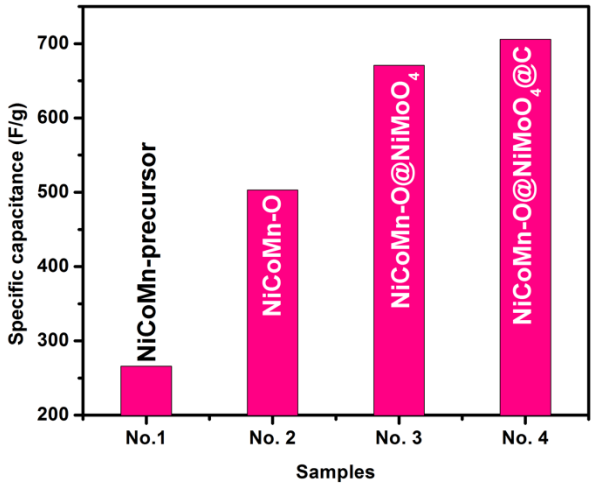

Figure S5.6. The specific capacitances of different samples calculated from CV curves at the scan rate of 10 mV/s.

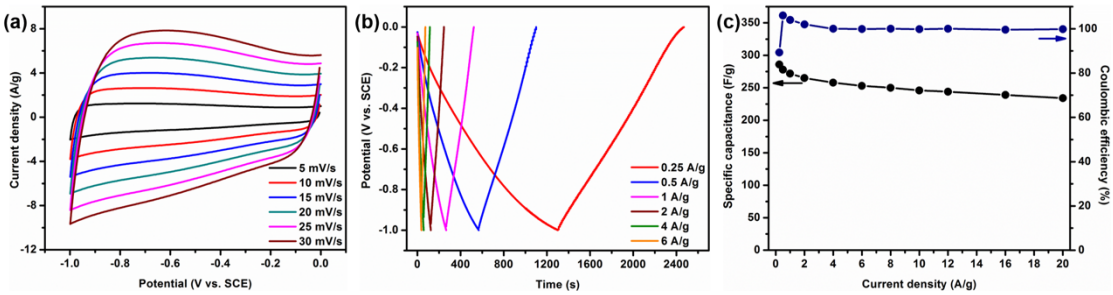

Figure S5.7. (a) CV curves of AC negative electrode. (b) GCD curves of AC negative electrode and (c) the corresponding specific capacitances and coulombic efficiencies calculated from the discharge GCD curves.

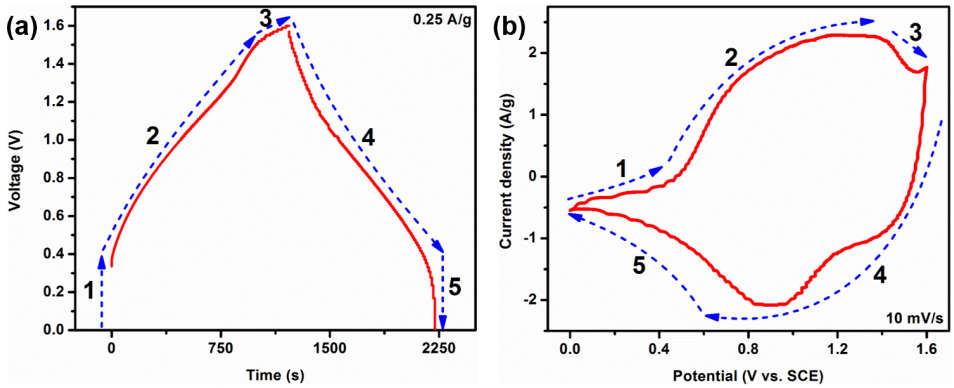

Figure S5.8. (a) GCD curve of NiCoMn-O@$NiMoO_4$@C at the current density of 0.25 A/g. (b) CV curve of NiCoMn-O@$NiMoO_4$@C at the scan rate of 10 mV/s.